Functionalized Composites for 3D-Printing and Additive Manufacturing Applications

By

Cole Dylan Brubaker

Dissertation

Submitted to the Faculty of the

Graduate School of Vanderbilt University

in partial fulfillment of the requirements

for the degree of

DOCTOR OF PHILOSOPHY

in

Civil Engineering

January 31, 2019

Nashville, Tennessee

Approved:

Douglas Adams, PhD

G. Kane Jennings, PhD

Sankaran Mahadevan, PhD

Sandra Rosenthal, PhD

Florence Sanchez, PhD

To my family, Scott, Melinda, and Quinn.

ACKNOWLEDGMENTS

To whom this dissertation is dedicated, I would first like to acknowledge my family for their never ending support, guidance, love and encouragement. Through the ups and the downs, the good and the bad, the countless phone calls and trips back home, you all were with me every step of the way. Without you, this journey would not have been possible. To my advisors, Dr. Douglas Adams and Dr. Kane Jennings, thank you for your advice, guidance and encouragement throughout my time at Vanderbilt. Over the past four and a half years I have grown both personally and intellectually, and could not have asked for a better set of mentors and friends. I would also like to thank the members of my committee Dr. Sankaran Mahadevan, Dr. Sandra Rosenthal and Dr. Florence Sanchez for their time and valuable insight. Particularly, I would like to thank Dr. Rosenthal for our research collaborations and access to her chemistry lab throughout my PhD studies. To Garrett Thorne, Dave Koester, and Chris Nash, there is no one I would rather spend my hot chicken and donut Fridays with. You three brought out the best of LaSIR. I would also like to thank my fellow graduate and undergraduate students I had the pleasure of working with, namely Dr. Ian Njoroge, Talitha Frecker, Michael Davies and Kailey Newcome. To the countless friends I have made in Nashville, I will always cherish the good times, adventures, and memories that helped make this city home for the past four and a half years. And last but not least, I would like to thank my hair and hairline for making the ultimate sacrifice. You may be gone, but your luscious blond locks will never be forgotten.

Funding for my PhD and the research covered in this dissertation was sponsored under the support of the Nuclear Energy Enabling Technologies (NEET) Program, Award Number DE-NE0008712, as well as the support of the U.S. Office of Naval Research, which provided funding

for this research as part of a Multi-Disciplinary University Research Initiative on Sound and Electromagnetic Interacting Waves under grant number N00014-10-1-0958.

TABLE OF CONTENTS

Page

LIST OF TABLES

Page

LIST OF FIGURES

Page

LIST OF PUBLICATIONS

The following peer reviewed publications have been adapted and included in the following chapters as described here:

Chapter 3 – 'Incorporation of Fluorescent Quantum Dots for 3D Printing and Additive Manufacturing Applications'

Brubaker, Cole, Frecker, Talitha, McBride, James, Reid, Kemar, Jennings, Kane, Rosenthal, Sandra, Adams, Douglas. "Incorporation of Fluorescent Quantum Dots for 3D Printing and Additive Manufacturing Applications." *J. Mater. Chem. C, 6, 28, 7584 - 7593* (2018) DOI: 10.1039/ct8tc02024h.

Chapter 4 – 'Nondestructive Evaluation and Detection of Defects in 3D-Printed Materials Using the Optical Properties of Gold Nanoparticles'

Brubaker, Cole, Davies, Michael, McBride, James, Rosenthal, Sandra, Jennings, Kane, Adams, Douglas. "Nondestructive Evaluation and Detection of Defects in 3D-Printed Materials Using the Optical Properties of Gold Nanoparticles." *ACS Appl. Nano Mater.* 1, 3, 1377-1384 (2018) DOI: 10.1021/acsanm.8b00142.

Chapter 5 – '3D Printed Electroluminescent Devices'

Brubaker, Cole, Newcome, Kailey, Jennings, Kane, Adams, Douglas. "3D Printed Electroluminescent Devices." *Paper in submission.*

Chapter 1

Introduction

1.1 3D Printing and Additive Manufacturing

With the ability to shorten production times, while simultaneously minimizing material waste, additive manufacturing technologies and techniques, including 3D printing, have emerged with the potential to revolutionize the way various materials are produced, utilized and repaired across a growing number of fields and applications. In fact, many industry experts have dubbed additive manufacturing and 3D printing related technologies as the fourth industrial revolution – Industry 4.0 – due to its highly disruptive nature in the manufacturing sector. In order to accelerate product development and minimize manufacturing and production costs (e.g. retooling), additive manufacturing is being used to 3D print a myriad of parts and components for a number of products in applications ranging from aircrafts and automobiles to biological implants and hearing aids, among many others.[1,2] The relative ease and speed at which new parts and prototypes with complicated geometries can be designed and fabricated has driven the need, and continued demand, for 3D printing technologies. In fact, industrial adoption of 3D printing is projected to grow at a rate of 45% annually, surpassing a $10 billion market space by 2020.[3]

Traditionally, 3D printing occurs in a multistep process through which a part is drafted and designed using computer-aided design (CAD) software, converted to the appropriate file type for printing, and finally, deposited in a layer-by-layer fashion using the desired material to produce a final part.[2,4,5] Formally, additive manufacturing is defined by the ISO/ASTM

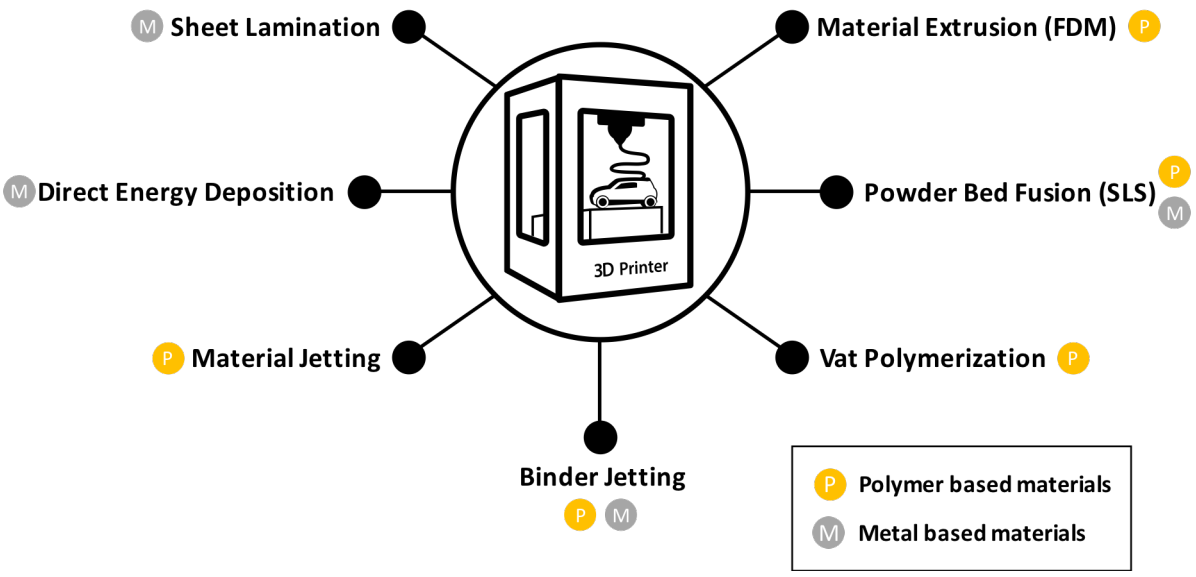

Figure 1.1 Various categories of additive manufacturing technologies

joint standard 52900 as the 'process of joining materials to make parts from 3D model data, usually layer upon layer, as opposed to subtractive manufacturing and formative manufacturing methodologies'.[6] With a variety of compatible materials ranging from plastics, metals, polymer composites and ceramics, to organic materials and living cells, additive manufacturing technologies are typically categorized according to the selected material and form of material deposition.[2,7,8] Additive manufacturing technologies are often grouped among seven main categories including: material extrusion, powder bed fusion, vat polymerization, binder jetting, material jetting, direct energy deposition, and sheet lamination (Figure 1.1).[8]

Though each approach has its own set of advantages and drawbacks, fused deposition modeling (FDM), a form of material extrusion, has emerged as a prominent and popular form of additive manufacturing. The relative affordability of FDM printing hardware, combined with the ease of materials processing and ability to rapidly manufacture functional structures

and components, has helped drive the continued demand for FDM-related systems and technologies not only in industrial applications, but for commercial and hobbyist use as well.[9] Similar to other processes where parts and components are 'built up' in a layer-by-layer fashion, FDM utilizes a thermoplastic feedstock to produce and manufacture the desired part or structure. Here, a polymer-based filament is fed through a nozzle after being heated above its melting temperature and the subsequent molten plastic is deposited onto a build plate. With each layer of material deposited, the printer's build plate is sequentially lowered as the nozzle travels in a predetermined path following the part geometry to manufacture the final structure.

Through materials processing and design considerations, the development of new polymer-based materials compatible with material extrusion-based technologies has been a recent area of focus in the advancement of FDM technologies. Namely, there has been increasing interest in the design and development of functionalized and other 'smart' materials for additive manufacturing applications. In order to accomplish this goal, researchers have explored the use of additives and polymer design/modifications to enable 3D-printed materials and structures with a wide range of unique, and oftentimes enhanced, material properties, behaviors and responses not observed in the unmodified host polymer host matrix. Specifically, the incorporation of additives, such as nano- and micron-scale materials, for example, within the 3D printing process is rapidly gaining interest in both academic and industrial fields due to the tremendous flexibility that this approach offers for not only the design of the materials, but also the additive manufacturing process as a whole.

On the length scale of approximately 1 – 100 μm, the incorporation of nano- and other micron-size material systems and additives within 3D printing processes can enable a number of new and customizable material properties including enhanced material strength properties,[10]

increased chemical durability[11] and advanced optical responses,[12] among other properties, that are not observed in the unmodified host material. In order to develop such functionalized composites, additives are typically incorporated within the 3D printing process using one of two methodologies: (1) intermittent layer-by-layer deposition and introduction of the selected additive in the unmodified host matrix through stoppages in the printing operation, and (2) direct incorporation within printer filament through dissolution and premixing of the desired additives within the polymer host matrix prior to printing.[13,14] In this dissertation, I focus on the second approach, where functionalized filament is designed, fabricated, and extruded for use with conventional FDM type 3D printing systems for each composite material system studied. To date, a range of organic[15] and inorganic material systems including, carbon nanotubes,[16–18] metallic nanoparticles,[19–24] graphene,[25,26] and fibers,[27–29] among others, are various examples of nano- and micron-scale systems and additives that have been incorporated within the 3D printing process. Such 3D-printed composites have been utilized for applications including, but not limited to, conductive materials,[16,17,21,22] sensors,[17,19] catalysis and photocatalytic processes,[23,30] drug delivery systems,[31,32] advanced optical applications,[20] and materials with improved mechanical strength and durability.[27–29] In each case, a number of physical parameters – ranging from solubility, miscibility, melting temperature and thermal stability, to materials durability, processability and optical characteristics – are crucial considerations for ensuring the compatibility and overall functionality of 3D-printed composite systems.

Building upon the recent progress in these new 3D-printed material systems, the focus of my dissertation revolves around the design, development, characterization, inspection, and implementation of optically enhanced composites through the use of various nano- and micron-

scale additives. Specifically, I explore the incorporation of cadmium-based quantum dots (Chapter 3), gold nanoparticles (Chapter 4) and zinc-based phosphor materials (Chapter 5) within a polylactic acid (PLA) polymer host matrix for their compatibility with additive manufacturing and FDM applications. Quantum dots, nanoparticles, and phosphors were selected as additives based on a number of considerations including their compatibility with PLA, tunable optical response, and stimuli responsive behavior, among others, as further discussed in the following sections. For each composite system, material characterizations and optical testing is performed to reveal the effects that functionalization has on the properties of the embedded additives and PLA polymer host matrix following materials processing and 3D printing. Additionally, relevant applications and potential end uses for the three material systems are developed, including passive devices (frequency selective light guide and nondestructive inspection gauge), and active devices (electroluminescent transducer), to demonstrate the versatility of this approach for designing and developing functionalized materials. With the continued adoption of additive manufacturing and 3D printing technologies across a growing number of fields and industries, advancements in materials processing and design techniques are becoming more and more necessary. The use of three unique material additives demonstrates the scalability of this design process and approach for ultimately expanding the number of material systems compatible with FDM applications beyond just those discussed in this thesis.

1.2 Polylactic Acid (PLA) - Polymer Host Matrix

Polylactic acid (PLA) is a non-toxic biodegradable, aliphatic, thermoplastic polymer made from renewable resources. It is one of the most commonly used plastics for 3D printing and additive manufacturing applications due in part to its favorable materials properties.[33–35] Falling under the category of linear polyesters, PLA is characterized by its amorphous semi-crystalline structure with a melting temperature of ~180 °C and a glass transition temperature near 70 °C. A number of common solvents such as dichloromethane (DCM), chloroform, tetrahydrofuran (THF), pyridine and acetone, among others, have all been shown to effectively dissolve PLA.[36] Due to its molecular structure and other factors including molecular weight and crystallinity, PLA can be synthesized and designed to have little to no optical contributions across the visible range (i.e. 400 nm – 800 nm).[37] Because both absorbance and photoluminescence are either minimal or completely absent in the unmodified host matrix, the overall optical response of PLA can be easily customized and tuned through the use of various material additives as explored in this dissertation.

Over the past two decades, advancements in synthesis and polymerization procedures have helped reduce the cost associated with the production of PLA, making it a viable alternative to traditional petroleum-based plastics.[38] Prior to its adoption for 3D printing and additive manufacturing applications, PLA has been used with a number of conventional manufacturing methods such as injection and blow molding. For melt-processing based approaches, a pelletized PLA feedstock is heated above its melting temperature, injected into the desired mold and subsequently cooled to obtain the final part or structure. Using these techniques, functional products and parts ranging from biomedical implants and devices, to packaging, coatings and films, among other products, have all been manufactured using

PLA.[39,40] The progression from conventional manufacturing approaches to its adoption for 3D printing and additive manufacturing techniques was relatively organic, as a number of the necessary materials processing and techniques and methods for PLA had previously been developed.

1.3 Quantum Dots

Falling in the category of nanomaterials, quantum dots are crystalline, semiconductor nanoparticles on the length scale of several nanometers. They exhibit distinct optical and other electromagnetic characteristics that are typically not observed at the bulk scale.[41] Quantum dots were first discovered in the early 1980's and have been used in a number of diverse applications ranging from solar cells,[42,43] to biological imaging and tracking,[44] lighting/displays[45,46] (including the introduction of commercially available quantum dot TVs), and mechanical load sensing,[47] just to name a few applications. By tuning the material composition and relative size of the resulting quantum dot, the overall optical response and behavior can be modulated according to the selected synthesis procedure.

The optical response and behavior of quantum dots are primarily driven by the presence of discrete energy levels within the final material system. Sandwiched between the bottom of the conduction band and top of the valence band, quantum dots contain a band gap in which electrons are able to move under the presence of external excitation sources.[48,49] These sources, including both electrical and optical inputs, cause the movement of excitons between electron-hole pairs across the band gap, leading to the release of energy in the form of light due to separation and recombination. This release of light is called fluorescence. The overall size of

the energy levels/band gap, and resultant fluorescence and emissive optical behavior, is governed almost completely by the size and material composition of the quantum dot.[50]

Since their discovery, a number of quantum dot systems have been designed and developed through such modulations in material properties and synthesis procedures.[51] Combining the range of applicable synthesis approaches (including colloidal synthesis, lithography, and patterned growth, among others) with a variety of starting materials (e.g. cadmium, zinc, sulfur, selenide, etc.), quantum dots can be tuned to emit virtually any color across the visible spectrum.[52] For the purposes of this dissertation, my work focuses specifically on the use of cadmium-based quantum dot systems, namely cadmium sulfur selenide graded alloy quantum dots (CdSSe QDs). CdSSe QDs were selected for their use in 3D printing applications in part due to their miscibility with PLA in its dissolved state, and resultant optical properties with a relatively high quantum yield. Additional information regarding the CdSSe QD synthesis procedure and incorporation within the 3D printing process is discussed in Chapters 2 and 3, respectively.

1.4 Metallic Nanoparticles

Metallic nanoparticle systems, including the gold nanoparticles studied in this thesis, represent an additional platform upon which optically enhanced materials for additive manufacturing applications can be developed. With a variety of synthesis procedures dating back to the 1850's,[53] a number of chemical modifications and ligand exchange procedures can be performed to develop a range of gold nanoparticle-based polymers and materials compatible with 3D printing applications. To date, gold nanomaterials have been used for various sensing applications including the detection of mechanical loads,[54] fluctuations in temperature,[55] and

changes in pH,[56] among other chemical[57,58] and biological[53] stimuli, through distinct changes in optical properties alone.

Unlike quantum dot systems whose emission is primarily driven by band-gap energy considerations, the optical response of gold nanoparticles is a result of electromagnetic effects related to local surface plasmon resonance (LSPR).[59] LSPR occurs when light interacts with particles much smaller than the incident wavelength, leading to an oscillation of the particle and a resultant peak in the recorded absorbance spectra.[60] The LSPR peak is sensitive to a number of factors including nanoparticle shape, size, inter-particle distance and aggregation, surface ligands, as well as the refractive index and dielectric properties of the surrounding media. Fluctuations in any of these parameters have been shown to influence the optical properties, and recorded absorbance spectra, of as-synthesized gold nanoparticles. While intermediate in price relative to commercially available dyes, a combination of their multi-stimuli responsive behavior, long-term temporal optical stability, chemical inertness and solubility in various organic solvents make gold nanomaterials a promising approach for the continued development of functionalized materials for additive manufacturing applications and advanced sensing technologies. Detailed gold nanoparticle synthesis procedures as well as their use in 3D printing applications is discussed in Chapters 2 and 4, respectively.

1.5 Phosphors

With applications ranging from lighting and displays[61,62] to wearable devices[63–65] and even structural health monitoring[66] and visual sensing,[67] metal-doped phosphor systems have received significant interest from the research community due to their tunable response and behavior. Owing to their underlying composition and structure, luminescent phosphor

materials capable of emitting colors across the visible spectrum have been developed.[68,69] Among the numerous phosphor systems that have been reported in the literature, ZnS-based phosphors are one of the most commonly studied due to their combined intense luminescent and emissive properties and temporal durability and stability.[70–72] Transition metal ions, including copper[70–73] and manganese,[72–75] are two examples of dopants that have been used to modulate the optical response and emissive behavior of ZnS-based phosphor materials. In each case, the substitution of metal ions within the host crystal lattice result in the formation of discrete energy levels responsible for the observed differences in the luminescent and emissive behaviors for the various metal ion dopants; similar to the driving mechanisms that were previously described for quantum dot fluorescence.

Traditionally incorporated within a polymer host matrix or binder, both electroluminescent (EL) and mechanoluminescent (ML) devices and structures capable of optically responding to electrical and mechanical stimuli, respectively, have been demonstrated using metal-doped phosphor systems. In each case, the application of an external stimulus results in a bright luminescence due to the presence of the embedded phosphors. As a third material system, ZnS-based phosphors were selected for the development of visually responsive and optically enhanced materials compatible with additive manufacturing and 3D printing applications due in part to the considerations listed above: intense luminescence and optical response, temporal stability, and responsive nature to both mechanical and electrical stimuli. Details regarding the fabrication and use of PLA/phosphor functionalized materials and devices are included in Chapters 2 and 5, respectively.

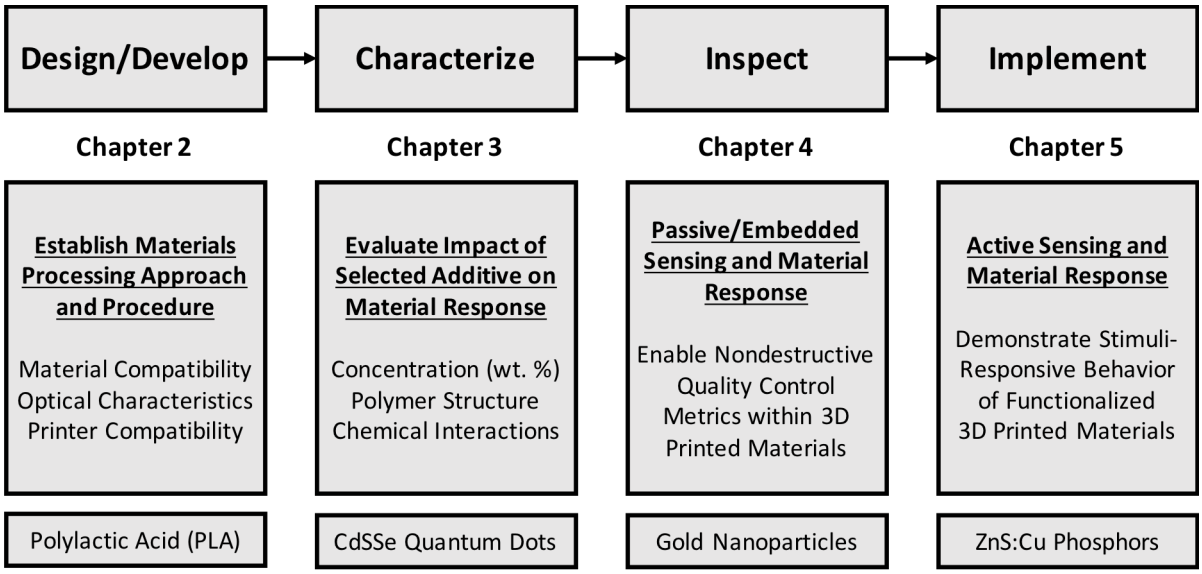

Figure 1.2 Graphical overview and outline of individual Chapters covered in this thesis

1.6 Scope of Work

The scope of this work involves the design and development of functionalized materials for additive manufacturing applications. A graphical overview and outline detailing the contribution of each chapter and this thesis as a whole is shown in Figure 1.2. Through various materials processing and design considerations, I present a methodology that effectively incorporates the unique material and size dependent behaviors of several nano- and micron-scale additives within larger, bulk scale 3D-printed parts and materials. This approach is described in further detail in Chapter 2, where functionalized filament compatible with commercially available FDM 3D-printing systems is fabricated by combining a solution-based mixing process with various drying and extrusion steps.

In Chapter 3, I describe the incorporation of fluorescent CdSSe quantum dots within a 3D printing process to evaluate the effects that functionalization has on the underlying materials properties and the responses of both the polymer host matrix and embedded additive.

Absorbance, photoluminescence, thermal analysis and mechanical testing are studied to quantify how filament functionalization changes the optical and material properties of the embedded quantum dots and PLA host matrix following 3D-printing. Additionally, following materials characterization, I demonstrate the ability to 3D print light pipes and fluorescent devices as a relevant application and potential use of quantum dots in additive manufacturing applications.

In Chapter 4, I incorporate the optical properties of gold nanoparticles into 3D printed specimens to facilitate nondestructive inspection through the detection of defects and missing print layers. Consistent with Beer-Lambert's Law for nanoparticles in solution, a linear relationship between absorbance intensity and the total number of print layers is observed. By analyzing changes in absorbance intensity, the presence, location and extent of material defects as small as 0.2 mm are identified through a nondestructive approach to enable rapid inspection of 3D printed parts and structures.

In Chapter 5, I demonstrate the use of ZnS:Cu phosphors in the development of stimuli responsive materials compatible with additive manufacturing applications. Incorporated within a PLA host matrix, ZnS:Cu functionalized filament is used to manufacture and 3D print alternating current electroluminescent devices. By applying a voltage across the phosphor-functionalized material, the 3D-printed alternating current electroluminescent devices displayed a tunable bright blue/green luminescent behavior. The observed optical response was found to be dependent on both the applied voltage and frequency of excitation, as the recorded emission displayed a blue shift with increasing excitation frequencies.

By focusing on materials and process design parameters, this work reveals key insights into how 3D-printed composite systems can be 'programmed' toward the development of

multifunctional and stimuli-responsive materials. In all, the methodologies and approaches discussed in this dissertation represent a collective body of work encompassing the design, development, characterization, inspection and implementation of functional materials compatible with FDM and 3D printing technologies. Through the proper selection of the polymer host matrix and material additive, the processes and approaches developed in this thesis represent a promising direction for the continued advancement of both functional composite materials and the field of additive manufacturing as a whole.

Chapter 2

Experimental and Characterization Methods

The following section describes in detail the experimental work performed during the development of functionalized materials for additive manufacturing applications and uses. An overview of all relevant materials, synthesis and processing procedures, as well as relevant material characterization and classification methods are herein described.

2.1 Materials

The following materials and chemicals were used as received in the development of functionalized materials for additive manufacturing applications and uses. Cadmium oxide (CdO, 99.99% Sigma), octadecene (ODE, 90% Sigma), oleic acid (OA, 90% Sigma), tri-n-butylphosphine (TBP, 97% mixture of isomers Sigma), n-dodecylphosphonic acid (DDPA Sigma), hexadecylamine (HDA, 98% Sigma), gold(III) chloride trihydrate (≥99.9% trace metal basis Sigma), tert-butyl amine borane (97% Sigma), elemental selenium (Se, 99.999% Alfa Aesar), sulfur powder (USP Sublimed Fisher Scientific), triphenylphosphine (99% STREM Chemicals), 1-dodecanethiol (≥98.5% Acros Organics), potassium hydroxide (KOH, Fischer Scientific), trisodium citrate dehydrate (Sigma Aldrich), citric acid (Fischer Scientific), and poly(acrylic acid) (PAA, M_W ~100,000 35 wt. % in H_2O Sigma Aldrich) were used as received. Dichloromethane, toluene, chloroform, tetrahydrofuran, pyridine, acetone and ethanol and all other solvents were used as received from Sigma Aldrich or Fischer Scientific. Metal doped phosphor powder was purchased from Fulcom (Marshal) Company Limited (LP-6842) and

used as received. Polylactic acid pellets (3D850) were purchased from Filabot and supplied by Natureworks. Conductive PLA filament was purchased from Proto-Pasta and poly vinyl alcohol (PVA) filament was purchased from Ultimaker. ITO-coated glass slides were purchased from Delta Technologies (Part No. CG-51IN-1115).

2.2 Quantum Dot Synthesis Procedures

The following synthesis procedures were used to synthesize the ultra-small white light emitting cadmium sulfur selenide quantum dots and cadmium sulfur selenide graded alloy quantum dots.

2.2.1 Ultra-Small White Light Emitting CdSe Quantum Dots

Ultra-small white light emitting cadmium selenide quantum dots (CdSe QDs) were synthesized using a one-pot procedure according to the protocol described by Bowers et al.[76] A combination of 0.496 g dodecylphosphonic acid (DDPA), 0.128 g cadmium oxide (CdO), 6 g tri-n-octylphosphine oxide (TOPO), and 4 g hexadecylamine (HDA) were mixed together and heated to 330 °C under inert atmosphere until a clear and colorless solution was obtained. Next, a 0.2 M solution of Se:tributylphosphine (TBP) precursor was injected, quickly followed by the addition of 15 mL of butanol to cool the solution (less than 10 s). The solution was then quickly removed from the heating plate and rapidly cooled using compressed air, thereby stopping QD growth. The resulting CdSe QDs were solvated in a chloroform to avoid aggregation between individual QDs. Gel permeation chromatography (GPC), a method of size exclusion chromatography (SEC), was then used to clean the CdSe QDs and remove any precursor and byproducts leftover from the synthesis process. 'Clean' CdSe QDs were stored

out of direct light to avoid quenching the QD emission. The synthesis produced monodisperse QDs approximately 1.5 nm in diameter with quantum yields ranging from 6% to 10% on average. To further increase the overall quantum yield, CdSe QDs were treated with a citric acid capping agent. CdSe QDs in chloroform were added to an excess of citric acid and heated to 60 °C. Once the temperature reached 60 °C, the solution was cooled and filtered to remove excess citric acid. The quantum yield increased from ~10% to ~45% following treatment. Due to the increased quantum yield, all samples discussed and tested in this dissertation were fabricated using citric acid treated CdSe QDs.

2.2.2 CdSSe Graded Alloy Quantum Dots

Cadmium sulfur selenide graded alloy quantum dots (CdSSe QDs) were synthesized according to the protocol presented by Keene et al.[77] In short, the synthesis proceeded as follows: 4 mmol cadmium oxide (CdO) and 16 mmol oleic acid (OA) were mixed with 80 mL octadecene (ODE) in a 250 mL round bottom flask and heated with stirring to 300 °C under inert atmosphere. Once the solution was clear and colorless, a mixture of 2.24 mL 0.75 M sulfur/tri-n-butylphosphine/octadecene (S/TBP/ODE) was quickly injected. Following injection, the reaction was further heated at 260 °C under stirring for an additional 2 h, upon which the solution was cooled using compressed air. CdSSe QDs were cleaned through centrifugation for 15 min at 7500 RPM in a butanol/ethanol mixture (3:2 ratio by volume), resuspended in toluene and run through a column of poly(styrene-co-divinylbenzene).[78] 'Clean' CdSSe QDs were resuspended in toluene and stored out of direct light to avoid quenching of the QD emission.

2.3 Gold Nanoparticle Synthesis Procedures

The following synthesis procedures were used to synthesize poly(acrylic acid) coated and dodecanethiol-capped gold nanoparticles.

2.3.1 Poly(Acrylic Acid) Coated Gold Nanoparticles

Poly(acrylic acid) (PAA) coated gold nanoparticles (AuNPs) were obtained through a ligand exchange process previously reported in the literature.[79] First, water soluble gold nanoparticles were synthesized according to a modified Turkevich method.[80,81] On a stir plate, 50 mL of 0.25 mM gold(III) chloride trihydrate ($HauCl_4 \bullet 3H_2O$) in a flat bottom flask was brought to a boil under reflux conditions to ensure a constant reaction volume. Once boiling, 1 mL of sodium citrate (194 mM) was injected into the flask under vigorous stirring and heating. After the addition of the sodium citrate reducing agent, the solution quickly changed color from clear to bright red, indicating the formation of gold nanoparticles. The solution was then heated for an additional 15 min and stirred under reflux conditions for 2 h. The resulting solution was transferred to a brown bottle and stored in a refrigerator until use. As synthesized nanoparticles had an average diameter of approximately 26 nm, as confirmed through UV-Vis absorption data and corresponding calculations, as well as with dynamic light scattering (DLS) measurements.

Following the above synthesis procedure, 1 mL of stock gold nanoparticles was transferred into centrifuge tubes, and the pH of the solution was adjusted through the addition of 40 μL NaOH (0.5 M) to facilitate the ligand exchange process. This change in pH can be visually observed, as the color of the gold nanoparticle solution shifted from red to purple/blue. Next, 10 μL of PAA solution was added to the gold nanoparticle solution and sonicated for 1

h to perform the ligand exchange. Following sonication, the PAA-coated gold nanoparticle solution was centrifuged at 15,000 RPM for 15 min, and the supernatant was carefully removed. PAA-coated gold nanoparticles were then further dried, and the resultant PAA-coated gold nanoparticles were resuspended in 1 mL of the desired pH buffer solution or water and again sonicated for an additional 60 min to adequately disperse the nanoparticles in the aqueous media. PAA coated gold nanoparticles displayed a darker blue/gray coloration following the ligand exchange process.

2.3.2 Dodecanethiol-stabilized Gold Nanoparticles

Dodecanethiol-stabilized gold nanoparticles (AuNPs) were synthesized according to previously reported protocols.[82,83] Briefly, $Au(PPh_3)Cl$ precursor was prepared through dropwise addition of triphenylphosphine (3.6 mmol) to gold (III) chloride trihydrate ($HAuCl_4 \bullet 3H_2O$, 1.8 mmol) in ethanol (5 mL). The resulting solution was filtered and washed with ethanol, and precipitated from acetone/THF (1:1 by volume). The resultant powder was then recrystallized to obtain $Au(PPh_3)Cl$. Next, $Au(PPh_3)Cl$ (0.25 mmol) and 125 μL of dodecanethiol were dissolved in toluene (20 mL) in a 250 mL single neck round bottom flask under stirring. The resulting mixture was heated to 50 °C, at which point tert-butyl amine borane complex (2.5 mmol) was added under vigorous stirring and additional heating for 5 min. The solution changed color from clear to a dark purple, indicating the formation of AuNPs. AuNPs were precipitated in cold ethanol and centrifuged for 15 min at 5 krpm. AuNPs were washed twice with acetone via centrifugation for 15 min at 5 krpm, and the resultant AuNPs were resuspended in toluene and stored in an amber bottle. As synthesized

AuNPs had an average diameter of 4.39 ± 0.93 nm, and displayed a well-defined surface plasmon resonance (SPR) peak at 521 nm with a purple coloration when suspended in toluene.

2.4 Functionalized Filament Fabrication

PLA was selected as the host matrix for the fabrication of functionalized filament according to the following four considerations: (1) mutual miscibility with various nanomaterials and additives in solution; (2) minimal optical contributions across the visible spectrum, including both absorbance and emission; (3) relative ease of materials processing; and (4) compatibility with commercially available FDM printers. As previously discussed, optically enhanced filament for 3D printing and additive manufacturing applications was fabricated using a solution processing-based approach. As such, the overall solubility and miscibility between the respective polymer-solvent and polymer-additive represents a crucial consideration for evaluating the compatibility of the desired material system. Miscibility is defined as the ability of two solutions to mix together and form a homogeneous solution, while solubility describes the ability of a material to completely dissolve in a given solvent. In addition to experimental testing, Hildebrand and Hansen solubility parameters can be used to approximate polymer-solvent and polymer-nanoparticle interactions, and offer an additional approach for evaluating the compatibility of a functionalized polymer system.[84] For the purposes of this thesis, dichloromethane was selected and exclusively used as the solvent for the dissolution of the PLA matrix. A poly aprotic solvent, dichloromethane is miscible with chloroform, toluene, methanol, and other solvents commonly used in nanoparticle synthesis procedures, allowing for the uniform mixing of the selected additive and PLA host matrix in its dissolved state. Furthermore, dichloromethane has a relatively low boiling point (41°C)

and a low vapor pressure, which enable the rapid evaporation and removal of solvent from the PLA composite

The following procedure was used to fabricate functionalized filament compatible with FDM type 3D printing systems. First, a desired amount of pure PLA pellets was dissolved in dichloromethane under stirring. Upon complete dissolution, the selected additives were added at the desired weight percent, and the mixture was further stirred. Once the additives were well-dispersed and thoroughly mixed, the PLA composite mixture was separated among crystallization dishes and dried to obtain a hard plastic. Dry plastic was then shredded to obtain small pellets and further dried at 100 °C for 1 h to remove excess dichloromethane prior to extrusion. This second drying step was found to be crucial, as the presence of dichloromethane led to the formation of bubbles in the filament during the extrusion process. These bubbles resulted in an inconsistent filament diameter and shape, ultimately yielding filament not suitable for use with 3D printers. After drying and complete removal of dichloromethane, a Filabot EX2 extrusion system was used to extrude pure PLA PLA/nanocomposite filament at a temperature range of 170-180°C. Extruded filament, ~2.85 mm in diameter, was then spooled using a Filabot Spooler and ready to be used for 3D printing and sample fabrication.

2.5 Sample Preparation and Fabrication

All 3D-printed test specimens were fabricated using an Ultimaker 3 Extended dual extrusion FDM type 3D printing system. A 0.4 mm nozzle heated to 215 °C was used to deposit filament onto a glass build plate heated to 60 °C with a print layer thickness of 0.1 mm. All samples were printed with a 100% material infill. The print nozzle was purged with pure PLA filament between prints to prevent clogging and minimize cross contamination between

samples. Thin film templates ranging in thickness from 1 to 10 print layers (0.1 mm to 1 mm) were fabricated to evaluate the optical response of the 3D printed composite systems studied, as discussed in the following section. In an attempt to minimize variability, a number of processing parameters were held constant between the three individual material systems tested (Table 2.1). Most notably, the only difference in the filament fabrication process for the three systems studied was the selected additive and its overall concentration in PLA. A number of prior research studies have shown that differences in processing conditions including extrusion temperature, printing temperature, layer height, print layer orientation, etc. can all significantly influence the overall material response of 3D printed parts and samples.[85–87] By holding these variables constant, the aim of this approach was to reduce the number of variables that could influence the overall material response, and instead focus on the impact of the selected additive being studied.

Table 2.1 Variations in materials processing parameters and conditions between material systems studied in this thesis.

Same	Different

• PLA polymer host matrix
• Polymer processing and filament fabrication steps
  ○ Dissolution (dichloromethane)
  ○ Drying (ambient conditions)
  ○ Shredding
  ○ Additional drying (100 °C)
  ○ Extruding (170-180 °C)
• 3D printing and sample fabrication
  ○ Nozzle temperature (215 °C)
  ○ Build plate temperature (60 °C)
  ○ Print layer height (0.1 mm)
  ○ Print layer orientation
	• Selected material additive
	  ○ CdSSe quantum dots (Ch. 3)
	  ▪ Oleic acid surface ligand
	  ○ Gold nanoparticles (Ch. 4)
	  ▪ Dodecanethiol surface ligand
	  ○ ZnS:Cu phosphor (Ch. 5)
	• Concentration of material additive in PLA

2.6 Optical Characterization

2.6.1 UV Vis Spectroscopy

Ultraviolet-visible spectrophotometry, UV-Vis, is an experimental method commonly used to determine the absorbance spectrum of a given sample. Absorbance is a useful metric for evaluating various material parameters and optical properties including color, as well as information regarding the concentration of nanoparticles and other additives in solution. In its most simple configuration, a UV-Vis system functions by passing a beam of light through the desired sample and measuring the corresponding intensity of the light that is transmitted through and reaches the detector. The measured absorbance (A) is related to the transmission of light according to Equation 2.1

$$A = -\log\left(\frac{\%T}{100\%}\right) \tag{2.1}$$

where transmittance (%T) is calculated as the ratio between the initial intensity of the light source (I_0) and intensity of the light that reaches the detector (I) after passing through the sample (I/I_0). Absorbance is recorded for each component wavelength in the desired spectral range being studied and used to plot the corresponding spectral response. For all tests performed in this thesis, absorbance measurements were recorded using a Cary 60 UV-Vis spectrophotometer system and accompanying software. This system uses a xenon pulse lamp source and two silicon diode detectors with a wavelength accuracy of ± 0.5 nm. Scans were recorded at a rate of 4800 nm/min in the visible range from 400 – 800 nm for both solution-based and solid 3D-printed samples tested. As discussed in Chapter 4, scan rate was not found to influence the recorded absorbance response. A thin film adapter/holder was used to support

3D-printed samples within the UV-Vis system during data collection and testing. Unless otherwise stated, a minimum of three samples/scans were tested to evaluate the absorbance response of the functionalized 3D-printed composites studied in this thesis.

2.6.2 Photoluminescence Response

Similar to absorbance, photoluminescence (PL) provides a metric upon which the optical properties of fluorescent materials can be evaluated. Rather than measuring the amount of light transmitted through a material, PL records the emission of a sample in its excited state. Using an optical excitation source set to a specific wavelength/frequency, samples are irradiated and the corresponding release of energy in the form of light is measured at a secondary detector. This emission of light is called fluorescence. Through the recombination of electron-hole pairs and movement of photons between the conduction and valence bands, information regarding the optical behavior of a material can be evaluated and quantified for a given spectral range.

For all tests performed in this study, PL measurements were recorded using a PTI spectrophotometer and accompanying software. A scan rate of 1 nm/s and 1 nm step size were used for all samples tested. A laser was used as the optical excitation source, where the frequency of excitation was selected based on the material system being studied. For CdSSe QD samples, PL was recorded with an excitation wavelength of 500 nm, and the PL of phosphor samples was recorded at an excitation wavelength of 400 nm. The wavelength specified for the excitation source was chosen to be close to the band gap energy for the specific material system being studied. Following excitation, the emitted light is recorded at the secondary detector, where the intensity is measured at each component wavelength to construct

the final PL spectra. PL measurements were recorded for both quantum dots in solution as well as for quantum dots and phosphors in larger scale, bulk scale 3D-printed parts as discussed in Chapters 3 and 5. In order to ensure repeatability between tests, a custom stand was used to ensure uniform orientation and position between individual scans for 3D-printed thin film samples. Samples were supported at a 45° angle relative to the laser excitation source. Again, a minimum of three samples/scans was tested to evaluate the absorbance response of the functionalized 3D-printed composites studied in this thesis unless otherwise stated.

2.6.3 Electroluminescence Response

Electroluminescence (EL) is defined as the luminescence and corresponding emission of light under the presence of an electrical excitation source. Similar to fluorescence, EL is related to the release of light resulting from the recombination of electron and hole pairs under the presence of an external excitation source; in this case an applied voltage. The EL response of 3D-printed ZnS:Cu alternating current electroluminescent (ACEL) discussed in Chapter 5 was evaluated for various voltage and frequency dependent combinations using a charge-coupled device based spectrometer (Labsphere CDS 600 CCD spectrometer) and accompanying software (OceanView). 3D-printed ACEL devices were excited using a Keysight 10MHz function generator and Krohn-Hite voltage amplification system (model 7500) for frequencies ranging from 10 Hz to 10 kHz and voltages from 150 to 245 V.

Similar to the PL set up described above, the CCD spectrometer used to evaluate 3D-printed ACEL devices functions by recording the intensity of light that is emitted for each component wavelength across the spectral range being studied. As the recorded emission and fluorescence data are recorded in terms of the number of photons hitting the detector (i.e.

counts), the recorded data collected is uncalibrated and does not represent a particular optical power or energy at a specified wavelength. A number of factors including the distance of the spectrometer from the ACEL device sample as well as integration time can impact the recorded EL response for a given sample. In order to address these constraints, the spectrometer was supported at a fixed height above ACEL samples and an integration time of 2.5 sec was used for all testing configurations. A total of five individual ACEL samples was printed and tested to evaluate the EL response of the PLA/phosphor composite developed in this thesis. In order to provide a comparison between the individual samples, the recorded optical response for each sample was normalized according to its maximum EL response. Details of ACEL device fabrication as well as comparison between individual samples are included in Chapter 5.

2.7 Material Characterization

2.7.1 Thermal Response

As a metric to evaluate the underlying response of the functionalized 3D-printed materials, various thermal testing was performed. In particular, both thermogravimetric analysis (TGA) and differential scanning calorimetry (DSC) were used to study the impact that functionalization has on the PLA polymer host matrix. TGA testing is commonly used to provide an indication of changes in physical material properties and overall resistance to degradation with increasing temperature. For the functionalized composites studied, a small sample of the 3D-printed material (~ 0.1 g) is loaded into a platinum reference pan (Instrument Specialists PS2030) and heated from 25 to 500 °C using an Instrument Specialists TGA 1000 under nitrogen purge (100 mL/min). Over time, as temperature is increased, the mass of the sample and any corresponding degradation is recorded. The resulting data is plotted with Mass

(%) on the y-axis and Temperature (°C) on the x-axis (as shown in Figure 3.5). For the PLA composite systems studied in this thesis, a single material degradation step was observed regardless of additive or concentration. In each case, the material loss step occurred at a temperature above those used for materials processing and 3D printing, and is further discussed in Chapters 3 and 4, respectively.

In addition to TGA, DSC offers a second approach for evaluating the thermal response of the functionalized composites studied in this thesis. Instead of evaluating changes in mass with temperature, DSC is used to understand thermal phase transitions such as glass transition temperature, crystallization temperature as well as melting temperature. These phase transitions can provide a direct understanding of polymer chain structure and movement, as variations in the amount of heat flow are recorded for increasing temperatures. When a phase change occurs, the amount of heat required to go from a solid to a liquid, and vice versa, changes. Such differences are recorded as the emergence of peaks, valleys, and shoulders in the recorded DSC response (e.g. Figure 3.6). All DSC testing performed in this thesis was conduced using a TA instruments Q 2000 under nitrogen purge (50 mL/min). Samples were loaded into hermetic aluminum pans (TA Instruments DSC84012) and equilibrated at -25 °C and heated to 225 °C at a rate of 25 °C/min where the temperature was held isothermally for 5 min before being cooled back to -25 °C. A total of three scans were run for each sample, and the corresponding thermal data were recorded from the final scan. Averages and standard deviations for each concentration and weight percent of additive studied were calculated from the three independent scans, where additional discussion can found in Chapter 3.

2.7.2 Mechanical Load Response

Mechanical testing was also studied to evaluate the impact that filament functionalization has on the material response of functionalized 3D-printed composite materials. The tensile load response of 3D-printed dogbone samples was analyzed using an Instron 5944 single column load frame operating in displacement control at a rate of 5 mm/min. ASTM D638 Type V (Standard Test Method for Tensile Properties of Plastics) tensile dogbone samples were fabricated and tested to evaluate the impact that filament functionalization has on the overall mechanical properties of the 3D-printed materials. A minimum of three tensile specimens were averaged to obtain the data presented in this thesis, where all samples were observed to break within their gauge length during testing. Again, it should be noted that all processing parameters including print nozzle temperature, build plate temperature, print layer height, and print layer orientation were kept constant between individual samples in an attempt to minimize any impact on the recorded mechanical response. Relevant mechanical properties including ultimate tensile strength, strain at break, tensile modulus and toughness were evaluated with the data obtained for tensile testing. Additional information and discussion is included in Chapter 3.

2.8 Additional Characterization Methods

Transmission and scanning transmission electron microscopy (TEM/STEM) images for CdSSe QDs and gold nanoparticles in solution and in 3D-printed films were recorded using a Technai Osiris electron microscope. Quantum dots and nanoparticles in solution were drop cast onto a carbon-coated mesh grid, and the residual solvent was allowed to evaporate prior to imaging. 3D-printed polymer samples were prepared using a microtome, where thin slices

(approximately 75 nm in thickness) of PLA/CdSSe and PLA/AuNP samples were cut and supported on a nickel grid prior to imaging. All TEM grids were purchased from TED Pella, Inc. Differential interference contrast (DIC) and white light microscopy images for the PLA/phosphor samples were recorded using a Zeiss Axiovert 200 Inverted Fluorescence Microscope at various ranges of magnification. 3D-printed film thicknesses ranged from 0.1 mm to 0.5 mm. STEM and DIC/WL images and corresponding quantum dot, gold nanoparticle, and phosphor sizes were analyzed using ImageJ software.

Chapter 3

Incorporation of Fluorescent Quantum Dots for 3D Printing and Additive Manufacturing Applications

3.1 Introduction

In this chapter, I present a method for incorporating fluorescent quantum dots within additive manufacturing and 3D printing processes and applications. To the best of my knowledge, the paper I published that comprises this Chapter represents the first such report related to the direct incorporation of quantum dots within FDM-type 3D printing applications.[88] Prior research has focused on the use of ink-jet printing technologies to manufacture and print quantum dot structures on a relatively small scale,[89,90] but the method discussed in this Chapter allows for the direct incorporation and implementation of quantum dots within the additive manufacturing process to enable the agile production of larger-scale parts and structures. As described in the experimental section of Chapter 2, the basis of this approach revolves around the incorporation of cadmium sulfur selenide graded alloy quantum dots (CdSSe QDs) within a polylactic acid (PLA) host matrix through solution-based mixing to manufacture and extrude printer filament compatible with commercially available FDM 3D-printing systems. As a functional demonstration of this new approach, light pipes and fluorescent devices are manufactured using FDM by incorporating the optical response of the embedded CdSSe QDs in the finished parts through the 3D printing process.

A variety of optical, thermal, and mechanical testing and material characterizations are performed on 3D-printed samples to evaluate the effects of functionalization on the underlying properties of both the embedded quantum dots and PLA polymer host matrix. Surface

chemistry considerations, polymer structure, and the overall concentration of embedded quantum dots were all found to impact the underlying material response of the as-printed structures. Establishing an understanding of material behavior following materials processing, functionalization, and printing, as well as the mechanisms that control these observed responses, is a crucial step in the continued development, advancement and understanding of functionalized materials for additive manufacturing and 3D printing applications.

3.2 Experimental Methods

Quantum dot based fluorescent filament compatible with commercially available FDM-type 3D printing systems was fabricated according to the protocol and procedure detailed in the experimental section of Chapter 2. CdSSe QDs were embedded in PLA at various concentrations (i.e. 0% (pure PLA), 0.1%, 0.5%, 1%, 3%, 5%, 7% CdSSe QDs in PLA by weight) and tested to evaluate the impact of functionalization on the material response of the final 3D-printed structures and devices. Additional information relating to the optical, thermal and mechanical testing and characterization is outlined in further detail in Chapter 2.

3.3 Results and Discussion

3.3.1 Optical properties of 3D-printed PLA/CdSSe QD nanocomposites

The as-synthesized CdSSe QDs, with a diameter of 5.7 ± 1.0 nm, confirmed through TEM measurements (Figure A.1), displayed an average quantum yield of 54% and corresponding bright orange color/luminescence with a band-edge absorbance peak near 569 nm and a maximum photoluminescence (PL) emission intensity at 593 nm in solution. Thin

film templates, 0.5 mm in thickness, were fabricated to study the optical properties and characteristics of 3D-printed PLA/CdSSe QD samples at varying concentrations of CdSSe QDs in PLA by weight (Figure 3.1). When incorporated within PLA, the absorbance behavior and response of CdSSe QDs was relatively unchanged, as both the overall spectral shape and absorbance peak location for 3D-printed films remained constant with CdSSe QDs in solution following materials processing and printing (Figure 3.2a and 3.2b, respectively). Additionally, 3D-printed PLA/CdSSe QD films displayed a linear relationship between absorbance intensity (measured at the absorbance peak for CdSSe QDs in solution, i.e. 569 nm) and quantum dot concentration (% of CdSSe QDs in PLA by weight) for the 3D-printed samples studied (Figure 3.2c). This behavior is consistent with Beer-Lambert's Law, which relates the absorbance (A, a.u.) of nanoparticles in solution to concentration (c, mol/L), molar extinction coefficient (ε, $M^{-1}cm^{-1}$), and path length (l, cm) (Eqn. 3.1). For the 3D-printed films, when ε and l (overall film thickness, 0.5 mm) are held constant, a linear relationship between peak absorbance (A, a.u.) and concentration of quantum dots embedded in PLA (c, % of CdSSe QDs in PLA by weight) is obtained.

$$A = \epsilon l c \tag{3.1}$$

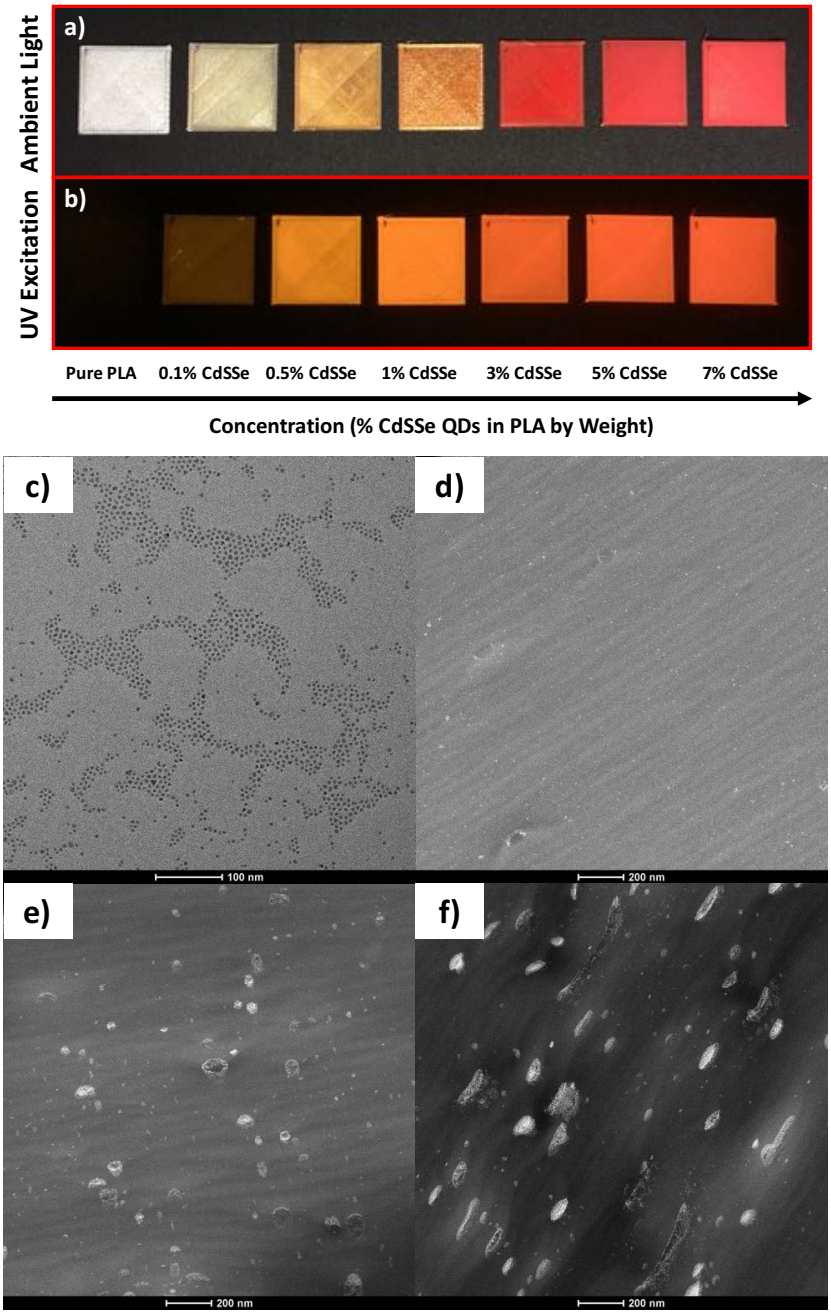

Figure 3.1 3D-printed pure PLA and PLA/CdSSe QD films at varying concentrations of CdSSe QDs in PLA by weight under a) ambient light and b) UV excitation (picture was taken using a UV filter). Corresponding TEM image of c) CdSSe QDs drop cast from solution (approximately 5.7 ± 1.0 nm in diameter, scale bar 100 nm), high angle annular dark field (HAADF) STEM images of d) PLA/CdSSe QD 3D-printed film (0.5% CdSSe QD in PLA by weight, scale bar 200 nm), e) PLA/CdSSe QD 3D-printed film (3% CdSSe QD in PLA by weight, scale bar 200 nm), f) PLA/CdSSe 3D-printed film (7% CdSSe QD in PLA by weight, scale bar 200 nm). Aggregation between individual quantum dots can be seen at increasing concentrations of CdSSe QDs in PLA.

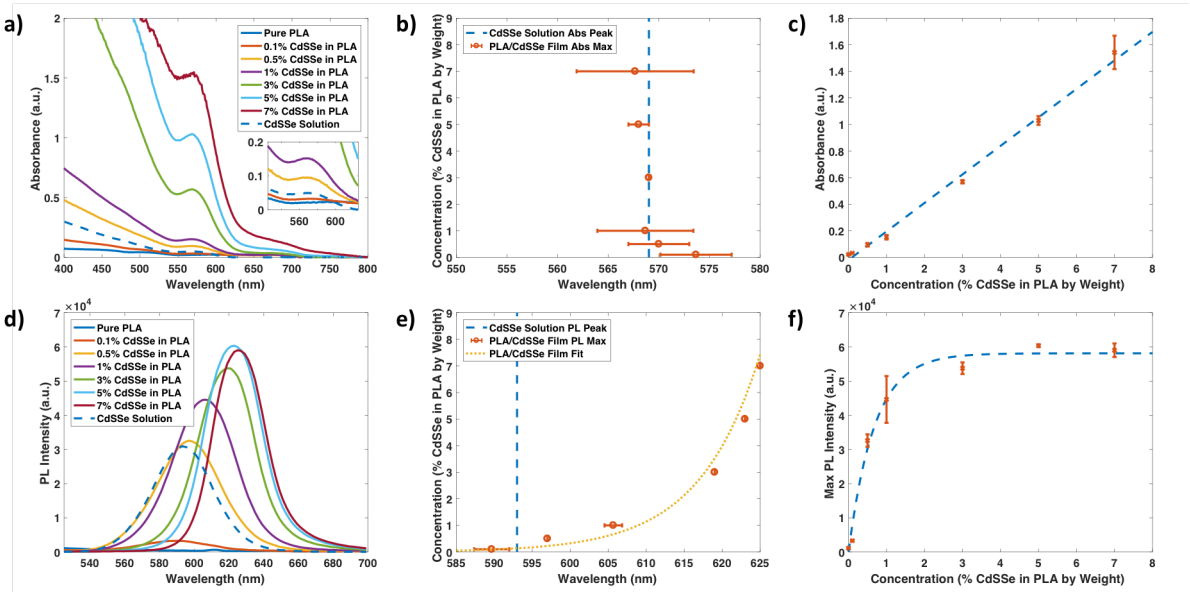

Figure 3.2 a) Average absorbance spectra of 3D-printed PLA/CdSSe QD films at varying concentrations of CdSSe QDs in PLA by weight and CdSSe QDs in solution. b) Location of absorbance peak for 3D-printed PLA/CdSSe QD films at varying concentrations of CdSSe QDs in PLA by weight. c) Relationship between absorbance intensity (measured at absorbance peak for CdSSe QDs in solution, 569 nm) and concentration of CdSSe QDs in PLA by weight. d) Average photoluminescence spectra of 3D-printed PLA/CdSSe QD films at varying concentrations of CdSSe QDs in PLA by weight and CdSSe QDs in solution. e) Location of maximum photoluminescence for 3D-printed PLA/CdSSe QD films at varying concentrations of CdSSe QDs in PLA by weight. f) Relationship between maximum photoluminescence intensity and concentration of CdSSe QDs in PLA by weight.

The photoluminescence (PL) emission properties of 3D-printed PLA/CdSSe QD thin films was also evaluated. Though the overall monochromatic behavior of CdSSe QDs in solution was maintained following printing, a significant red shift in the location of maximum PL intensity was observed for increasing concentrations of CdSSe QDs in PLA (Figure 3.2d and 3.2e, respectively). For the highest concentration studied (7% CdSSe in PLA by weight), the location of maximum PL intensity was red-shifted by 32 nm relative to CdSSe QDs in solution. This spectral red shift is attributed to a combination of two factors previously illuminated in the literature: quantum dot aggregation in 3D-printed PLA/CdSSe QD films,

and the presence of multiple size populations in the as-synthesized graded alloy CdSSe QDs enabling energy transfer from small to larger sized quantum dots in aggregated form.[91,92]

In order to quantify the degree to which quantum dot aggregation influenced the observed optical response, high angle annular dark field (HAADF) STEM images were recorded for 3D-printed PLA/CdSSe QD structures. According to prior research, a direct relationship between aggregation and the recorded spectral shift is expected.[91] At low concentrations (i.e. 0.5% CdSSe in PLA by weight), minimal aggregation was observed, and CdSSe QDs were well dispersed throughout the 3D-printed structure (Figure 3.1d). Relative to CdSSe QDs in solution, the location for maximum PL emission was red-shifted by 4 nm for the 0.5% PLA/CdSSe QD 3D-printed sample (Figure 3.2e). At higher concentrations of CdSSe QDs in PLA (i.e. 3% and 7% CdSSe QDs in PLA by weight), though, distinct aggregation between individual quantum dots within the 3D-printed structures was confirmed (Figure 3.1e and 3.1f). In these samples, embedded CdSSe QDs existed primarily in larger, aggregated structures ranging in size from 49 ± 24 nm to 70 ± 54 nm, where the location of max PL intensity red shifted 26 nm and 32 nm for 3% and 7% CdSSe QDs in PLA by weight, respectively.

With increasing concentrations of embedded quantum dots and the resultant aggregation in 3D-printed PLA/CdSSe QD films, energy transfer between the multiple size populations in as-synthesized CdSSe QDs is expected to drive the observed spectral red shift (Figure 3.2d and 3.2e). This energy transfer, and corresponding reabsorption, is displayed by a narrowing of the full width at half maximum (FWHM) of the PL emission spectra for increasing concentrations of CdSSe QDs in PLA (Figure 3.3). Here, the lower wavelength emission associated with smaller quantum dots in the nanofunctionalized composite decreases,

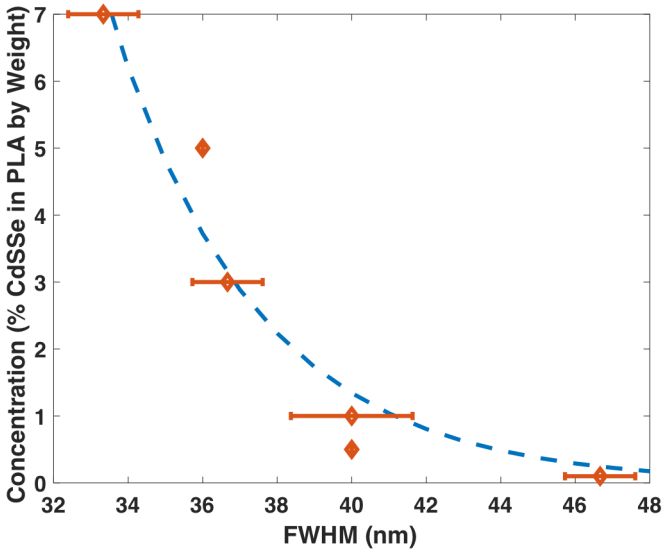

Figure 3.3 Full width half maximum (FWHM) analysis of photoluminescence spectra for PLA/CdSSe QD 3D-printed films at varying concentrations of of CdSSe QDs in PLA by weight.

as its emission is reabsorbed by surrounding, larger CdSSe QDs, and the overall spectral response begins to be dominated by the higher wavelength component of the quantum dot emission. The spectral red shift observed for 3D-printed PLA/CdSSe QD films is expected to continue to plateau with increasing concentrations of quantum dots, as indicated by the trends obtained for the samples studied in this Chapter.

Similar to the observed spectral red shift, the overall maximum PL intensity of 3D-printed PLA/CdSSe QD films was also found to be concentration dependent. Near a 3% by weight loading, max PL intensity begins to reach a steady state for increasing concentrations of CdSSe QDs in PLA (Figure 3.2f). These results are similar to previously reported findings, where the emission intensity of ultra-small cadmium selenide quantum dots embedded within polymeric films began to approach a maximum value with increasing concentration of quantum dots.[84] These trends can be attributed to aggregation in the 3D-printed structures, and

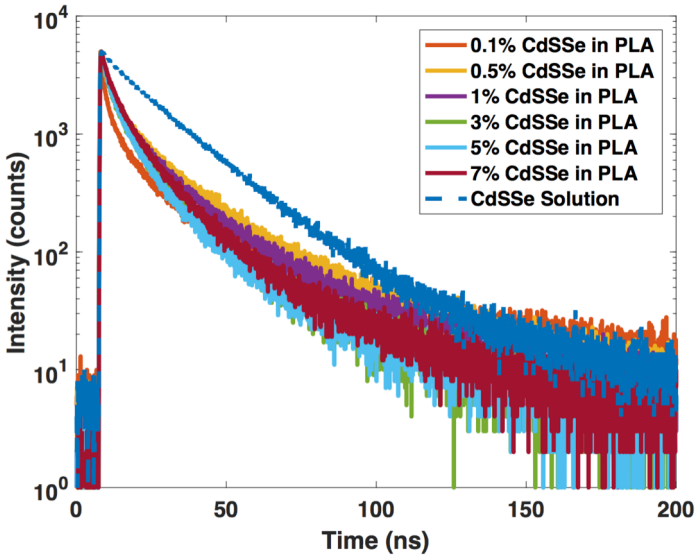

Figure 3.4 Lifetime analysis of 3D-printed PLA/CdSSe QD films and CdSSe QDs in Solution

a corresponding reduction in quantum efficiency of the aggregated quantum dots occurs due to their close proximity.

Beyond absorbance and emission characteristics, fluorescence lifetime measurements of CdSSe QDs in solution and 3D-printed PLA/CdSSe QD films were also evaluated. Decay curves were fit to a three-component exponential function, and the lifetimes of PLA/CdSSe QD films were found to be shorter than that of CdSSe QDs in solution (see Appendix A). Again, this behavior can be attributed to the increase in aggregation and energy transfer between the multiple size populations present in the PLA/CdSSe QD 3D-printed samples (Figure 3.4).[93,94]

3.3.2 Thermal properties 3D-printed of PLA/CdSSe QD nanocomposites

The thermal stability of PLA/CdSSe QD nanocomposite systems was studied using thermogravimetric analysis. Residual weight versus temperature for 3D-printed pure PLA and PLA/CdSSe QD samples are shown in Figure 3.5. All samples, regardless of CdSSe QD concentration, displayed a single weight loss step beginning near 250 °C, followed by complete material loss occurring above 350°C. With material extrusion/filament fabrication and 3D printing operating temperatures of 180°C and 215°C, respectively, thermogravimetric analysis confirms the thermal stability of PLA/CdSSe QD nanocomposites in the operating temperature range, and that minimal material degradation or loss occurs during both the filament fabrication and 3D printing processes.

The thermal response of 3D-printed PLA/CdSSe QD nanocomposites was further studied using differential scanning calorimetry to better understand the behavior of the polymer chain network and overall impact that filament functionalization has relative to the unmodified PLA host matrix. Representative differential scanning calorimetry scans for 3D-printed pure PLA and PLA/CdSSe QD samples are shown in Figure 3.6a. Average values for glass transition temperature (T_g), crystallization temperature (T_c) and melting temperature (T_m) are plotted in Figure 6b and further detailed in Table 3.1. With increasing concentrations of CdSSe QDs in PLA, glass transition, crystallization and melting temperatures were all observed to decrease relative to the unmodified pure PLA following materials processing and 3D printing, with more significant decreases in the recorded thermal transitions occurring at higher concentrations of CdSSe QDs in PLA (Figure 3.6b).

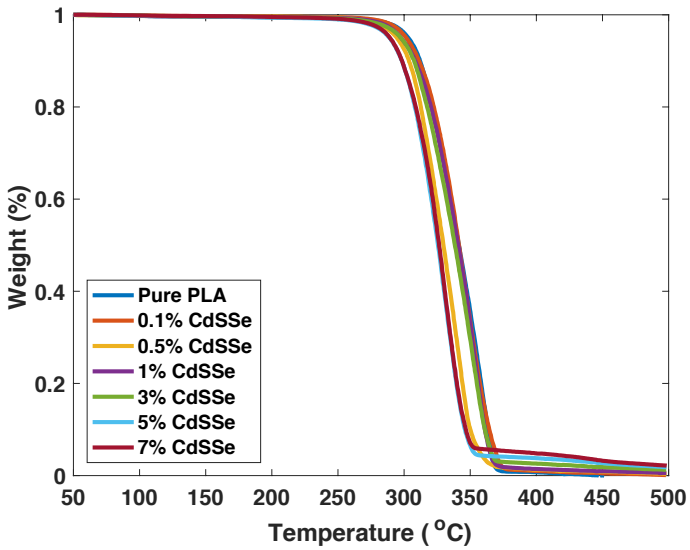

Figure 3.5 Thermogravimetric analysis response of 3D-printed pure PLA and PLA/CdSSe QDs films at various concentrations of CdSSe in PLA by weight (0.1%, 0.5%, 1%, 3%, 5%, 7%). All films studied showed good thermal stability in the range of temperatures used for materials processing and 3D-printing.

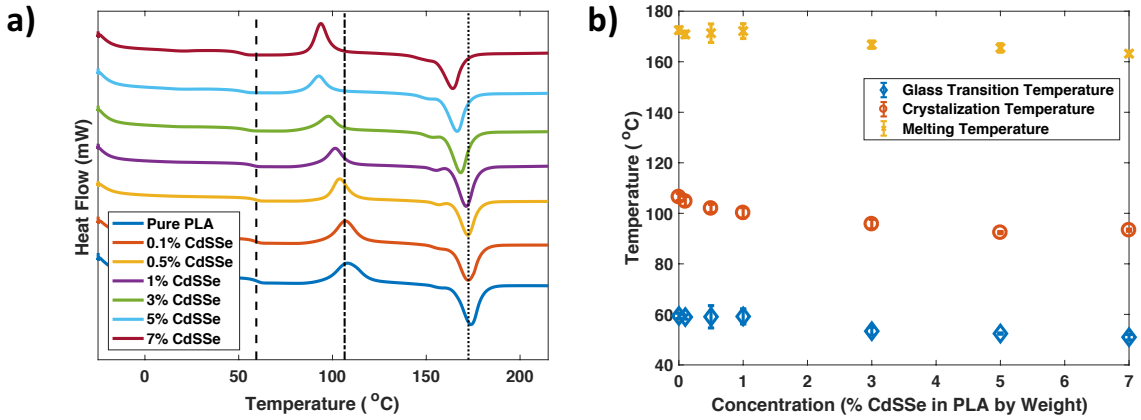

Figure 3.6 a) Representative differential scanning calorimetry curves for 3D-printed pure PLA and PLA/CdSSe QD samples at various concentrations of CdSSe QDs in PLA by weight. Dashed lines are guides for the eye and represent average values of pure PLA glass transition temperature, crystallization temperature and melting temperature, from left to right respectively. b) Average glass transition temperature, crystallization temperature and melting temperature for 3D-printed pure PLA and PLA/CdSSe QDs at various concentrations of CdSSe QDs in PLA by weight (data is further detailed in Table 3.1).

Table 3.1 Differential scanning calorimetry results

	Glass Transition Temperature (°C)	Crystallization Temperature (°C)	Melting Temperature (°C)
Pure PLA	59.4 ± 1.0	106.5 ± 1.4	172.5 ± 1.3
0.1% CdSSe QD in PLA	59.0 ± 0.8	104.7 ± 1.9	170.8 ± 1.3
0.5% CdSSe QD in PLA	59.1 ± 4.4	101.9 ± 1.6	171.3 ± 3.7
1% CdSSe QD in PLA	59.2 ± 3.0	100.2 ± 2.1	172.1 ± 2.9
3% CdSSe QD in PLA	53.4 ± 1.5	95.7 ± 1.9	166.8 ± 1.5
5% CdSSe QD in PLA	52.4 ± 0.3	92.4 ± 0.4	165.5 ± 1.7
7% CdSSe QD in PLA	51.0 ± 1.1	93.3 ± 0.4	163.2 ± 1.0

These changes in thermal transition can be attributed to a combination of two underlying mechanisms: 1) interactions between the PLA host matrix and natively bound surface ligands present on CdSSe QDs, and 2) aggregation and agglomeration between CdSSe QDs in the final 3D-printed structure. Surface ligand-polymer chain interactions are known to have a significant impact on the overall behavior of polymer-based nanocomposite systems. For attractive interactions, thermal transitions, namely glass transition temperature, are typically observed to increase when compared to the unmodified host matrix even at relatively high concentrations of embedded nanomaterials.[95] This behavior is due in part to embedded nanoparticles chemically interacting with and binding to the surrounding polymer host matrix, restricting polymer motion due to an increased energy barrier for intermolecular chain movement.[96] In the case of 3D-printed PLA/CdSSe QD nanocomposites, though, the opposite trend is observed. This behavior is attributed to poor interactions between the pure PLA chain network and oleic acid surface ligands present on the embedded CdSSe QDs. Fatty acids, such

as oleic acid, consisting of a long hydrocarbon chain and terminal carboxyl group, have been previously reported to act as a plasticizing agents when incorporated within a pure PLA host matrix.[97] Plasticizing agents are known to lower glass transition temperature, as well as crystallization and melting temperatures, by effectively allowing for improved polymer chain mobility and alignment.[98] It is expected that the methyl-rich surface of the oleic acid-modified CdSSe QDs interacts weakly through Van der Waals forces with the PLA polymer chain network. As such, I hypothesize that the lack of strong intermolecular interactions between oleic acid and PLA results in the formation of additional free surfaces and free spaces near embedded quantum dots, as PLA is unable to adequately wet the surface of oleic acid-capped CdSSe QDs.

In addition to the aforementioned impact of native surface ligands, the size and concentration of embedded nanomaterials, including the presence of aggregates, has also been found to influence the overall thermal response of polymer-based nanocomposite systems.[99–101] As discussed previously, CdSSe QDs were observed to form aggregates in micelle-like structures at increasing concentrations of quantum dots in PLA (Figure 3.1). With weak chemical interactions between the surrounding polymer matrix, aggregated quantum dots can be thought of as acting as void spaces in the 3D-printed PLA/CdSSe QD nanocomposite systems. The presence of voids at nanoparticle-polymer interfaces have been found to reduce the glass transition behavior of polymer-based nanocomposite systems due to the resultant increased polymer mobility near the regions surrounding embedded nanomaterials.[96] Thermal transitions of 3D-printed PLA/CdSSe QD nanocomposites are expected to decrease with increasing aggregate size due to the formation of larger polymer chain discontinuities and the

resultant formation of interphase regions near quantum dot surfaces resulting from weak polymer-nanoparticle interactions, consistent with the trends obtained in this study.[102]

3.3.3 Mechanical properties of 3D-printed PLA/CdSSe QD nanocomposites

The tensile load responses of 3D-printed pure PLA and PLA/CdSSe QD samples were studied to evaluate the impact of filament functionalization on the mechanical properties of as-printed PLA/CdSSe QD nanocomposites. The presence of CdSSe QDs in 3D-printed dogbone samples is visible under both ambient light, where samples maintained the orange coloration

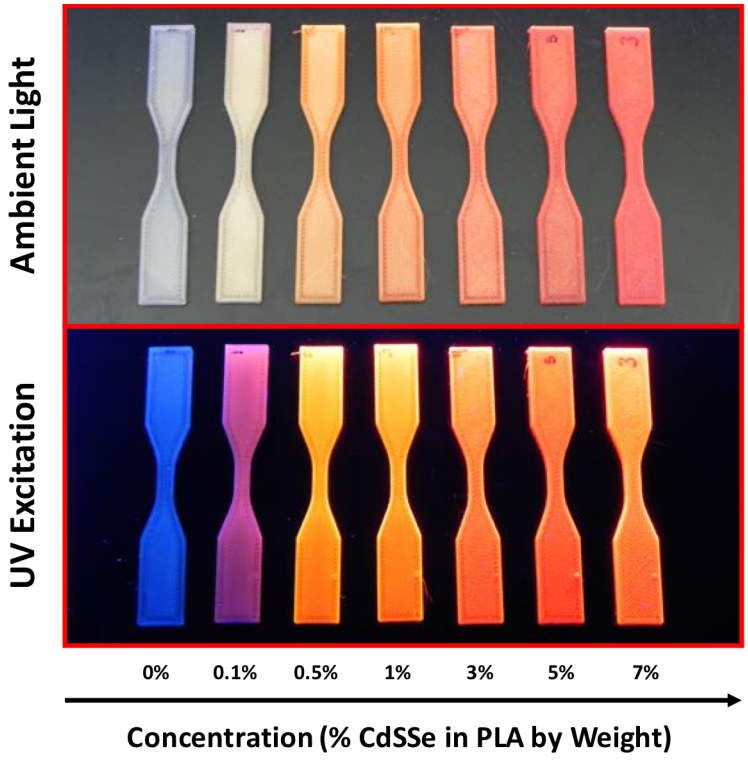

Figure 3.7 3D-printed ASTM D638 Type V tensile dogbone specimen with varying of concentration of CdSSe in PLA by weight under ambient light and UV excitation (top and bottom, respectively).

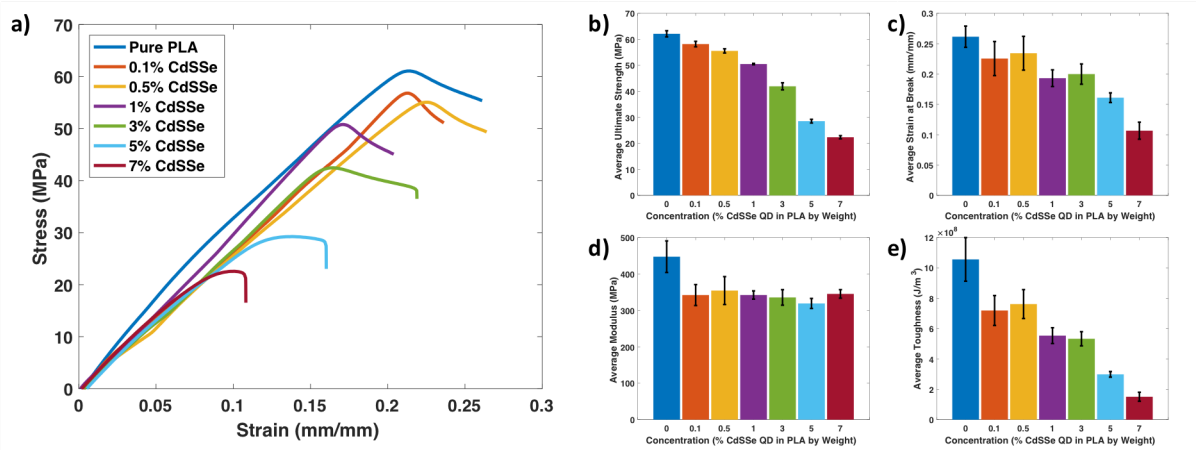

Figure 3.8 Tensile load response of 3D-printed pure PLA and PLA/CdSSe QD dogbone specimens. a) Representative stress vs. strain curves for varying concentrations of CdSSe QDs in PLA by weight. b) Average ultimate strength for varying concentrations of CdSSe QDs in PLA by weight. c) Average strain at break for varying concentrations of CdSSe QDs in PLA by weight. d) Average modulus for varying concentrations of CdSSe QDs in PLA by weight. e) Average toughness for varying concentrations of CdSSe QDs in PLA by weight.

of CdSSe QDs in solution, and UV excitation, where the fluorescent behavior of the embedded quantum dots was preserved following materials processing and 3D printing (Figure 3.7). It should be noted that the purple coloration of the pure PLA and 0.1% PLA/QD samples is a result of reflection from the backlight source, as the image was not taken with a UV filter. Representative stress vs. strain curves for 3D-printed pure PLA and PLA/CdSSe QD dogbone specimens loaded in tension are shown in Figure 3.8a. A summary of relevant mechanical testing results, including average ultimate tensile strength, average strain at break, as well as average elastic modulus and toughness for all samples tested is presented in Figure 3.8 and further detailed in Table 3.2.

Table 3.2 Mechanical properties of 3D-printed pure PLA and PLA/CdSSe QD tensile test specimen

	Average Ultimate Tensile Strength (MPa)	**Average Strain at Break (mm/mm)**	**Average Tensile Modulus (MPa)**	**Average Toughness ($x10^8$ J/m^3)**
Pure PLA	62 ± 1.0	0.26 ± 0.02	447 ± 43	11 ± 1.4
0.1% CdSSe QD in PLA	58 ± 1.0	0.23 ± 0.03	342 ± 29	7.2 ± 0.99
0.5% CdSSe QD in PLA	55 ± 0.81	0.23 ± 0.03	354 ± 38	7.6 ± 0.95
1% CdSSe QD in PLA	50 ± 0.26	0.19 ± 0.01	342 ± 11	5.5 ± 0.52
3% CdSSe QD in PLA	42 ± 1.0	0.20 ± 0.02	336 ± 21	5.3 ± 0.47
5% CdSSe QD in PLA	29 ± 0.71	0.16 ± 0.01	319 ± 14	3.0 ± 0.19
7% CdSSe QD in PLA	22 ± 0.60	0.11 ± 0.01	345 ± 12	1.5 ± 0.30

Similar to the results obtained for differential scanning calorimetry testing, the mechanical load response of 3D-printed PLA/CdSSe QD specimens was found to be dependent on the overall concentration of embedded quantum dots. For the tensile dogbone specimens, ultimate strength, strain, modulus and toughness were all observed to decrease relative to pure PLA following the inclusion of CdSSe QDs within the 3D-printed structures. The largest decrease in material strength properties were, on average, observed for the highest concentrations of embedded quantum dots. In fact, ultimate strength and fracture toughness for PLA/CdSSe QD samples containing 7.0% quantum dots by weight were found to decrease by 63% and 85%, respectively, relative to the unmodified pure PLA matrix. these changes in material strength properties are again attributed to to a combination of weak polymer-surface ligand interactions and quantum dot aggregation present in the final 3D-printed structures.

Upon initial inspection of the recorded thermal and mechanical testing results, the embedded quantum dots appear at first to be acting as a plasticizing agent. For polymer based systems, and PLA in particular, the addition of plasticizers has been shown to decrease both the ultimate tensile strength and tensile modulus, consistent with the results obtained for 3D-printed PLA/CdSSe QD samples.[103,104] By promoting intermolecular chain movement, plasticizers are also well known to cause increased deformation for thermoplastic materials. In the case of the 3D-printed PLA/CdSSe QD nanocomposite system, though, elongation at break was observed to decrease, resulting in a more brittle material response with increasing concentrations of embedded quantum dots; this is the opposite effect of what is typically observed for plasticized polymer systems.

At low concentrations of embedded quantum dots (i.e. 0.1% and 0.5% CdSSe QDs in PLA), no statistical difference in the recorded strain response was observed relative to the unmodified pure PLA host matrix, as samples had overlapping standard deviations. These samples also displayed the smallest changes in recorded ultimate strength and toughness, as the low concentrations of embedded quantum dots have limited impact on the polymer chain network. The formation of aggregates and agglomerates in polymer-based nanocomposite structures, however, has been shown to significantly influence the underlying polymer structure and resulting thermal and mechanical behaviors. The presence of aggregates in a polymer matrix, such as those observed in 3D-printed PLA/CdSSe QD structures at higher concentrations of embedded quantum dots, can act as sites for crack initiation and propagation that ultimately lead to the premature and brittle failure of nanocomposite systems.[105] The combined contribution of aggregation and the overall lack of interaction between oleic acid-capped CdSSe QDs and surrounding PLA host matrix significantly reduces the ability of 3D-

printed PLA/CdSSe QD nanocomposites to carry mechanical load. The resultant outcome is a decreased ultimate tensile strength and strain at failure, where aggregated quantum dots ultimately form representative void spacings within the PLA host matrix.

The impact of quantum dot functionalization on the recorded modulus and toughness of PLA/CdSSe QD samples should also be noted. Modulus is commonly defined as the ability of a material to deform elastically under the application of external load, and it offers a means to measure corresponding stiffness of the material. Modulus for PLA/CdSSe QD samples was recorded directly during tensile testing as the slope of the linear component of the stress-strain curve (Figure 3.8a). Following the addition of CdSSe QDs to the PLA host matrix, a decrease in the recorded modulus was observed. Unlike other thermal and mechanical testing results, modulus did not appear to be dependent upon the overall concentration of embedded quantum dots. Rather, a single drop in modulus of approximately 25% relative to unmodified pure PLA was observed. These results are in line with previously reported polymer-nanocomposite systems where increased polymer chain mobility due to the presence of embedded nanomaterials resulted in a decreased modulus due to the lack of intermolecular interactions present at the surface of the embedded quantum dots.[106,107]

Toughness was calculated as the integral under the stress-strain curve, and correlates to the ability of a material to absorb energy when loaded. Typically, ductile materials are thought of as being 'tougher' as they are able to absorb energy over longer periods of time due to increased elongation before failure. With increasing concentration of CdSSe QDs in PLA, a significant decrease in material toughness was observed. In line with the reduced ultimate strength and strain at failure, material toughness decreases in accordance with the overall concentration of embedded quantum dots. This reduction in capacity to absorb energy results

from quantum dot aggregation and a corresponding inability to carry load due to the poor intermolecular interactions between the CdSSe QDs and the surrounding PLA matrix.[106]

3.3.4 3D-printed PLA/CdSSe QD light devices

In order to demonstrate a significant potential application for 3D-printed PLA/CdSSe QD nanocomposite systems, hollow U-shaped optical light pipes were fabricated (Figures 3.9a and 3.9b).[108] Light pipes are components and devices that are used to transport or redirect light from a source to a desired location.[109] Proof-of-concept light pipes were 3D-printed using an inner shell of PLA/CdSSe QD functionalized material (0.5% and 3.0% CdSSe QDs in PLA by weight), surrounded by a white PLA exterior to aid with internal reflection of the quantum dot emission. Although the light pipe does not currently operate using total internal reflection, it is believed to transport light through a combination of reflection and scattering. Future studies are to be completed in order to increase the amount of internal reflection in the 3D-printed device. Methods to achieve this goal will focus on printing a surrounding layer with a higher refractive index polymer than the PLA, or to coat the PLA/CdSSe QD layer with a reflective material. When excited with an external emission source, a red shift in the location of maximum PL emission relative to quantum dots in solution was observed for the light pipe devices tested, similar to trends observed for PLA/CdSSe QD thin film samples discussed previously (Figure 3.9c). Opposite from the trends displayed for 3D-printed PLA/CdSSe QD thin films, though, the PL emission intensity for the optical light pipe was observed to decrease with increasing concentration of embedded quantum dots (i.e. as the weight percent of CdSSe QDs in PLA increased from 0.5% to 3.0%). This response can be attributed to the attenuation

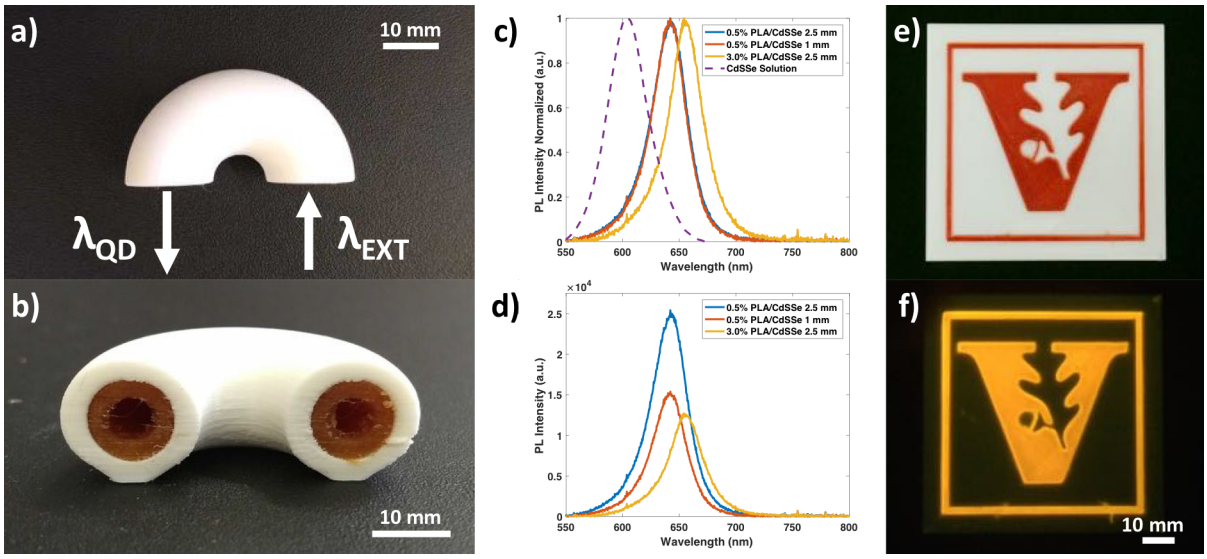

Figure 3.9 3D-printed optical light pipe. a) Top view. b) Profile view, thickness of interior PLA/CdSSe QD layers tested was 1 mm and 2.5 mm, respectively. c) Normalized PL spectra for CdSSe QD solution and 3D-printed PLA/CdSSe QD optical light pipes. d) PL spectra for 3D-printed PLA/CdSSe QD optical light pipes. e) 3D-printed fluorescent device under ambient light. f) 3D-printed fluorescent device under UV excitation (picture was taken using a UV filter).

of quantum dot emission due to the increased number of quantum dots absorbing light in the 3.0% PLA/CdSSe QD light pipe as compared to the 0.5% PLA/CdSSe QD light pipe.[110] Additionally, as the thickness of the PLA/CdSSe QD inner layer was reduced, the recorded PL emission intensity was observed to decrease (Figure 3.9d). This trend is attributed to the decrease in absorption cross-section and corresponding reduction in the overall number of quantum dots along the excitation path. By tuning the size, concentration and type of embedded quantum dots, as well as the thickness of the inner quantum dot-functionalized layer, a customized optical light pipe with tunable emission wavelength and intensity can be obtained by 3D-printing.

Additionally, as a second example of a representative application for 3D-printed light device, a Vanderbilt logo was printed using PLA/CdSSe QD filament encased within a white

PLA surround (Figures 3.9e and 3.9f). This device represents the capability of 3D-printing to fabricate bulk-scale fluorescent displays, devices, and passive structures using multiple materials.

3.4 Conclusions

In this Chapter, the ability to develop functionalized nanocomposite materials compatible with 3D printing applications through the incorporation of CdSSe QDs within a PLA host matrix was demonstrated. Focusing on materials processing considerations, CdSSe QDs and PLA were mixed, dried and extruded to obtain filament compatible with stock fused deposition modeling (FDM) type 3D printers. The optical, thermal and mechanical responses of 3D-printed CdSSe QD structures were studied to evaluate the impact that filament functionalization has relative to the unmodified PLA polymer host matrix. While the overall absorbance behavior of CdSSe QDs was maintained following printing, slight changes in the photoluminescent behavior was observed for 3D-printed CdSSe QD structures. Most noticeable was the red shift in maximum PL emission intensity for increasing concentrations of embedded CdSSe QDs. This spectral shift was attributed to a combination of aggregated quantum dots within the 3D-printed structures and corresponding reabsorption resulting from multiple size populations within embedded quantum dots. The thermal and mechanical behaviors of 3D-printed PLA/CdSSe QD test specimens were also found to be dependent on the overall concentration of embedded quantum dots. In this case, reductions in thermal transitions and material strength properties are attributed to the presence of aggregated quantum dots and the overall lack of interaction between the natively bound oleic acid surface ligands present on CdSSe QDs and the surrounding PLA host matrix. By tuning the surface

composition of the embedded quantum dots to promote favorable interactions with the polymer host matrix, future research will focus on the development of quantum dot based 3D-printed nanocomposite systems with enhanced optical and mechanical strength properties. The ability to incorporate quantum dots and within 3D printing and additive manufacturing processes represents an initial first step in the design, development, and expansion of new materials systems combatable with additive manufacturing applications. Utilizing the insights gained from the materials processing procedure and optical, thermal, and mechanical testing that was performed for 3D-printed PLA/CdSSe QD composites, the following Chapters will focus on the demonstration of additional material systems with enhanced, multifunctional behaviors and properties for a variety of applications and uses.

Chapter 4

Nondestructive Evaluation and Detection of Defects in 3D-Printed Materials Using the Optical Properties of Gold Nanoparticles

4.1 Introduction

Building upon the work with 3D-printed quantum dot-based nanocomposite systems discussed in the previous Chapter, a novel method that addresses a critical scientific barrier encountered in these emerging materials and systems is presented in this Chapter; 3D printing produces hidden defects that are not readily detected. Being highly composite in nature, the layer-by-layer deposition process used in additive manufacturing presents ample opportunities for the formation of defects and discontinuities. In both plastics and metals, the presence of defects arising from 3D printing have been shown to reduce the overall strength and performance of as-printed parts and materials.[111–116] Such defects typically arise in the form of missing print layers resulting from a clogged print nozzle or under extrusion during the printing operation, and defects vary in size based on the 3D printing system being used.[117,118] Concerns related to cyber attacks on additive manufacturing systems have also indicated the potential for the introduction of intentional and malicious defects or flaws within additively manufactured components and parts.[119–121] To date, the nondestructive inspection and evaluation of 3D-printed materials for such defects has been limited to a handful of techniques, and is still a relatively new and emerging field of research.[122–127] Inspection of 3D-printed parts is crucial to prevent designs from being overly conservative and for quality control purposes to help ensure that as-printed parts meet all design specifications. The development of sensing methodologies to detect and monitor the presence of material defects produced

during the AM process is needed to enable the adoption of 3D-printing such that the quality of 3D-printed parts and structures can be assured.[128]

The new method that I have published and is presented here detects the presence of defects in 3D-printed structures based on the absorbance of gold nanoparticles through a nondestructive approach.[24] Similar to the work described in Chapters 2 and 3, gold nanoparticles are again incorporated within a PLA host matrix through a solution-based mixing approach, and samples with at least one dimension on the millimeter-scale with varying number of missing print layers are fabricated. By harnessing the optical properties of the embedded gold nanoparticles, in accordance with trends predicted by Beer-Lambert's Law, the presence of defects in as-printed structures are shown to be detected, localized and quantified based on nondestructive absorbance measurements alone.

4.2 Experimental Methods

Samples with varying weight percent of embedded gold nanoparticles (0% (i.e. pure PLA), 0.05%, 0.1% and 0.2% by weight) were fabricated to study the overall impact that concentration has on the optical properties of the 3D-printed nanofunctionalized composite material. Additional details related to filament fabrication and sample preparation are included in Chapter 2.

4.3 Results and Discussion

Dodecanethiol-stabilized gold nanoparticles (AuNPs), with an average diameter of 4.39 ± 0.93 nm confirmed through TEM measurements (Figure 4.1a), were synthesized according to previously reported protocols (Chapter 2).[82,83] Prior to filament fabrication and

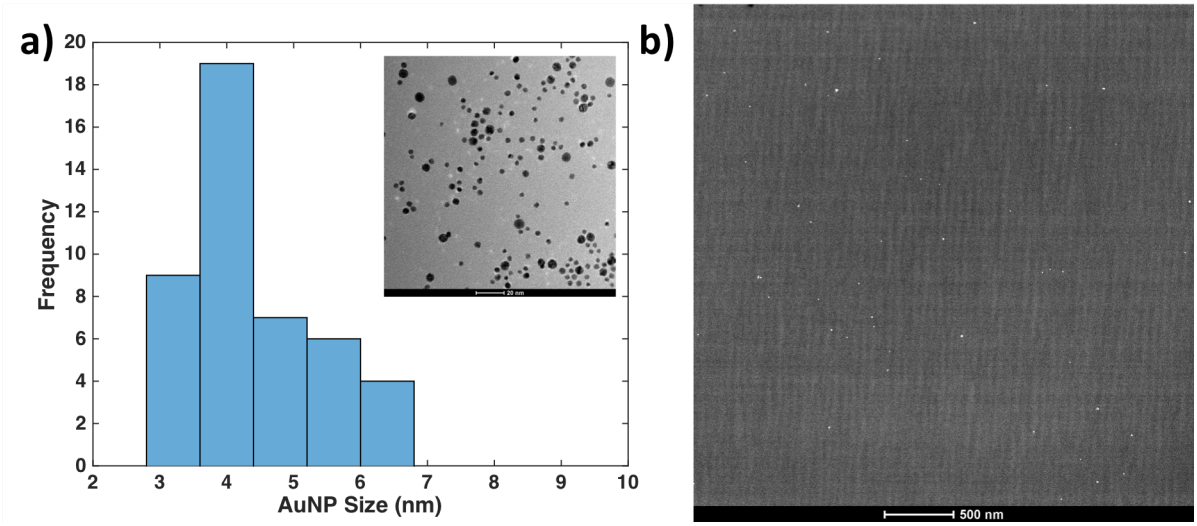

Figure 4.1 a) Histogram and TEM image of as-synthesized AuNPs, with an average size of 4.39 ± 0.93 nm after mixing. b) TEM image of 3D-printed PLA/AuNP film (0.1% weight/weight AuNP in PLA). AuNPs, bright spots in image, are well dispersed throughout the PLA matrix following materials processing, extruding and 3D printing.

incorporation within the PLA host matrix, miscibility of the PLA/AuNP mixture was confirmed through the resuspension of AuNPs in dichloromethane. Following solvent transfer, the optical properties and absorbance response of AuNPs in dichloromethane was unchanged when compared to their recorded response in toluene (Figure 4.2a). Additional solvents commonly used to dissolve PLA including chloroform, tetrahydrofuran, pyridine and acetone were also evaluated with dodecanethiol-stabilized AuNPs to further investigate the impact of solvent transfer on the optical properties of AuNPs.[36] It was found that AuNPs were miscible with chloroform and tetrahydrofuran, in addition to toluene and dichloromethane, but not pyridine or acetone (Figure 4.2b). Mutual miscibility between the respective polymer solvent and nanoparticle system, i.e. AuNPs suspended in dichloromethane, is a crucial consideration in the design of nano-functionalized materials for 3D-printing applications as discussed in Chapter 2.

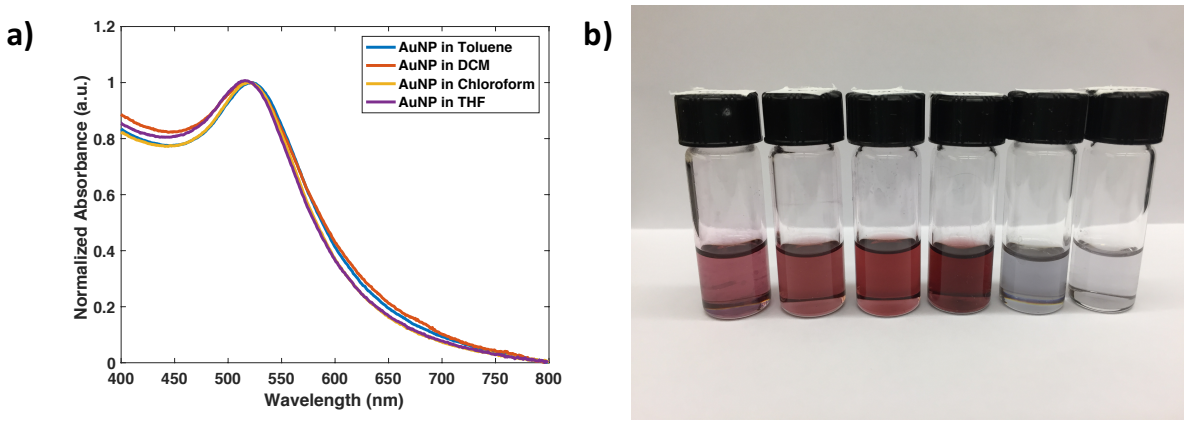

Figure 4.2 Optical response of AuNPs suspended in various solvents; a) Normalized absorbance spectra for AuNPs suspended in various solvents known to dissolve PLA. Minimal change in absorbance spectra and location of SPR peak is observed for AuNP in dichloromethane (DCM), chloroform and tetrahydrofuran (THF). b) From left to right, solutions of AuNPs suspended in toluene, dichloromethane, chloroform, tetrahydrofuran, pyridine and acetone. Miscibility of AuNPs in toluene, dichloromethane, chloroform and tetrahydrofuran is indicated by the purple coloration of nanoparticle solution.

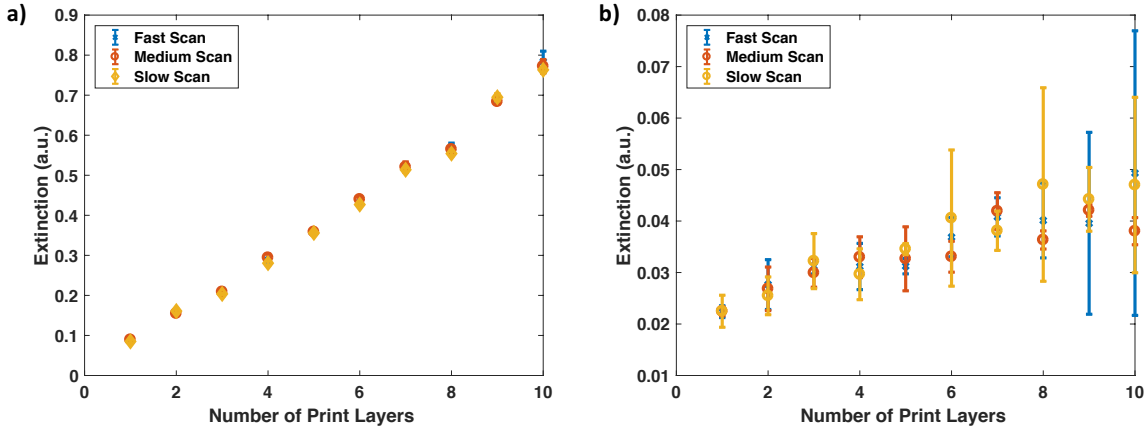

Figure 4.3 Absorbance of (a) PLA/AuNP and (b) pure PLA 3D-printed films measured at different scan rates recorded at 521 nm. Scan rates of 4800 nm/min, 2400 nm/min and 1200 nm/min for fast, medium and slow scans, respectively, were studied.

Thin films of pure PLA and PLA/AuNPs at varying concentrations of embedded nanoparticles were fabricated to study the optical response of AuNPs following materials processing and 3D printing (Figures 4.4e and 4.6a). A total of 15 scans, recorded from five individual samples and measured at three distinct locations, were statistically analyzed to

obtain the average absorbance and error bars herein presented. Absorbance measurements were recorded at a rate of 4800 nm/min in the visible range from 400 – 800 nm, where the corresponding response was found to be independent of the scan rate used for data collection (Figure 4.3). Due to scattering present in the 3D-printed films, the y-axis on all absorbance spectra recorded using the UV-Vis setup are labeled as 'Extinction (a.u.)' in order to better represent the combined effect of absorbance and any scattering present in the recorded spectral measurements.

Overall, the optical response and characteristics of AuNPs in solution are preserved following materials processing and printing, as 3D-printed films displayed a purple coloration consistent with AuNPs in solution and no change in the overall shape or behavior of the recorded absorbance spectra was observed for films with varying number of print layers (Figures 4.2 and 4.4). These results are in line with those reported for the absorbance response of PLA/CdSSe QD samples discussed in Chapter 3. Due to the quantum dot aggregation observed in Chapter 3, PLA/AuNP samples were fabricated at much lower concentration, to ensure AuNPs would be well dispersed with minimal aggregation in as-printed films. This behavior was confirmed through TEM measurements of the 3D-printed PLA/AuNP films (Figure 4.1b). 3D-printed pure PLA films are clear/white and have minimal absorbance across the visible spectrum regardless of the total number of print layers tested, consistent with previously reported results (Figures 4.4e and 4.4f).[129,130] The noise in the absorbance spectra for both pure PLA and PLA/AuNP specimens is attributed to the physical structure of the as-printed films, as the layer-by-layer deposition process introduces a number of locations for increased light scattering.

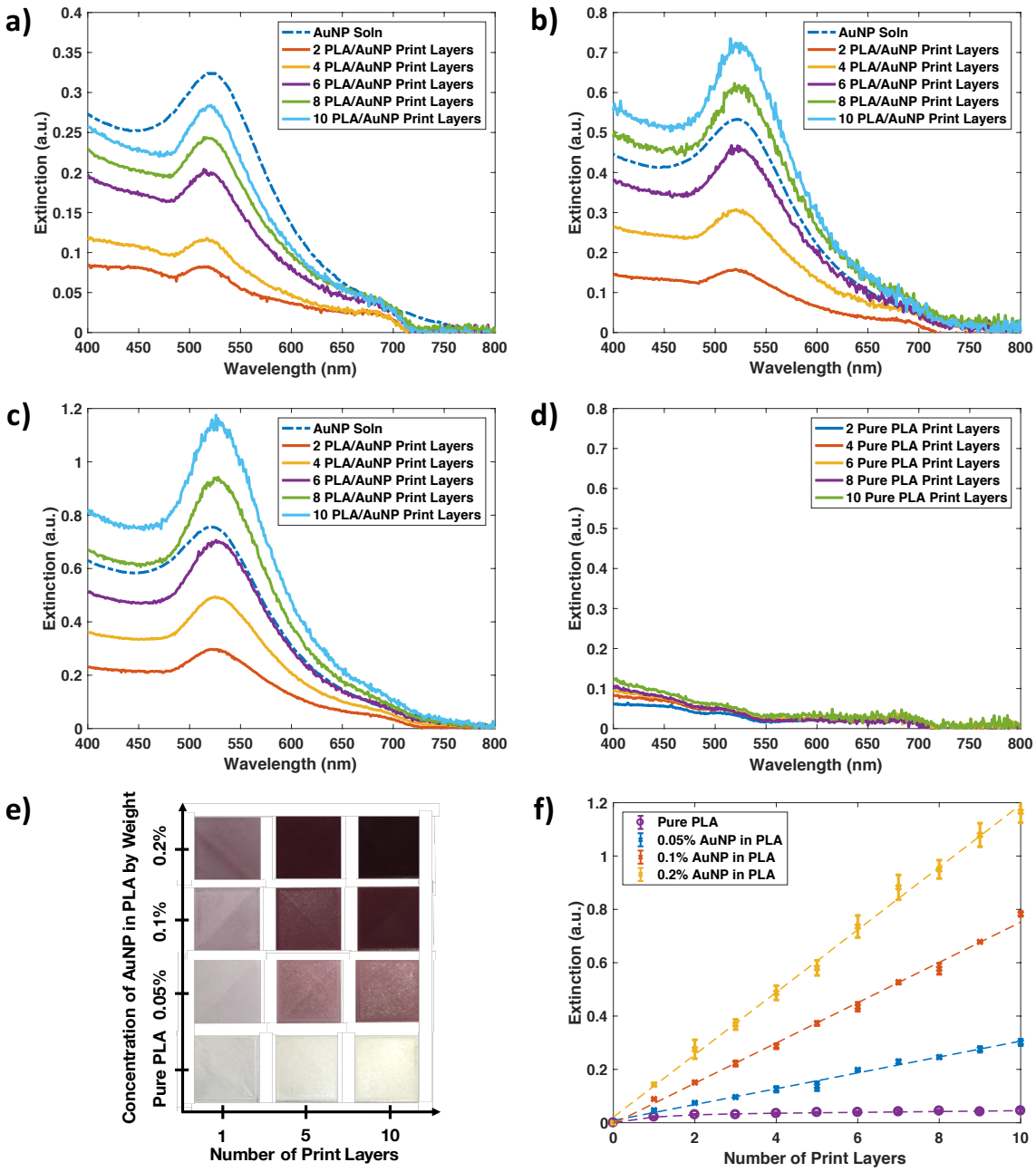

Figure 4.4 a) Absorbance spectrum of AuNP suspended in toluene (with a SPR peak at 521nm) and 3D printed PLA/AuNP films (0.05% AuNP in PLA by weight) with increasing number of print layers from 2 – 10 total layers (i.e. 0.2 mm – 1.0 mm). b) Absorbance spectrum of 3D printed PLA/AuNP films (0.1% AuNP in PLA by weight) with increasing number of print layers. c) Absorbance spectrum of 3D printed PLA/AuNP films (0.2% AuNP in PLA by weight) with increasing number of print layers. d) Absorbance spectrum of pure PLA films with increasing number of print layers. e) 3D-printed films of pure PLA and PLA/AuNP at concentrations of 0.05%, 0.1% and 0.2% AuNP in PLA by weight. f) Absorbance measured at SPR peak vs. number of print layers for 3D printed films of pure PLA and PLA/AuNP at concentrations of 0.05%, 0.1% and 0.2% AuNP in PLA by weight.

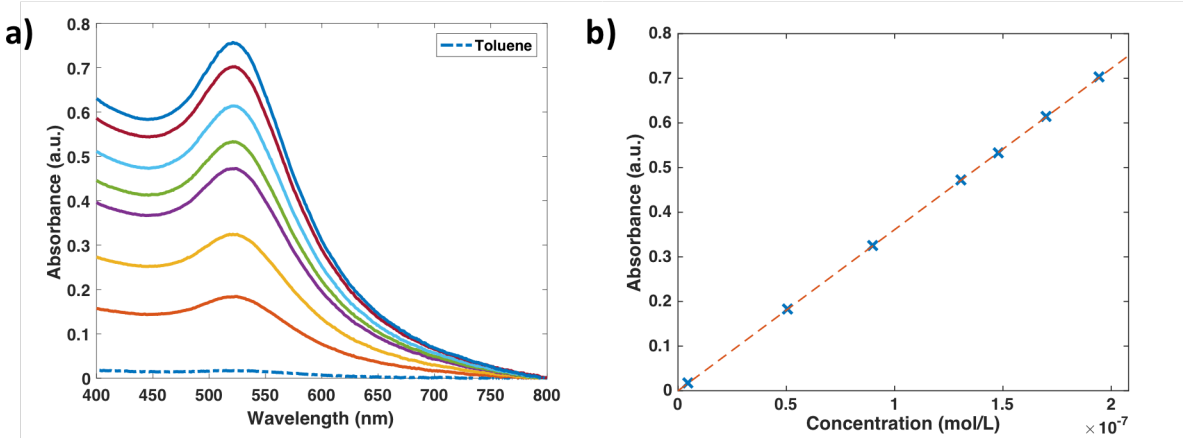

Figure 4.5 (a) Absorbance spectrum for AuNPs suspended in toluene at various concentrations. b) Concentration of nanoparticles in solution vs. absorbance measured at SPR peak (521 nm) demonstrating Beers Law for AuNPs in solution.

The absorbance of 3D-printed PLA/AuNP films was found to be directly dependent on overall material thickness and total number of print layers (Figures 4.4a – 4.4c). These results are again consistent with Beer-Lambert's Law for nanoparticles in solution discussed in Chapter 3, where a linear relationship between absorbance measured at the SPR peak and concentration of AuNPs in solution is obtained (Equation 3.1 and Figure 4.5). Similarly, a linear relationship between the total number of print layers and absorbance (measured at the SPR peak for AuNPs in solution, 521 nm) is obtained for 3D-printed PLA/AuNP thin films at varying concentrations of AuNP in PLA by weight (Figure 4.4f, Table 4.1). In this case, the molar extinction coefficient and concentration of AuNPs in PLA remain constant, while the measured path length changes with increasing number of print layers and overall material thickness. Through the inclusion of AuNPs within 3D-printed structures, I am able to correlate the total number of PLA/AuNP print layers and absorbance in accordance with trends predicted by Beer-Lambert's Law.

Table 4.1 Equations used to fit data and corresponding R-square values for varying concentrations of AuNP in PLA/AuNP solid films (y = absorbance/extinction, x = number of print layers).

Concentration AuNP in PLA by Weight	Equation Used to Fit Data	R-squared Value
0% (Pure PLA)	y = 0.03103*exp(0.03787*x) - 0.03086*exp(-1.042*x)	0.9854
0.05%	y = 0.02974*x + 0.008598	0.9965
0.1%	y = 0.07552*x - 0.002997	0.9908
0.2%	y = 0.1171*x + 0.02097	0.9972

Utilizing this relationship, I present an alternative methodology in which the presence of defects and missing print layers in 3D-printed parts can be detected, localized and quantified through the inclusion of nanoparticles within the 3D printing process. To test this hypothesis, the absorbance of both PLA/AuNP and pure PLA control samples containing voids of 0.2 mm, 0.3 mm and 0.4 mm, representing two, three and four missing print layers, respectively, were studied (Figures 4.6b – 4.6d). To ensure uniform and repeatable void configurations between individual test samples, an internal support structure was printed using a polyvinyl alcohol (PVA) support. PVA was selected as the support polymer due to its minimal absorbance in the visible range,[131] representative of defects and missing print layers that may arise in the 3D printing process (Figure 4.7).

Representative absorbance spectra for a PLA/AuNP film (0.1% AuNP in PLA by weight) measured at locations with no missing print layers, and two, three and four missing print layers, indicates the feasibility of the proposed approach for nondestructive defect detection and localization (Figure 4.8a). When absorbance measured at the SPR peak is plotted for regions with and without voids, the presence of missing print layers is easily identified and quantified as a result of the inclusion of AuNPs (Figure 4.8b). For regions with no voids or

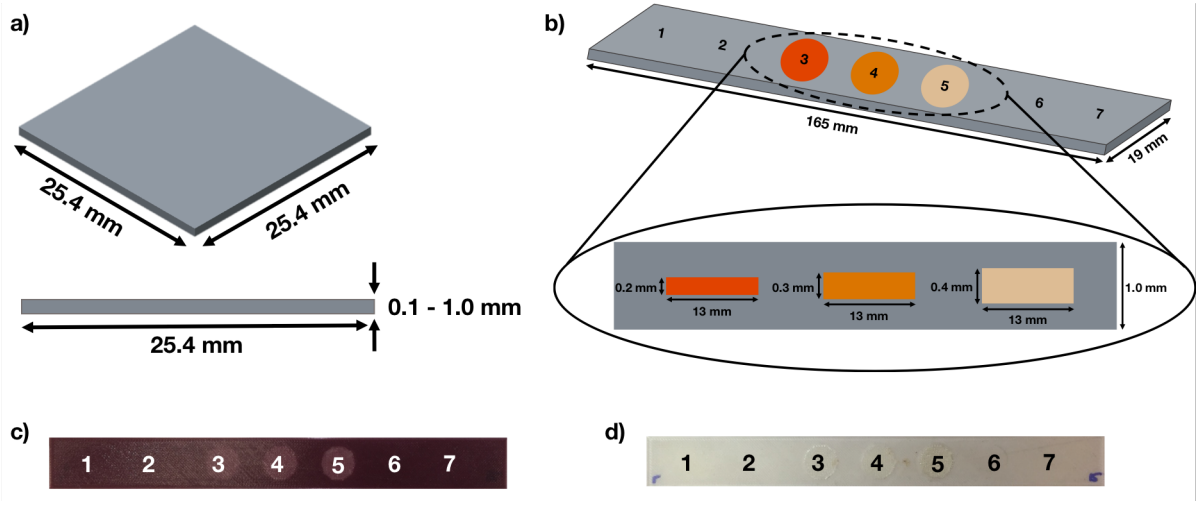

Figure 4.6 a) Schematic representation and dimensions of 3D printed solid thin film samples. b) Schematic representation and dimensions of void space samples, in which the numbers represent locations where absorbance measurements are recorded. A total of nine scans, recorded from three individual test samples, were statistically analyzed to obtain the average absorbance and error bars herein presented. c) Representative 3D-printed PLA/AuNP void spacing sample. d) Representative 3D-printed pure PLA void spacing sample.

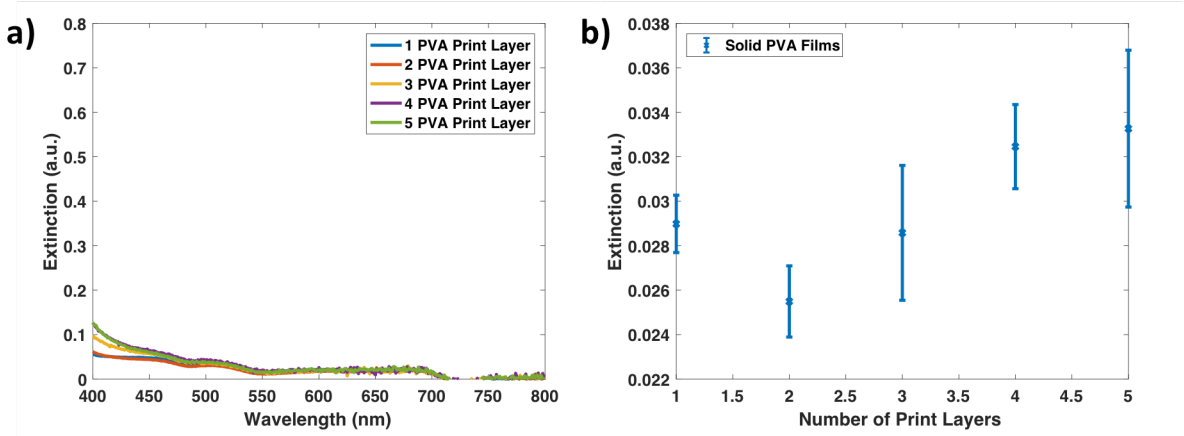

Figure 4.7 a) Absorbance spectra of solid polyvinyl alcohol (PVA) films with increasing number of print layers. b) Absorbance of PVA measured at SPR peak for AuNPs in solution (521 nm), where no trend or statistical difference is observed for films of increasing thickness.

missing print layers, absorbance remains nearly constant, but with the introduction of defects into the material, absorbance begins to linearly decrease in accordance with the total number of missing print layers and corresponding decrease in overall PLA/AuNP thickness (Figure 4.8c and Table 4.2).

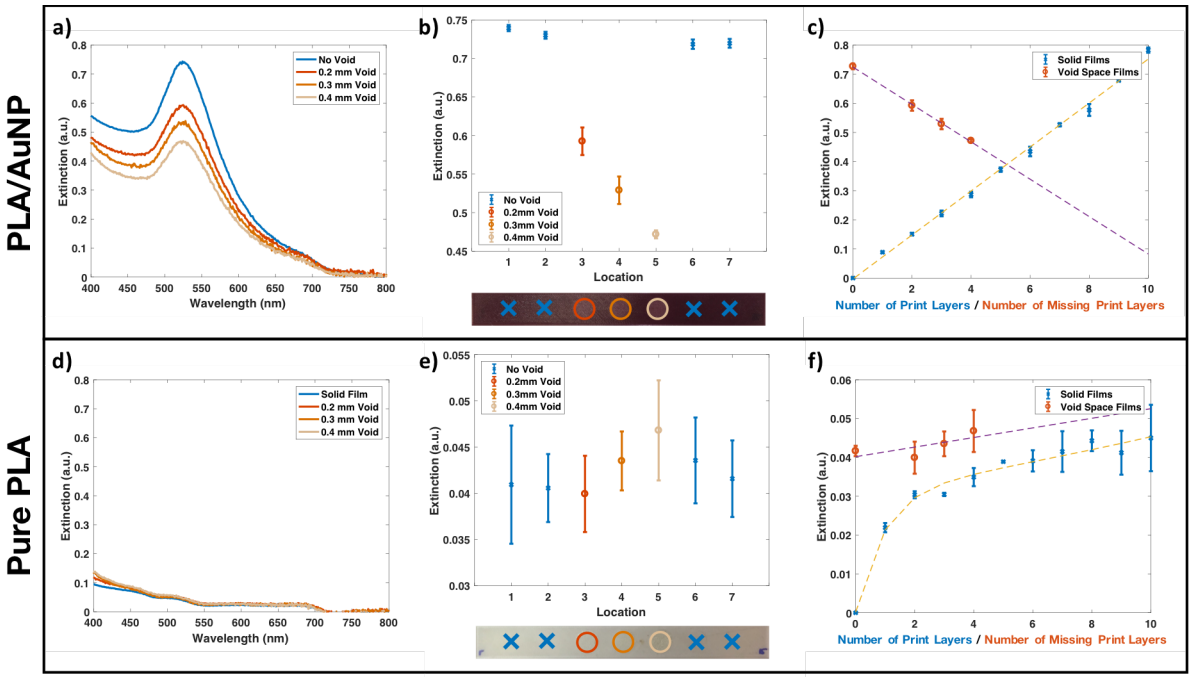

Figure 4.8 a) Absorbance spectrum of PLA/AuNP test specimen recorded at locations with no void, and 0.2 mm, 0.3 mm and 0.4 mm voids, respectively. b) Absorbance of PLA/AuNP test specimens measured at 521 nm at regions with no voids, and 0.2 mm, 0.3 mm and 0.4 mm voids, from left to right. c) Comparison between trends for absorbance vs. number of print layers and absorbance vs. number of missing print layers for PLA/AuNP samples. d) Absorbance spectrum of pure PLA test specimen recorded at locations with no void, and 0.2 mm, 0.3 mm and 0.4 mm voids, respectively. e) Absorbance of pure PLA test specimens measured at 521 nm at regions with no voids, and 0.2 mm, 0.3 mm and 0.4 mm voids, from left to right. f) Comparison between trends for absorbance vs. number of print layers and absorbance vs. number of missing print layers for pure PLA samples.

As absorbance was found to be directly related to the total number of print layers and overall material thickness for AuNP-functionalized specimens, I expect to observe similar absorbance for both solid and void space samples with the same total number of PLA/AuNP print layers. Using values obtained from their respective fitted linear trends (Figure 4.8c and Table 4.2), absorbance measured at the SPR peak for samples with the same total number of PLA/AuNP print layers is shown in Table 4.3. Comparing the recorded absorbance, the optical response of PLA/AuNP void spacing samples was found to overwhelmingly agree with solid

Table 4.2 Equations used to fit data and corresponding R-square values for pure PLA and PLA/AuNP void space samples shown in Figure 4.8, where y = absorbance and x = number of print layers.

Concentration AuNP in PLA by Weight	**Equation Used to Fit Data**	**R-squared Value**
0% (Pure PLA)	y = 0.001236*x + 0.04019	0.5159
0.1%	y = -0.06416*x + 0.7244	0.9988

Table 4.3 Comparison between absorbance response for solid PLA/AuNP films and PLA/AuNP void spacing samples shown in Figure 4.8 (0.1% AuNP in PLA by weight).

Solid Films		**Void Spacing**		**% Difference**
Number of Print Layers	*Absorbance (a.u.)*	*Number of Missing Print Layers out of 10 Total Print Layers*	*Absorbance (a.u.)*	
10	0.75	0 (No Void)	0.73	3.8
8	0.60	2 (0.2 mm Void)	0.59	0.85
7	0.53	3 (0.3 mm Void)	0.53	1.2
6	0.45	4 (0.4 mm Void)	0.47	3.8

PLA/AuNP films. Due to the incorporation of AuNPs within the PLA host matrix, and trends predicted by Beer-Lambert's Law, as few as two missing print layers (0.2 mm void) were localized and quantified within a 0.85% difference relative to solid PLA/AuNP films of the same total number of print layers.

Unlike PLA/AuNP samples though, the presence of defects and missing print layers in unmodified pure PLA control samples were unable to be identified or quantified using absorbance measurements, as pure PLA was observed to have minimal absorbance across the visible spectrum (Figure 4.8d). Absorbance intensity measured at the SPR peak for all seven locations tested displayed no distinct trend in accordance with the total number of pure PLA print layers printed (Figure 4.8e). In fact, there was no statistical difference between the

recorded absorbance for regions with no missing print layers and those containing voids, regardless of their size or location. The inability to detect missing print layers and material defects is further confirmed when absorbance trends for unmodified pure PLA solid and void control samples with the same total number of overall print layers are compared, as no overlap between the two curves is obtained (Figure 4.8f).

Additional void spacing configurations were evaluated for PLA/AuNP and unmodified pure PLA control samples. Here, 0.2 mm, 0.3 mm and 0.2 mm defects (two, three and two missing print layers) were printed using a PVA support. Again, the presence, location and relative size of material defects are identified through absorbance measurements for PLA/AuNP samples due to the optical properties of embedded AuNPs, while unmodified pure PLA films do not display any statistical difference in absorbance for regions with and without material defects (Figures 4.9a and 4.9b, respectively). A comparison between the optical response for PLA/AuNP and pure PLA films measured at the SPR peak plotted on the same

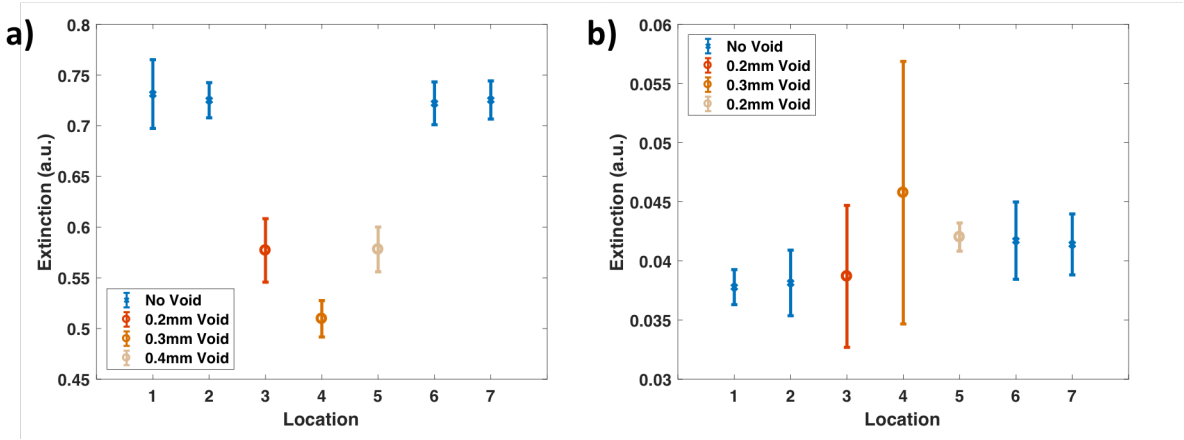

Figure 4.9 a) Absorbance of PLA/AuNP test specimens with three void locations of 0.2 mm, 0.3 mm and 0.2 mm from left to right. Using absorbance measurements, demonstrated ability to localize and identify the presence and relative size of the void defect for PLA/AuNP printed films. b) Absorbance of pure PLA test specimens with three void locations of 0.2 mm, 0.3 mm and 0.4 mm from left to right. Using absorbance measurements, unable to localize and identify the presence and relative size of the void defect in the unmodified pure PLA host matrix.

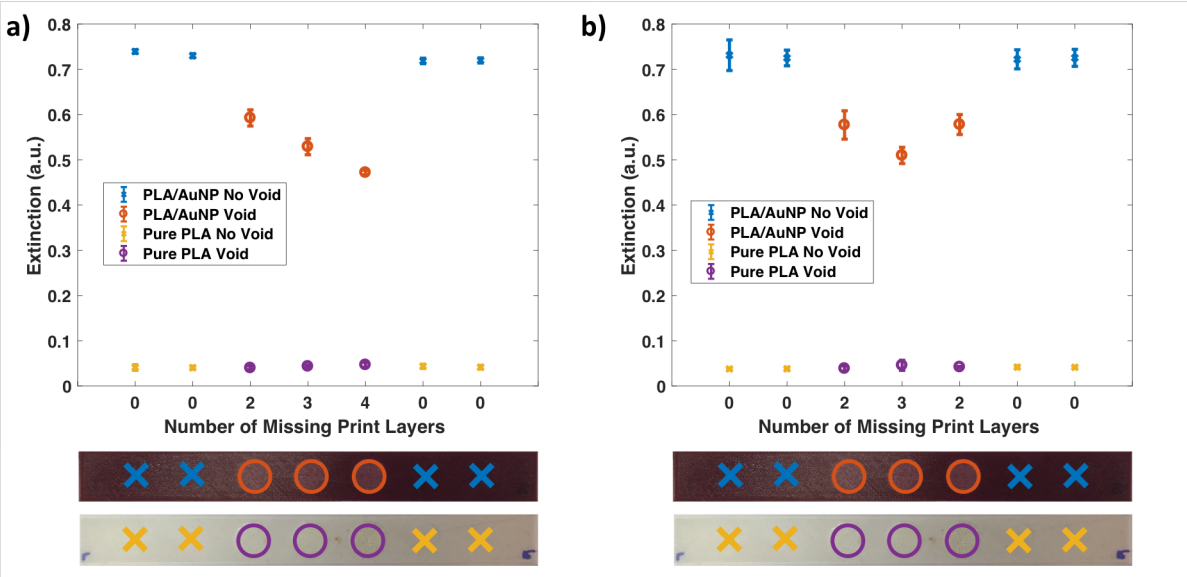

Figure 4.10 a) Comparison of absorbance measured at SPR peak location for PLA/AuNP and pure PLA at regions with no material defects, and two, three and four missing print layers, from left to right. b) Comparison of absorbance measured at SPR peak for PLA/AuNP and pure PLA at regions with no material defect, and two, three and two missing print layers, from left to right.

scale for both void configurations further confirms the effectiveness of embedded AuNPs for nondestructive defect detection as compared to an unmodified pure PLA host matrix (Figure 4.10).

The temporal response of 3D-printed PLA/AuNP films was also studied to evaluate the optical stability of the embedded AuNPs. After one year (365 days), as-printed PLA/AuNP films did not display any signs of degradation, as no change in the overall behavior or shape of the absorbance spectrum was observed (Figure 4.11a). Regardless of film thickness tested, absorbance at the SPR peak remained constant for 3D-printed PLA/AuNP films throughout the one-year period (Figure 4.11b). The stability of AuNPs embedded within the PLA matrix is crucial for ensuring the longevity of the proposed passive sensing methodology for continued monitoring of defects in as-printed parts, as a single baseline measurement can be used as a reference throughout the useable lifetime of 3D-printed materials.

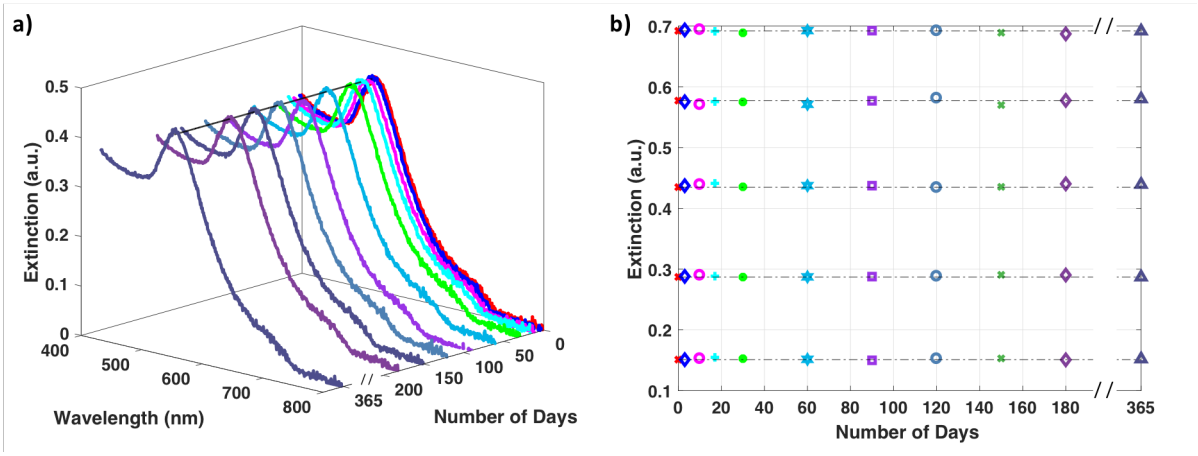

Figure 4.11 a) Representative absorbance spectrum for a 0.6 mm PLA/AuNP 3D printed film (0.1% AuNP in PLA by weight) over a period of one year (365 days). b) Absorbance measured at SPR peak (521 nm) for 3D-printed PLA/AuNP films at varying thicknesses over a period of one year (365 days), where absorbance remains constant for all film thicknesses tested. Data point colors correspond to date upon which absorbance measurements were recorded. Black lines represent absorbance measured at the SPR peak for the first recorded absorbance measurement.

4.4 Conclusions

Again relying on materials design and process considerations, this Chapter focused on the incorporation of gold nanoparticles for 3D printing processes to demonstrate the capability of designing a sensing methodology through the use of material additives. Utilizing the absorbance of embedded gold nanoparticles, the presence of defects and missing print layers in 3D-printed parts are localized and quantified through a nondestructive approach. Using this methodology, as few as two missing print layers (0.2 mm defect) are identified within a 0.85% difference when compared to solid PLA/AuNP films with the same total number of print layers. For an unmodified pure PLA host matrix, though, the presence and location of material defects are unable to be distinguished according to absorbance measurements alone, as pure PLA has minimal absorbance across the visible spectrum regardless of the total number of print layers and overall material thickness tested. The optical sensing enabled through materials processing

considerations and the inclusion of AuNPs in the PLA host matrix was highly stable, as the temporal response and optical behavior of 3D-printed PLA/AuNP films showed no signs of change or degradation one year after printing. Moving towards future applications, additional work will focus on expanding the range of material thickness compatible with this nondestructive inspection through a number of material and process design considerations. By selecting a polymer host matrix with minimal absorbance across the visible spectrum, and minimizing the overall concentration of selected material additive, it should be feasible to inspect 3D-printed parts and structures for material defects and damage with larger material thicknesses than the ones discussed in this Chapter.

Chapter 5

3D-Printed Electroluminescent Devices

5.1 Introduction

Combining the insights obtained in Chapters 3 and 4, the design and development of a stimuli responsive 3D-printed alternating current electroluminescent (ACEL) device is presented in this Chapter based on the optical response of ZnS:Cu phosphors. In their most basic configuration, ACEL devices are comprised of a phosphor/dielectric composite binder and a set of conductive electrodes through which external electrical stimuli can be applied to the device. The subsequent voltage drop across the phosphor/dielectric layer under electrical excitation results in an intense, bright luminescence based on the specific type of embedded phosphor and the applied voltage. Such devices have been used for a range of applications related to lighting and displays, and are continuing to gain attention for additional uses, such as sensing,[132] due to the flexibility of their design and implementation.

Traditionally ACEL devices are fabricated in multi-step processes involving various spin coating, masking, drop casting and curing iterations to manufacture the final device. Polymer host matrices such as polydimethylsiloxane (PDMS),[70–73,133,134] and other thermoplastics,[74] resins[61,132,135] and epoxies[136–138] have all been reported as encapsulating agents for the development of both the phosphor/dielectric composite and conducting electrodes. Although such conventional manufacturing approaches have resulted in the demonstration of a number of functional and durable ACEL devices, these fabrication techniques are time-consuming, posing a challenge to the more widespread use and implementation of ACEL devices.

In order to address such constraints, the first known demonstration of a 3D-printed ACEL device using a commercially available fused deposition modeling (FDM) type 3D printing system is reported in the paper submission upon which this Chapter is based.[139] As opposed to conventional manufacturing techniques that often require one or more hours of fabrication time,[70,73] functional and customizable ACEL devices can be printed in a matter of minutes using the approach discussed in this Chapter. Building upon recent reports in which phosphors have been utilized for direct ink writing (DIW) processes,[140] these 3D-printed devices consists of a polylactic acid (PLA)-based phosphor/dielectric composite binder sandwiched between an indium tin oxide (ITO) glass substrate and a 3D-printed carbon-based conductive PLA electrode to achieve device illumination and luminescence. 3D-printed PLA/phosphor ACEL devices were tested under various electrical configurations, and their resulting optical responses were recorded. By embedding copper-doped ZnS phosphors (ZnS:Cu, with an approximate particle size of 24 ± 6 μm, Figure A3.1) within the PLA host matrix, a visual color change from green to blue was observed with increasing excitation frequencies, where the overall luminescent intensity was found to be dependent on the applied voltage.

5.2 Experimental Methods

Details relating to experimental methods and materials, including functionalized PLA/phosphor filament fabrication, are provided in Chapter 2. Phosphors were embedded in PLA at concentrations, up to 40% by weight, to evaluate the optical response of PLA/phosphor samples, as well as the effectiveness of the proposed approach for the design and development for 3D-printed ACEL devices.

5.3 Results and Discussion

For initial testing, thin film templates, 0.5 mm in thickness, with varying concentrations of embedded phosphors ranging from 5 – 40% by weight, were fabricated to evaluate the optical response of the PLA/phosphor composite after materials processing and printing. 3D-printed PLA/phosphor thin film templates displayed a bright blue-green luminescent coloration under UV excitation (Figure 5.1a). Consistent with other polymer/ZnS:Cu-based phosphor systems,[70] the 3D-printed films exhibited a single monotonic photoluminescence (PL) emissive peak centered near 515 nm (Figure 5.1b). Though the overall spectral shape remained constant between the various concentrations tested (Figure 5.1d), the PL response reached a maximum intensity at a 20% by weight loading of phosphors embedded in PLA (Figure 5.1c). This behavior is attributed to the reduced efficiency of phosphors in close proximity and a partial wetting of their surface. Though there are more phosphors and subsequent potential light emitting sites, the increased density of the surrounding particles at higher concentrations effectively reduces the proportion of available light emitting sites, leading to a reduction in emissive efficiency and PL.[66] Further inspection of the 3D-printed films using differential interference contrast (DIC) microscopy confirms this behavior, where phosphors were observed to exist in close contact with one another, occasionally forming partially aggregated structures in samples containing higher concentrations of embedded phosphors (Figure 5.2). At a 20% by weight loading, though, phosphors were well dispersed throughout the 3D-printed films, providing a number of light-emitting sites that were observed under WL microscopy (Figure 5.3). Based on these findings and observations, all PLA/phosphor samples and ACEL devices were fabricated at a 20% by weight loading of phosphors to maximize the overall luminescent and optical response of the 3D-printed devices and structures.

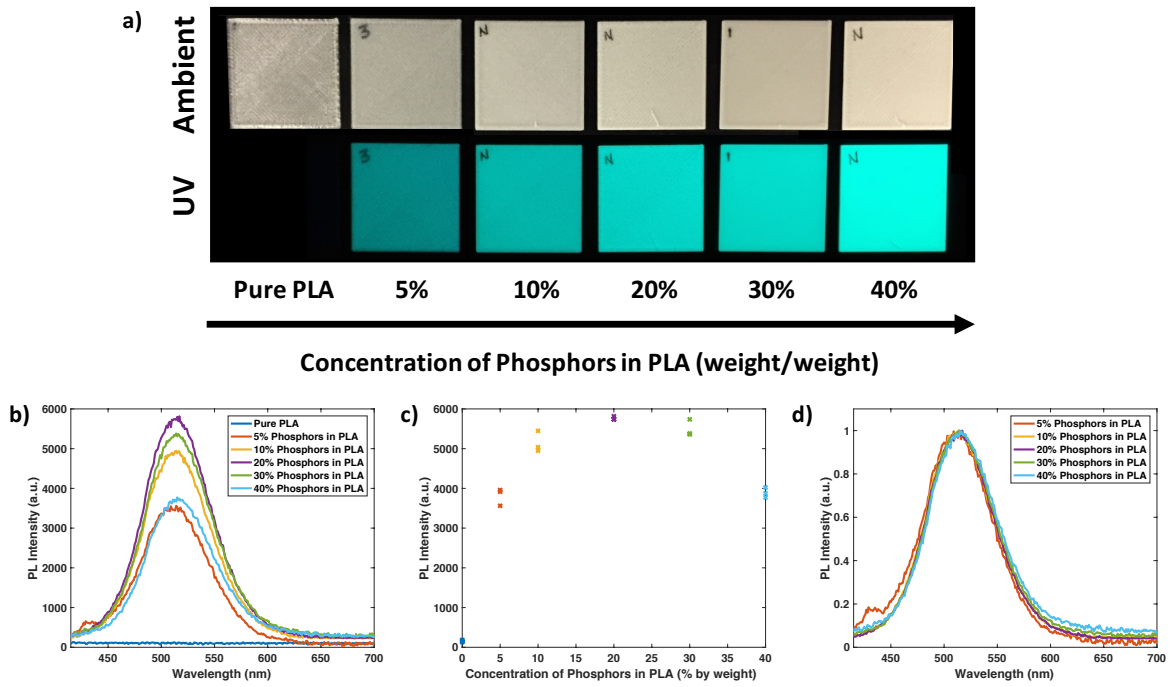

Figure 5.1 a) 3D-printed PLA/phosphor thin film samples at varying concentrations of phosphors in PLA (% by weight) under ambient and UV excitation (top and bottom, respectively). b) Photoluminescence (PL) response of 3D-printed PLA/phosphor thin film samples recorded at varying concentrations of phosphors in PLA (% by weight). c) Maximum PL intensity for 3D-printed PLA/phosphor thin film samples at varying concentrations of phosphors in PLA (% by weight) where three individual scans for each weight percent are shown in the plot. d) Normalized PL spectral response for 3D-printed PLA/phosphor thin film samples at various concentrations of phosphors in PLA by weight.

At 20% by weight, the 3D-printed samples studied in this report were fabricated using a significantly lower concentration of embedded phosphors compared to other ZnS-based devices previously reported in the literature, in which phosphor loadings in excess of 50% by weight are commonly used to obtain the desired optical response and behavior for both electro- and mechano-luminescent applications.[70–73,140] The ability to reduce the overall concentration and required weight of embedded phosphors provides a distinct advantage not only in cost but also in reducing the impact that functionalization has on the underlying material response and behavior of the polymer host matrix. Prior studies, including the results detailed in Chapter 3,

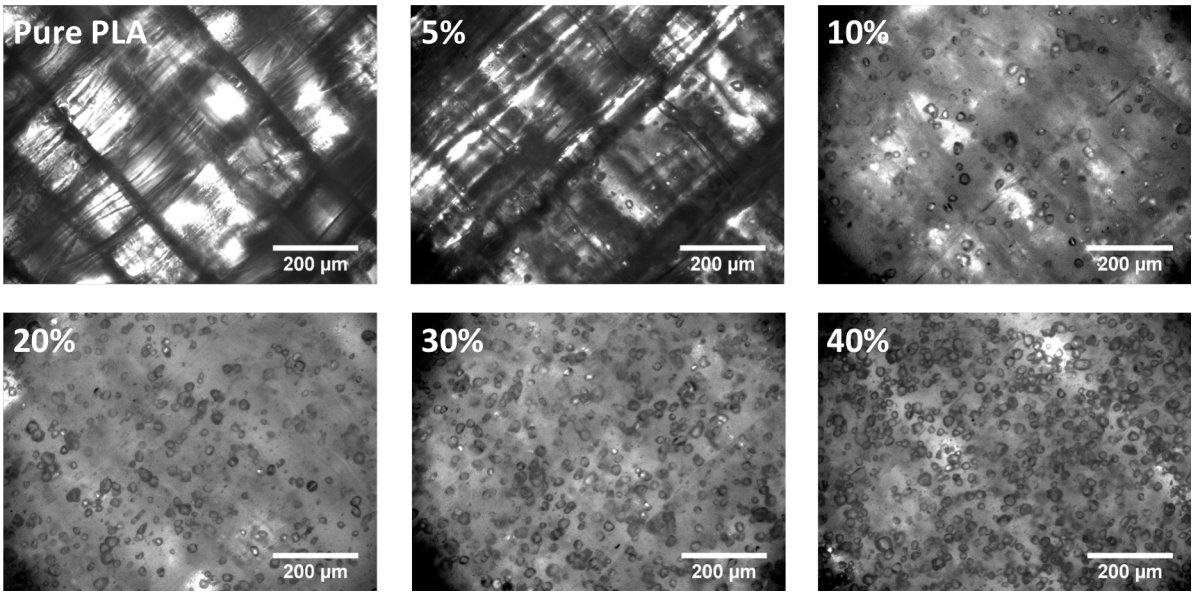

Figure 5.2 DIC microscopy of 3d-printed PLA/phosphor thin film samples at various concentrations of phosphors in PLA by weight. With increasing concentration, phosphors are observed to exist in close proximity, often in contact with one another at higher concentrations of embedded phosphors. The diagonal lines are a result of the sample fabrication process and nozzle movement/filament deposition during the 3D printing process.

have shown that functionalization can impact a number of material properties ranging from mechanical strength and durability, to thermal stability.[88,141–143] By effectively reducing the overall concentration of embedded phosphors needed for device fabrication, I aim to minimize any adverse impacts that functionalization may have on the material properties and response of the PLA host matrix as was demonstrated in Chapter 3, while still maintaining the optical response necessary to develop functioning ACEL devices.

A schematic representation of the 3D-printed ACEL devices tested in this paper is shown in Figure 5.4a. A single layer of PLA/phosphor material (100 μm in thickness) was directly deposited onto a pre-cleaned conductive ITO glass substrate and sandwiched between two layers of 3D-printed conductive carbon-based PLA serving as a second electrode (200 μm in thickness). In total, ACEL devices and samples were manufactured in less than 5 minutes,

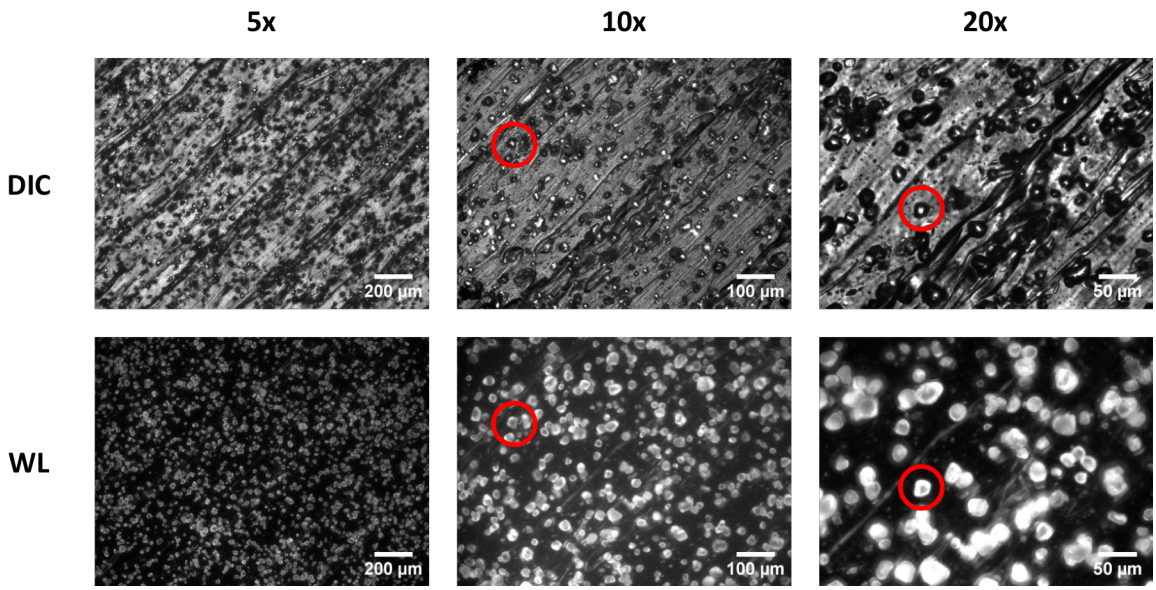

Figure 5.3 Differential interference contrast (DIC) and white light (WL) microscopy images for 3D-printed PLA/phosphor thin film (20% phosphor in PLA by weight) at increasing levels of magnification. Red circles indicate representative ZnS:Cu phosphor particles embedded in PLA under DIC and WL excitation, respectively. The diagonal lines visible in the images are a result of material deposition and nozzle movement occurring during the 3D printing process and material deposition/sample fabrication.

including the time required for nozzle heating and the entire 3D printing process. The optical response of 3D-printed ACEL devices was then evaluated for various conditions of frequency- and voltage-dependent excitations using a CCD-based spectrometer system. For each case, a sinusoidal voltage was applied across the single PLA/phosphor layer using a function generator and associated amplification source where samples were tested for voltages ranging from 150 V to 245 V and corresponding frequencies spanning from 10 Hz to 10 kHz.

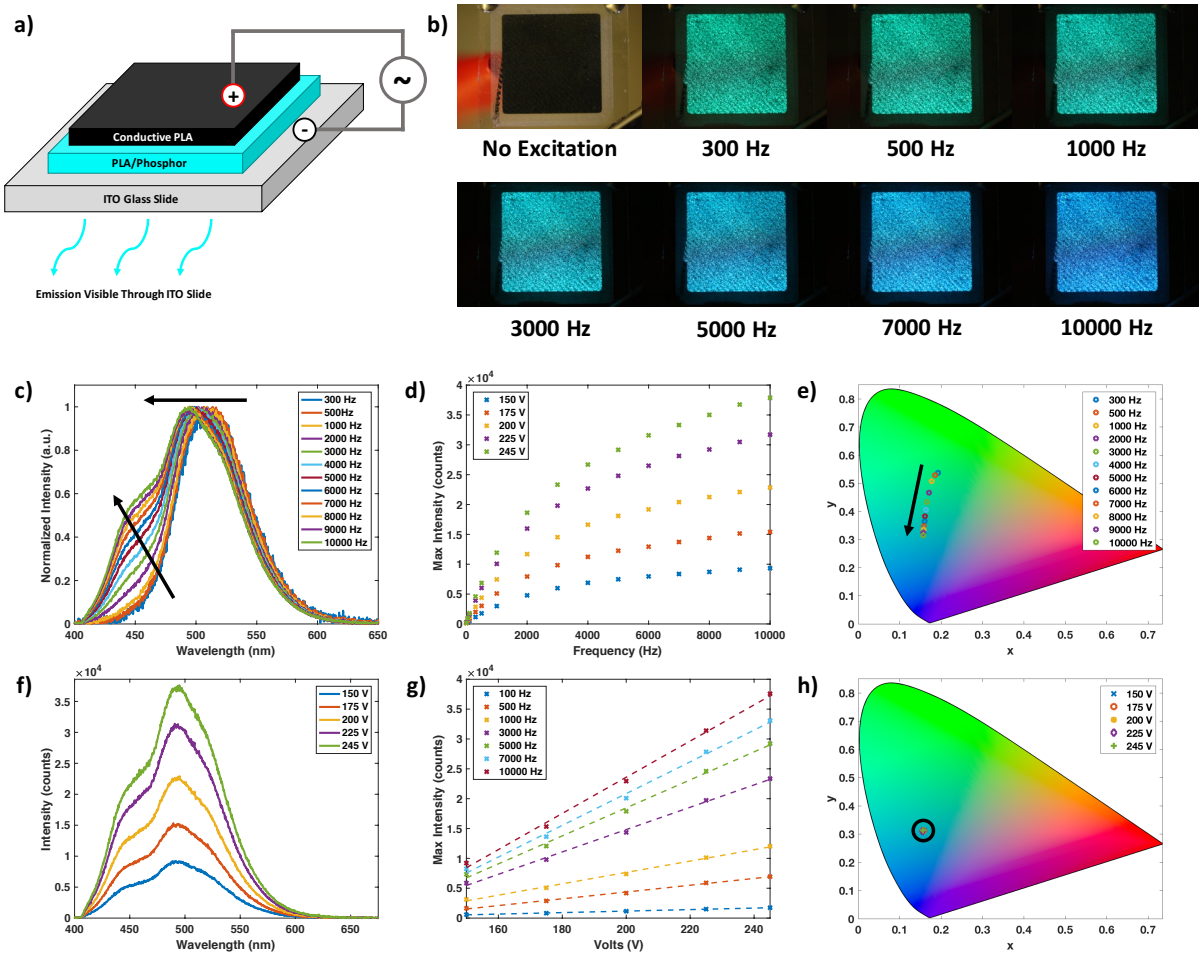

Figure 5.4 a) Schematic representation of 3D-printed ACEL device (from bottom to top: ITO glass slide/3D-printed PLA/phosphor layer/3D-printed conductive PLA electrode, where emission is visible through the bottom of the ITO glass slide). b) Still images of 3D-printed ACEL devices at various excitation frequencies under constant applied voltage (245 V). c) Normalized electroluminescence (EL) intensity spectra of representative ACEL device at increasing frequencies under 245 V excitation source (arrows are included as a guide for the eye for increasing frequencies studied). d) Dependence of excitation frequency on maximum EL response at various voltages; e) CIE coordinate (x,y) values for PL response at increasing frequencies under 245 V excitation source (arrow is included as a guide for the eye for increasing frequencies studied). f) Representative EL intensity spectra for ACEL device at increasing voltages with a constant 10 kHz excitation source. g) Dependence of excitation voltage on maximum EL response at various frequencies (dashed lines represent linear fits for each frequency studied; additional curve fitting information can be found in the supporting information Table C1). h) CIE coordinate (x,y) values at various voltages for constant 10 kHz excitation source (location of data points for all voltages tested fall within the black circle shown in the figure).

Still images of a representative 3D-printed ACEL device exposed to a constant voltage source and various excitation frequencies are shown in Figure 5.4b. Under these conditions, the 3D-printed samples displayed a bright luminescence that gradually changed color from green to blue with increasing excitation frequencies. The resulting electroluminescent (EL) spectral response was recorded in order to further quantify the impact of voltage and frequency on the optical response and resultant color change for 3D-printed ACEL devices. As the excitation frequency was increased from 300 Hz to 10 kHz under a constant voltage, the maximum EL peak location shifted from 517 nm to 495 nm and a secondary peak emerged near 450 nm for frequencies above 2000 Hz (Figure 5.4c). Furthermore, the maximum EL intensity and corresponding brightness of the 3D-printed ACEL devices dramatically increased with increasing frequency (Figures 5.4d). Commission Internationale de L'Eclairage (CIE) coordinates were used to visualize the dependence of color and electroluminescence on the applied voltage and excitation frequency by providing a relationship between the recorded spectral response and the corresponding color perceived by the human eye (Figure 5.4d). For the representative device shown, the calculated CIE coordinates shifted from (0.19, 0.54) to (0.16, 0.31) when frequency was increased from 300 Hz to 10 kHz, corresponding to the green to blue color change that was visually observed (Figure 5.4b and Table 5.1). The spectral response and corresponding shifts in both the observed color and in CIE coordinates were consistent among all samples tested, regardless of the applied voltage as shown in Figures 5.5 and 5.6, where additional information can be found in Supporting Information (Figures C1 – C5, and Table C1).

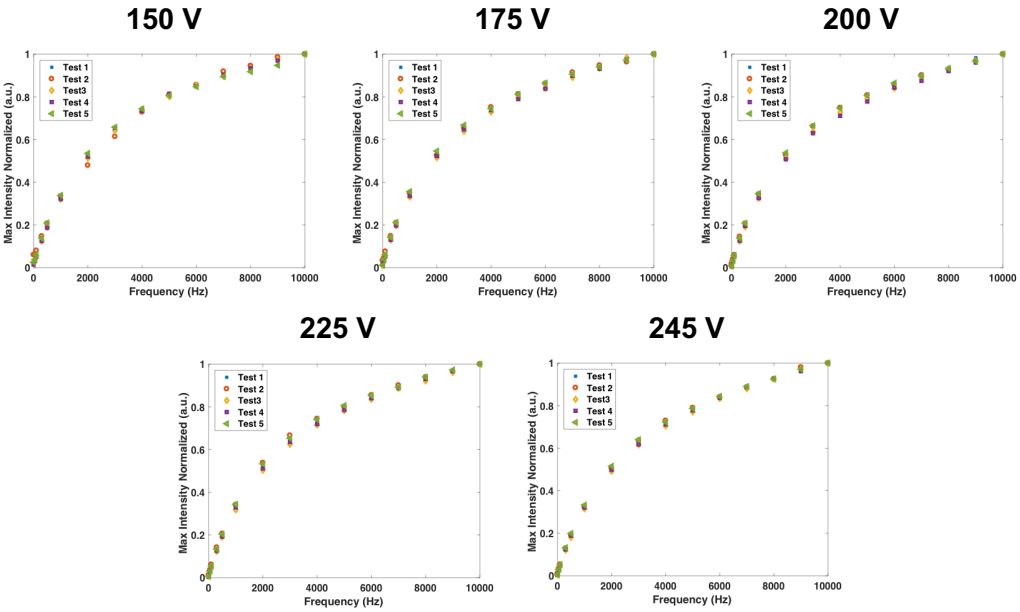

Figure 5.5 Normalized frequency-dependent maximum EL response at various applied voltages for five individual test samples studied.

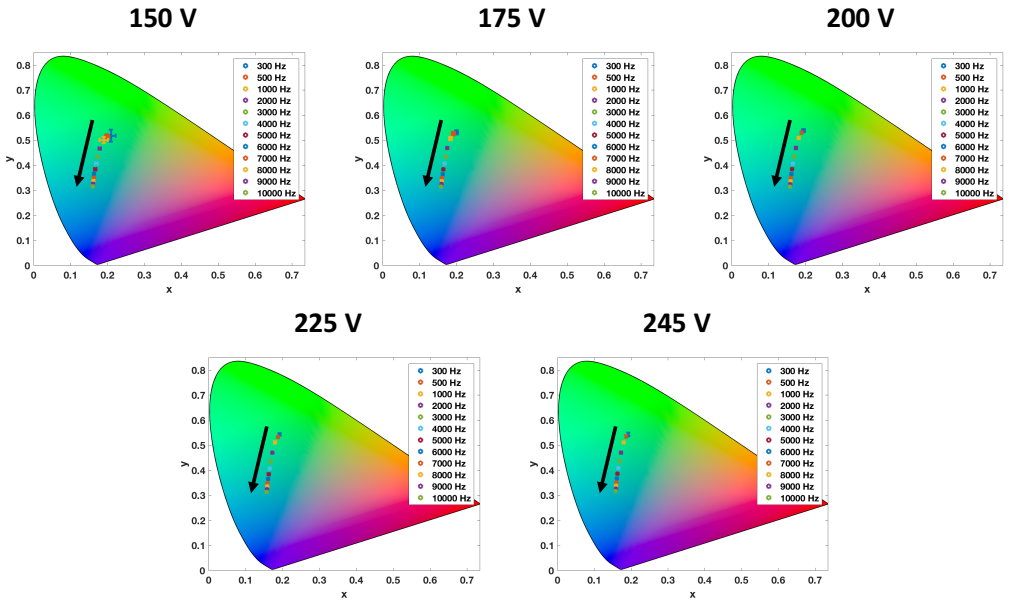

Figure 5.6 CIE spectra for frequency-dependent response at various excitation voltages. CIE response plotted for each figure represents averages of all five samples tested. CIE coordinate (x,y) pairs and corresponding standard deviations for the average values displayed are included in Table C2.

Table 5.1 Frequency-dependent response of CIE coordinates (x,y) at various applied voltages. CIE coordinates (x,y) correspond to data shown in Figure C3.

	150 V		175 V		200 V		225 V		245 V	
Frequency (Hz)	**x**	**y**	**x**	**y**	**x**	**y**	**x**	**y**	**x**	**y**
50	0.27	0.44	0.23	0.50	0.24	0.52	0.22	0.54	0.21	0.55
100	0.24	0.51	0.22	0.53	0.21	0.53	0.21	0.53	0.21	0.55
300	0.20	0.53	0.20	0.53	0.19	0.54	0.19	0.54	0.19	0.54
500	0.19	0.52	0.19	0.53	0.19	0.53	0.19	0.53	0.19	0.53
1000	0.18	0.50	0.18	0.50	0.18	0.51	0.18	0.51	0.18	0.51
2000	0.18	0.46	0.17	0.47	0.17	0.46	0.17	0.47	0.17	0.47
3000	0.17	0.43	0.17	0.43	0.17	0.43	0.17	0.43	0.17	0.43
4000	0.17	0.40	0.17	0.40	0.17	0.40	0.16	0.40	0.16	0.41
5000	0.16	0.38	0.16	0.38	0.16	0.38	0.16	0.38	0.16	0.38
6000	0.16	0.36	0.16	0.36	0.16	0.36	0.16	0.36	0.16	0.36
7000	0.16	0.35	0.16	0.35	0.16	0.35	0.16	0.35	0.16	0.35
8000	0.16	0.33	0.16	0.33	0.16	0.33	0.16	0.33	0.16	0.34
9000	0.16	0.32	0.16	0.32	0.16	0.32	0.16	0.32	0.16	0.32
10000	0.16	0.31	0.16	0.31	0.16	0.31	0.16	0.31	0.16	0.31

Though the presence of both green and blue emissive bands for ZnS:Cu-based phosphor systems and devices has been well documented,[71] the underlying mechanisms responsible for such spectral response and resultant change in color from green to blue with increasing excitation frequencies remain a topic of debate. In both cases, researchers hypothesize that the presence of structural impurities and metal dopant substitutions are the primary driving forces behind the optical response. For the green band occurring near 515 nm, a number of research groups attribute this emissive behavior to electron transfer between the impurity-induced shallow donor state arising from sulfur vacancies and the t_2 state of the substituted Cu ions.[71,144–147] An explanation for the subsequent blue emission and shoulder peak occurring near 450 nm, though, has yet to be agreed upon. Conflicting claims attribute

blue emission to electron transfer between the native ZnS conduction band and t_2 state of the substituted Cu ions,[144] Zn defect vacancies and resultant trap states not related to Cu dopants,[145] or transitions between sulfur vacancies and the native ZnS valence band.[148,149] With the application of an external voltage source, the recombination of electron-hole pairs between the discrete energy states ultimately leads to the observed blue/green luminescence in our 3D-printed ACEL devices.[134] The contribution of this study is not to identify the underlying mechanisms driving the emergence of additional emissive peaks with increasing frequency, but rather to demonstrate the capability of developing color tunable ACEL devices using 3D printing and additive manufacturing processes.

The optical response of 3D-printed ACEL devices was also evaluated for voltage-dependent excitation configurations. For a fixed frequency, the recorded EL spectra of a representative 3D-printed ACEL device exposed to various voltage inputs are shown in Figure 5.4f. Unlike the results for the frequency-dependent excitation case, the overall shape of the EL spectral response remained unchanged regardless of the applied voltage (Figures 5.4f). For this case, the recorded maximum EL intensity and resulting brightness increased as the applied voltage was increased. In fact, for all frequencies tested, the maximum EL intensity was linearly dependent with the applied voltage (Figure 5.4g). This response is in agreement with previously reported ACEL devices and can be attributed to an increase in excitation probability where a higher number of electrons are expected to activate more luminescent centers at higher voltages; leading to an increase in EL intensity.[150,151] As the overall EL spectral response and shape remained unchanged with increasing voltages, the recorded CIE coordinates for a fixed excitation frequency also remained relatively constant for all voltages tested (Figure 5.4h, Table 5.2). The optical response for voltage-dependent excitation was again highly

reproducible between individual samples, as seen in Figures 5.7 and 5.8 where additional spectral data can be found in Appendix C (Figures C6 – C10 and Table C3).

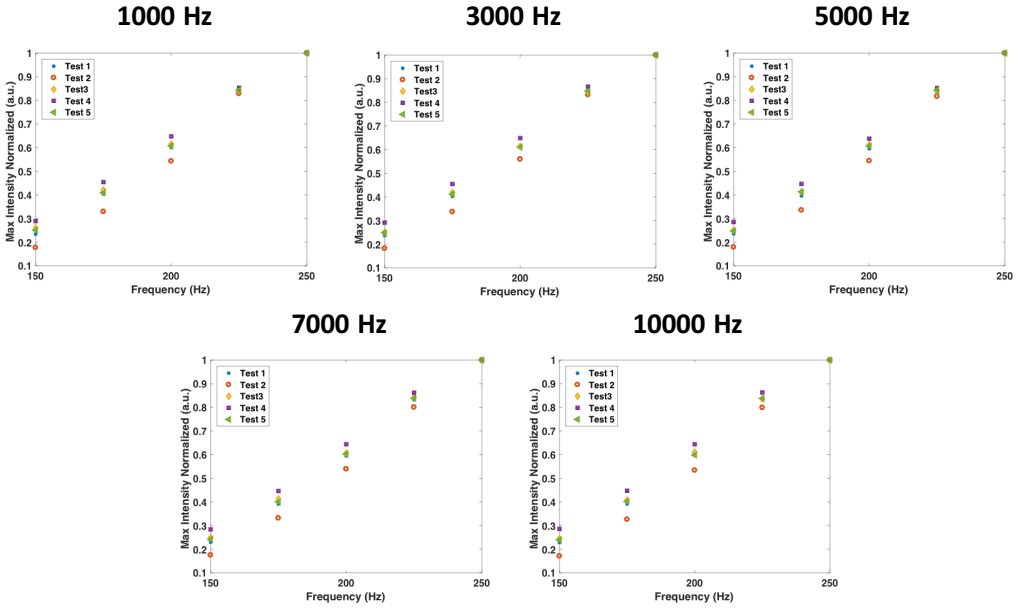

Figure 5.7 Normalized voltage-dependent maximum EL response at various applied frequencies for five individual test samples studied.

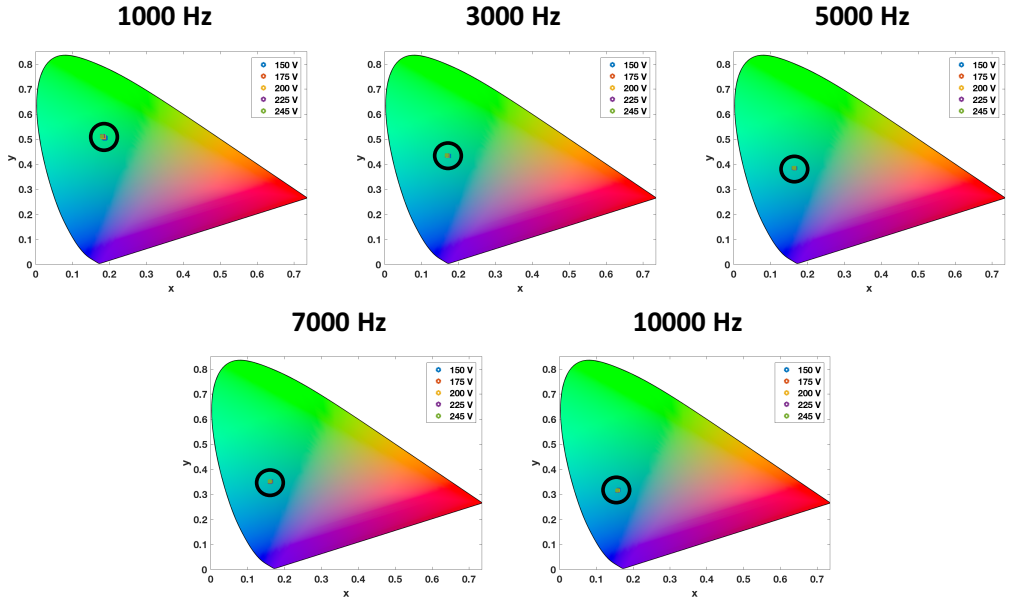

Figure 5.8 CIE spectra for voltage-dependent response at various excitation frequencies. CIE response plotted for each figure represents averages of all five samples tested. CIE coordinate (x,y) pairs and corresponding standard deviations for the average values displayed are included in Table C2.

Table 5.2 Voltage-dependent response of CIE coordinates (x,y) at various applied frequencies. CIE coordinates (x,y) correspond to data shown in Figure C8.

	1000 Hz		3000 Hz		5000 Hz		7000Hz		10000 Hz	
Voltage (V)	x	y	x	y	x	y	x	y	x	y
150	0.183	0.504	0.170	0.431	0.166	0.381	0.161	0.348	0.160	0.312
175	0.181	0.505	0.169	0.430	0.163	0.381	0.160	0.346	0.157	0.311
20	0.180	0.505	0.168	0.431	0.162	0.381	0.159	0.346	0.156	0.311
225	0.179	0.507	0.166	0.431	0.162	0.380	0.159	0.345	0.156	0.310
245	0.179	0.507	0.167	0.432	0.162	0.382	0.159	0.348	0.156	0.313

When compared to traditional ACEL device fabrication procedures, one of the major benefits of additive manufacturing and 3D printing is the flexibility in the design and manufacturing process in addition to the reduced production times and minimized material waste. As a potential and relevant application for the work described in this Chapter, I have successfully demonstrated the ability to 3D print customized, color tunable, light emitting devices (Figure 5.9). Similar to the frequency- and voltage-dependent samples tested, the ACEL devices shown in Figure 5.9 were 3D printed and manufactured in less than five minutes by depositing a single layer of PLA/phosphor filament onto an ITO slide sandwiched by the conductive PLA top electrode. I am able to control the luminescent shape and behavior of the ACEL device by modulating the design of the top conductive PLA electrode. Using computer aided design (CAD) software, any design, shape, geometry or logo can be incorporated within ACEL devices in a matter of minutes using this approach. When a voltage is applied to the printed device, the ACEL device only exhibits luminescent behavior where the top electrode is in contact with the PLA/phosphor layer. Regardless of shape or geometrical configuration, all customized 3D-printed samples displayed a color change from green to blue as the excitation frequency was increased.

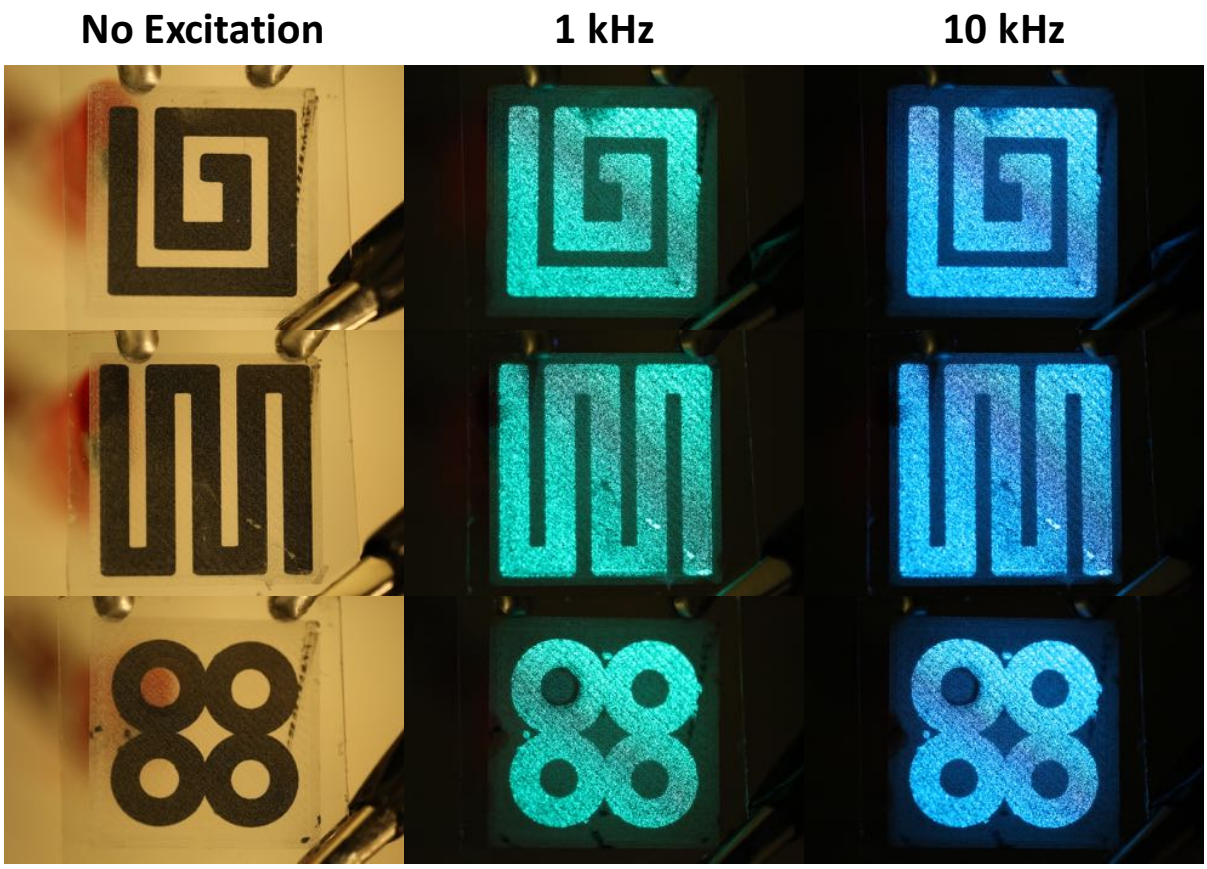

Figure 5.9 Demonstration of custom 3D-printed ACEL devices with various geometric patterns under ambient conditions with no excitation, and with a 245 V source under varying excitation frequencies showing visual changes in color.

5.4 Conclusions

Through materials design considerations, the ability to manufacture functional, active, and responsive ACEL devices using additive manufacturing and 3D-printing approaches was demonstrated in this Chapter. The luminescent performance and response of 3D-printed PLA/phosphor samples was evaluated at various concentrations, where it was found that a 20%-by-weight loading was the optimal concentration of embedded phosphors in the PLA host matrix. For concentrations above 20%, the luminescent response was found to decrease due to inter-particle interactions within the 3D-printed structure. Functional ACEL devices were

fabricated using FDM, where a single layer of PLA/phosphor was directly deposited onto an ITO glass slide and sandwiched between a secondary 3D-printed conductive electrode. When exposed to an external voltage source, 3D-printed ACEL devices were observed to have both voltage-and frequency-dependent responses, where the luminescent color and intensity could be easily modulated. The resultant color of the ACEL device depended exclusively on the applied frequency, where samples shifted from green to blue as the excitation frequency was increased. When the excitation frequency was held constant, though, the brightness and maximum luminescent intensity were linearly related to the applied voltage for the 3D-printed ACEL devices tested in this study. 3D printing offers an alternative approach to rapidly manufacture ACEL devices and stimuli responsive structures, and represents a new way of thinking for the continued development of light emitting components and applications across a variety of uses, fields, and industries.

Chapter 6

Conclusions and Future Work

6.1 Conclusions

In this dissertation, I successfully demonstrate the ability to incorporate a variety of nano- and micron-scale additives within additive manufacturing and 3D printing applications. By focusing on materials processing and design parameters, an overview and approach for how functionalized composite material systems can be designed and developed is thoroughly discussed. Quantum dots, nanoparticles, and phosphors were selected as representative material additives in order to demonstrate the flexibility and scalability of this approach for the continued advancement and development of new material systems compatible with additive manufacturing. In each case, a solution-based mixing process is used to directly combine the nano- and micron-size additives within a PLA polymer host matrix to manufacture and fabricate functionalized 3D printing filament using the following processing steps:

1. Dissolution of PLA polymer host matrix in dichloromethane
2. Addition and mixing of the selected material additive with the dissolved PLA
3. Drying to remove solvent from PLA/composite mixture (ambient conditions)
4. Shredding the resulting hard plastic for use with the filament extrusion system
5. Additional drying to remove any remaining/excess solvent (100 °C)
6. Extrusion of functionalized PLA/composite plastic filament (170 – 180 °C)

As one of the most commonly used plastics in 3D printing, PLA was exclusively used as the host matrix for the development of functionalized materials due in part to its favorable materials properties, including the following four considerations: (1) mutual miscibility with various nanomaterials and additives in solution; (2) minimal optical contributions across the visible spectrum, including both absorbance and emission; (3) relative ease of materials processing; and (4) compatibility with FDM printers. Owing in part to their unique optical response, quantum dots, nanoparticles, and phosphors were each explored for their use in 3D printing to demonstrate the ability to manufacture optically enhanced materials and structures. A variety of material testing and characterization is performed to evaluate the impact that functionalization has on the underlying properties of both the selected additive and PLA polymer host matrix. Process and printing parameters including filament extrusion temperature, printing temperature, build plate temperature, print layer orientation, and print layer height were each held constant between the three material systems to limit the number of possible variables that could impact the recorded material response. Through materials processing considerations, this thesis encompasses and describes the design/development, characterization, inspection, and implementation of functionalized composite materials, devices, and structures for use in 3D printing and additive manufacturing applications.

In Chapter 3, the impact of filament functionalization on the observed material response is evaluated and characterized. Cadmium sulfur selenide graded alloy quantum dots (CdSSe QDs) are incorporated within the PLA polymer host matrix at varying concentrations by weight (ranging from 0.5% to 7%), and the corresponding optical, thermal, and mechanical response of the 3D-printed composite material was studied. Quantum dot concentration and polymer/surface ligand interactions were both found to significantly influence the response of

the functionalized composite system. Although the recorded absorbance compared to CdSSe QDs in solution remained relatively unchanged following materials processing and printing, a significant red shift in the recorded PL spectra was observed with increasing concentrations of quantum dots. In fact, for the highest concentration studied, the location of maximum PL was red shifted 32 nm relative to CdSSe QD in solution, with the recorded photoluminescence intensity reaching a maximum near a 3%-by-weight loading. This behavior was attributed to aggregation between individual quantum dots in the 3D printed films at increasing concentrations, and confirmed through TEM measurements. Furthermore, the presence of CdSSe QDs within the PLA host matrix was found to influence both the thermal and mechanical response of 3D-printed PLA/CdSSe QD systems. The glass transition temperature was found to decrease by 8 °C relative to the unmodified pure PLA host matrix, while ultimate tensile strength decreased by 64% for the highest concentration of CdSSe QDs in PLA tested. These deviations in material properties result from a combination of weak interactions between the natively bound oleic acid surface ligands present on CdSSe QDs and PLA host matrix, and quantum dot aggregation in the final 3D-printed structures. Following materials characterization, light pipes and other passive fluorescent devices were 3D printed based on the optical response of embedded CdSSe QDs, where the overall efficiency and performance was found to be dependent on both the physical dimensions and concentration of embedded quantum dots. An understanding of material behavior following modification and functionalization is a crucial first step in the development of functionalized materials for 3D printing and additive manufacturing applications.

With a better understanding of material response following functionalization, Chapter 4 explores the use of optically enhanced materials for passive sensing applications.

Specifically, the optical properties of gold nanoparticles were harnessed via the development of functionalized printer filament to detect defects and missing print layers in 3D printed parts. Rather than quantum dots, gold nanoparticles were selected for the design of this passive sensing and material inspection methodology based primarily on their long term temporal stability, and to further demonstrate the feasibility of this design process for creating an array of new materials compatible with additive manufacturing. Based on the findings presented in Chapter 3, the overall concentration of embedded gold in PLA was limited to a maximum of 0.2% by weight in an attempt to minimize any negative impacts that functionalization might have on the recorded material response for the samples studied. Thin film samples with increasing thickness ranging from 0.1 mm to 1.0 mm (1 to 10 print layers) were fabricated to evaluate the optical response of the 3D-printed composite. Consistent with Beer-Lambert's law for nanoparticles in solution, a linear relationship between absorbance intensity and the total number of print layers (i.e. material thickness) for the thin film samples tested was observed. Samples with various size defects ranging from 2 to 4 print layers were fabricated, and by analyzing changes in absorbance intensity, the presence, location and extent of material defects as small as 0.2 mm were identified through this nondestructive approach. Control tests were performed on the unmodified pure PLA host matrix, where the presence of defects were unable to be identified based on optical inspection and absorbance measurements. The overall response of the gold nanoparticle functionalized samples was found to be highly stable, as their recorded optical response remained unchanged for more than one year after printing; a crucial consideration in the development of a passive sensing system. The findings outlined in this Chapter provide key insights and considerations for the development of future functionalized 'smart' materials that can be realized through 3D printing.

Beyond passive devices and sensors, Chapter 5 explored the use of phosphor-based additives in the development of active and stimuli responsive 3D-printed material systems. Utilizing the materials design considerations and processes established in Chapters 2, 3, and 4, ZnS:Cu phosphors are incorporated within a PLA host matrix to manufacture alternating current electroluminescent (ACEL) devices using commercially available FDM type 3D printing systems. The optical PL response of the PLA/phosphor composite was evaluated to determine the optimal concentration of embedded phosphors to achieve the brightest luminescent intensity. ACEL devices were fabricated using a multi component approach, where a single layer (100 μm) of PLA/phosphor-functionalized filament was deposited onto a clean ITO-coated conductive glass slide, and sandwiched between an outer layer of 3D-printed carbon-doped conductive PLA serving as a second electrode. As-printed ACEL devices were exposed to a number of voltage- and frequency-dependent excitation cases, and the corresponding optical response was evaluated. Similar to other ACEL devices fabricated using conventional manufacturing approaches such as spin coating and drop casting, a distinct green to blue shift in the recorded emission with increasing excitation frequencies was observed for the 3D printed system. CIE coordinates and other spectral data were evaluated to quantify the response and behavior of this active and stimuli responsive 3D-printed device. The optical response and behavior for 3D-printed ACEL devices were highly stable and reproducible between individual test samples studied. Furthermore, ACEL devices with various geometric shapes were printed to demonstrate the effectiveness and feasibility of additive manufacturing and 3D printing technologies for developing functional and stimuli-responsive parts and components, such as the ACEL devices demonstrated in this Chapter.

6.2 Future Work

With the wide range of relevant topics and related areas of research, additive manufacturing represents a promising direction for the future of materials development and design. By harnessing the unique optical, mechanical, chemical, and thermal behavior of nanoparticles, nanomaterials, and other additives, 3D-printed systems can be tailored to intrinsically respond to a variety of external stimuli and forces for use in a number of diverse fields and applications. Though the work encompassed in this dissertation represents a significant advancement in the field of additive manufacturing material systems as a whole, there are a number of additional research topics that can still be addressed. Namely, the following questions and research topics will be considered as future work in the design and development of new material systems, towards the realization of a complete material lifecycle assessment strategy for 3D-printed parts and components.

- Minimize impact on mechanical and thermal properties of polymer host matrix while still maintaining optical response of selected material additive following material functionalization. Work should focus on evaluating additional material systems in addition to various ligand exchange procedures and surface chemistry/polymer structure interactions to promote favorable interactions between the host matrix and selected material additive.
- Can new, stimuli responsive, materials be developed to visually communicate the presence of external loads acting on a material? The development of a material capable of visually responding to various mechanical, thermal, electrical and chemical loadings would represent a significant advancement for material state/structural health monitoring applications. This work will build

off of previous research I have conducted, in which the use poly-acrylic acid coated gold nanoparticles were capable of responding to changes in pH through a color change visible to the naked eye without the need for additional sensing systems and devices.[152] Additionally, I have demonstrated that white light emitting quantum dots are capable of communicating the presence of mechanical loads when incorporated into a surface coating, so additional testing related to the optical response of 3D printed composites under mechanical loadings should be considered as an alternate sensing methodology.[47]

- Can nanoparticles and other material additives be used to inspect 3D printed parts both during and after the manufacturing process? Though gold nanoparticles are effective for detecting defects as small as the thickness of two pieces of paper, advancements in material inspection for the additive manufacturing process will be necessary for its large scale adoption. This section of future work will focus on incorporating nanoparticles to monitor for defects and discontinuities *during* the manufacturing process, as opposed to in the final part. Here I propose evaluating the optical response of the embedded nanomaterials in real time to monitor for the presence of any non-uniformities, and subsequently correct these observed material defects through a closed-loop feedback system.

REFERENCES

(1) Ning, F.; Cong, W.; Qiu, J.; Wei, J.; Wang, S. Additive Manufacturing of Carbon Fiber Reinforced Thermoplastic Composites Using Fused Deposition Modeling. *Compos. Part B Eng.* **2015**, *80* (October), 369–378.

(2) Wong, K. V.; Hernandez, A. A Review of Additive Manufacturing. *ISRN Mech. Eng.* **2012**, *2012*, 1–10.

(3) Allen, M.; Chen, W.; Wang, C. 3D Printing Standards and Verification Services Introduction: 3-D Printing Verification. *Appl. Innov. Rev. Issue* **2016**, No. 2.

(4) Huang, S. H.; Liu, P.; Mokasdar, A.; Hou, L. Additive Manufacturing and Its Societal Impact: A Literature Review. *Int. J. Adv. Manuf. Technol.* **2013**, *67*, 1191–1203.

(5) Conner, B. P.; Manogharan, G. P.; Martof, A. N.; Rodomsky, L. M.; Rodomsky, C. M.; Jordan, D. C.; Limperos, J. W. Making Sense of 3-D Printing: Creating a Map of Additive Manufacturing Products and Services. *Addit. Manuf.* **2014**, *1*, 64–76.

(6) ISO/ASTM. Standard Terminology for Additive Manufacturing – General Principles – Terminology. *ASTM Int.* **2015**, *i*, 1–9.

(7) Kruth, J. P. Material Incress Manufacturing by Rapid Prototyping Techniques. *CIRP Ann. - Manuf. Technol.* **1991**, *40* (2), 603–614.

(8) Calignano, F.; Manfredi, D.; Ambrosio, E. P.; Biamino, S.; Lombardi, M.; Atzeni, E.; Salmi, A.; Minetola, P.; Iuliano, L.; Fino, P. Overview on Additive Manufacturing Technologies. *Proc. IEEE* **2017**, *105* (4), 593–612.

(9) Dudek, P. FDM 3D Printing Technology in Manufacturing Composite Elements. *Arch. Metall. Mater.* **2013**, *58* (4), 1415–1418.

(10) Lebaron, P. C.; Wang, Z.; Pinnavaia, T. J. Polymer-Layered Silicate Nanocomposites: An Overview. *Appl. Clay Sci.* **1999**, *15*, 11–29.

(11) Kasemann, R.; Schmidt, H. Coating for Mechanical and Chemical Protection Based on Organic-Inorganic Sol-Gel Nanocomposites. *New J. Chem.* **1994**, *18*, 1117–1123.

(12) Beecroft, L. L.; Ober, C. K. Nanocomposite Materials for Optical Applications. *Chem. Mater.* **1997**, *9* (6), 1302–1317.

(13) Campbell, T. A.; Ivanova, O. S. 3D Printing of Multifunctional Nanocomposites. *Nano Today* **2013**, *8*, 119–120.

(14) Gao, W.; Zhang, Y.; Ramanujan, D.; Ramani, K.; Chen, Y.; Williams, C. B.; Wang, C. C. L.; Shin, Y. C.; Zhang, S.; Zavattieri, P. D.; Gao, W. The Status, Challenges, and Future of Additive Manufacturing in Engineering. *Comput. Des.* **2015**, *69*, 65–89.

(15) Weng, Z.; Wang, J.; Senthil, T.; Wu, L. Mechanical and Thermal Properties of ABS/Montmorillonite Nanocomposites for Fused Deposition Modeling 3D Printing. *Mater. Des.* **2016**, *102*, 276–283.

(16) Gnanasekaran, K.; Heijmans, T.; van Bennekom, S.; Woldhuis, H.; Wijnia, S.; de With, G.; Friedrich, H. 3D Printing of CNT- and Graphene-Based Conductive Polymer Nanocomposites by Fused Deposition Modeling. *Appl. Mater. Today* **2017**, *9*, 21–28.

(17) Kim, K.; Park, J.; Suh, J.; Kim, M.; Jeong, Y.; Park, I. 3D Printing of Multiaxial Force Sensors Using Carbon Nanotube (CNT)/Thermoplastic Polyurethane (TPU) Filaments. *Sensors Actuators A Phys.* **2017**, *263*, 493–500.

(18) Kennedy, Z. C.; Christ, J. F.; Evans, K. A.; Arey, B. W.; Sweet, L. E.; Warner, M. G.;

Erikson, R. L.; Barrett, C. A. 3D-Printed Poly(Vinylidene Fluoride)/Carbon Nanotube Composites as a Tunable, Low-Cost Chemical Vapour Sensing Platform. *Nanoscale* **2017**, *9* (17), 5458–5466.
(19) Guo, S. Z.; Qiu, K.; Meng, F.; Park, S. H.; Mcalpine, M. C. 3D Printed Stretchable Tactile Sensors. *Adv. Mater.* **2017**, *1701218*, 1–8.
(20) Haring, A. P.; Khan, A. U.; Liu, G.; Johnson, B. N. 3D Printed Functionally Graded Plasmonic Constructs. *Advanced Optical Materials*. 2017, pp 1–9.
(21) Farahani, R. D.; Dubé, M.; Therriault, D. Three-Dimensional Printing of Multifunctional Nanocomposites: Manufacturing Techniques and Applications. *Adv. Mater.* **2016**, *28*, 5794–5821.
(22) Kim, T. Y.; Kim, I.; Park, J.-J.; Kim, T. Y.; Kim, S. I.; Park, J.-J. Fabrication of Thermally Stable Silver–Organic Complex (TS-SOC) Based Conductible Filament Materials for 3D Printing. *Adv. Mater. Technol.* **2017**, *17000791* (9).
(23) Skorski, M. R.; Esenther, J. M.; Ahmed, Z.; Miller, A. E.; Hartings, M. R. The Chemical, Mechanical, and Physical Properties of 3D Printed Materials Composed of TiO2-ABS Nanocomposites. *Sci. Technol. Adv. Mater.* **2016**, *17* (1), 89–97.
(24) Brubaker, C. D.; Davies, M. A.; McBride, J. R.; Rosenthal, S. J.; Kane Jennings, G.; Adams, D. E. Nondestructive Evaluation and Detection of Defects in 3D Printed Materials Using the Optical Properties of Gold Nanoparticles. *Appl. Nano Mater.* **2018**, *1* (3), 1377–1384.
(25) Zhang, D.; Chi, B.; Li, B.; Gao, Z.; Du, Y.; Guo, J.; Wei, J. Fabrication of Highly Conductive Graphene Flexible Circuits by 3D Printing. *Synth. Met.* **2016**, *217*, 79–86.
(26) Zhang, Q.; Zhang, F.; Medarametla, S. P.; Li, H.; Zhou, C.; Lin, D. 3D Printing of Graphene Aerogels. *Small* **2016**, *12* (13), 1702–1708.
(27) Wang, X.; Jiang, M.; Zhou, Z.; Gou, J.; Hui, D. 3D Printing of Polymer Matrix Composites: A Review and Prospective. *Composites Part B: Engineering*. February 2017, pp 442–458.
(28) Tekinalp, H. L.; Kunc, V.; Velez-Garcia, G. M.; Duty, C. E.; Love, L. J.; Naskar, A. K.; Blue, C. A.; Ozcan, S. Highly Oriented Carbon Fiber-Polymer Composites via Additive Manufacturing. *Compos. Sci. Technol.* **2014**, *105*, 144–150.
(29) Ning, F.; Cong, W.; Qiu, J.; Wei, J.; Wang, S. Additive Manufacturing of Carbon Fiber Reinforced Thermoplastic Composites Using Fused Deposition Modeling. *Compos. Part B Eng.* **2015**, *80*, 369–378.
(30) Tubío, C. R.; Azuaje, J.; Escalante, L.; Coelho, A.; Guitián, F.; Sotelo, E.; Gil, A. 3D Printing of a Heterogeneous Copper-Based Catalyst. *J. Catal.* **2016**, *334*, 110–115.
(31) Gupta, M. K.; Meng, F.; Johnson, B. N.; Kong, Y. L.; Tian, L.; Yeh, Y. W.; Masters, N.; Singamaneni, S.; McAlpine, M. C. 3D Printed Programmable Release Capsules. *Nano Lett.* **2015**, *15* (8), 5321–5329.
(32) Goyanes, A.; Wang, J.; Buanz, A.; Martínez-Pacheco, R.; Telford, R.; Gaisford, S.; Basit, A. W. 3D Printing of Medicines: Engineering Novel Oral Devices with Unique Design and Drug Release Characteristics. *Mol. Pharm.* **2015**, *12* (11), 4077–4084.
(33) Drumright, R. E.; Gruber, P. R.; Henton, D. E. Polylactic Acid Technology. *Adv. Mater.* **2000**, *12* (23), 1841–1846.
(34) den Eynde, M. Van; Van Puyvelde, P. 3D Printing of Polylactic Acid. In *Advances in Polymer Sciences*; Springer, Berlin, Heidelberg, 2017; pp 1–20.
(35) Sarasua, J. R.; Arraiza, A. L.; Balerdi, P.; Maiza, I. Crystallinity and Mechanical

Properties of Optically Pure Polylactides and Their Blends. *Polym. Eng. Sci.* **2005**, *45* (5), 745–753.
(36) Sato, S.; Gondo, D.; Wada, T.; Kanehashi, S.; Nagai, K. Effects of Various Liquid Organic Solvents on Solvent-Induced Crystallization of Amorphous Poly(Lactic Acid) Film. *J. Appl. Polym. Sci.* **2013**, *129* (3), 1607–1617.
(37) Jamshidian, M.; Tehrany, E. A.; Imran, M.; Jacquot, M.; Desobry, S. Poly-Lactic Acid: Production, Applications, Nanocomposites, and Release Studies. *Compr. Rev. Food Sci. Food Saf.* **2010**, *9* (5), 552–571.
(38) Lim, L.-T.; Auras, R.; Rubino, M. Processing Technologies for Poly(Lactic Acid). *Prog. Polym. Sci.* **2008**, *33* (8), 820–852.
(39) Lasprilla, A. J. R.; Martinez, G. A. R.; Lunelli, B. H.; Jardini, A. L.; Filho, R. M. Poly-Lactic Acid Synthesis for Application in Biomedical Devices - A Review. *Biotechnology Advances*. Elsevier January 1, 2012, pp 321–328.
(40) Castillo Martinez, F. A.; Balciunas, E. M.; Salgado, J. M.; Domínguez González, J. M.; Converti, A.; Oliveira, R. P. de S. Lactic Acid Properties, Applications and Production: A Review. *Trends in Food Science and Technology*. Elsevier March 1, 2013, pp 70–83.
(41) Alivaisatos, A. P. Semiconductor Custers, Nanocrystals, and Quantum Dots. *Science (80-.).* **1996**, *271*.
(42) Sargent, E. H. Colloidal Quantum Dot Solar Cells. *Nat. Photonics* **2012**, *6* (3), 133–135.
(43) Niezgoda, J. S.; Yap, E.; Keene, J. D.; Mcbride, J. R.; Rosenthal, S. J. Plasmonic Cu x In y S 2 Quantum Dots Make Better Photovoltaics Than Their Nonplasmonic Counterparts. *Nano Lett.* **2014**, *14*, 3262–3269.
(44) Kovtun, O.; Sakrikar, D.; Tomlinson, I. D.; Chang, J. C.; Arzeta-Ferrer, X.; Blakely, R. D.; Rosenthal, S. J. Single-Quantum-Dot Tracking Reveals Altered Membrane Dynamics of an Attention-Deficit/Hyperactivity-Disorder-Derived Dopamine Transporter Coding Variant. *ACS Chem. Neurosci.* **2015**, *6*, 526–534.
(45) Yang, Y.; Zheng, Y.; Cao, W.; Titov, A.; Hyvonen, J.; Manders, J. R.; Xue, J.; Holloway, P. H.; Qian, L. High-Efficiency Light-Emitting Devices Based on Quantum Dots with Tailored Nanostructures. *Nat. Photonics* **2015**, *9* (4), 259–265.
(46) Kim, T.-H.; Cho, K.-S.; Lee, E. K.; Lee, S. J.; Chae, J.; Kim, J. W.; Kim, D. H.; Kwon, J.-Y.; Amaratunga, G.; Lee, S. Y.; Choi, B. L.; Kuk, Y.; Kim, J. M.; Kim, K. Full-Colour Quantum Dot Displays Fabricated by Transfer Printing. *Nat. Photonics* **2011**, *5*, 176–182.
(47) Brubaker, C. D.; Frecker, T. M.; Njoroge, I.; Shane, D. O.; Smudde, C. M.; Rosenthal, S. J.; Jennings, G. K.; Adams, D. E. In-Situ Material State Monitoring Using Embedded CdSe Quantum Dots. In *Sensors and Smart Structures Technologies for Civil, Mechanical, and Aerospace Systems*; 2016; Vol. 9803, pp 1–14.
(48) Baskoutas, S.; Terzis, A. F. Size-Dependent Band Gap of Colloidal Quantum Dots. *J. Appl. Phys.* **2006**, *99* (1), 13708.
(49) Alivisatos, A. P. Semiconductor Clusters, Nanocrystals, and Quantum Dots. *Science (80-.).* **1996**, *271* (5251), 933–937.
(50) Frecker, T.; Bailey, D.; Arzeta-Ferrer, X.; McBride, J.; Rosenthal, S. J. Review—Quantum Dots and Their Application in Lighting, Displays, and Biology. *ECS J. Solid State Sci. Technol.* **2016**, *5* (1), R3019–R3031.
(51) Evans, C. M.; Cass, L. C.; Knowles, K. E.; Tice, D. B.; Chang, R. P. H.; Weiss, E. A. Review of the Synthesis and Properties of Colloidal Quantum Dots: The Evolving Role

of Coordinating Surface Ligands. *J. Coord. Chem.* **2012**, *65* (13), 2391–2414.
(52) Pu, Y.; Cai, F.; Wang, D.; Wang, J. X.; Chen, J. F. Colloidal Synthesis of Semiconductor Quantum Dots toward Large-Scale Production: A Review. *Industrial and Engineering Chemistry Research*. American Chemical Society February 14, 2018, pp 1790–1802.
(53) Daniel, M. C. M.; Astruc, D. Gold Nanoparticles: Assembly, Supramolecular Chemistry, Quantum-Size Related Properties and Applications toward Biology, Catalysis and Nanotechnology. *Chem. Rev.* **2004**, *104*, 293–346.
(54) Han, X.; Liu, Y.; Yin, Y. Colorimetric Stress Memory Sensor Based on Disassembly of Gold Nanoparticle Chains. *Nano Lett.* **2014**, *14* (5), 2466–2470.
(55) Liu, Y.; Han, X.; He, L.; Yin, Y. Thermoresponsive Assembly of Charged Gold Nanoparticles and Their Reversible Tuning of Plasmon Coupling. *Angew. Chemie - Int. Ed.* **2012**, *51* (26), 6373–6377.
(56) Li, D.; He, Q.; Yang, Y.; Möhwald, H.; Li, J. Two-Stage PH Response of Poly(4-Vinylpyridine) Grafted Gold Nanoparticles. *Macromolecules* **2008**, *41* (19), 7254–7256.
(57) Stover, R. J.; Moaseri, E.; Gourisankar, S. P.; Iqbal, M.; Rahbar, N. K.; Changalvaie, B.; Truskett, T. M.; Johnston, K. P. Formation of Small Gold Nanoparticle Chains with High NIR Extinction through Bridging with Calcium Ions. *Langmuir* **2016**, *32* (4), 1127–1138.
(58) Xiao, R. P.; Wang, D. F.; Lin, Z. Y.; Qiu, B.; Liu, M. H.; Guo, L. H.; Chen, G. N. Disassembly of Gold Nanoparticle Dimers for Colorimetric Detection of Ochratoxin A. *Anal. Methods* **2015**, *7* (3), 842–845.
(59) Eustis, S.; El-Sayed, M. A. Why Gold Nanoparticles Are More Precious than Pretty Gold: Noble Metal Surface Plasmon Resonance and Its Enhancement of the Radiative and Nonradiative Properties of Nanocrystals of Different Shapes. *Chem. Soc. Rev.* **2006**, *35* (3), 209–217.
(60) Sharifi, A.; Hassani, B. Vacuum Drying of Barberry Fruit (Berberis Vulgaris) and Selection of a Suitable Thin Layer Drying Model. *Res. J. Appl. Sci. Eng. Technol.* **2013**, *5* (5), 1668–1673.
(61) Shim, H.; Allabergenov, B.; Kim, J.; Noh, H. Y.; Lyu, H. K.; Lee, M. J.; Choi, B. Highly Bright Flexible Electroluminescent Devices with Retroreflective Electrodes. *Adv. Mater. Technol.* **2017**, *2* (9).
(62) Fang, H.; Tian, H.; Li, J.; Li, Q.; Dai, J.; Ren, T. L.; Dong, G.; Yan, Q. Self-Powered Flat Panel Displays Enabled by Motion-Driven Alternating Current Electroluminescence. *Nano Energy* **2016**, *20*, 48–56.
(63) Bredol, M.; Dieckhoff, H. S. Materials for Powder-Based AC-Electroluminescence. *Materials (Basel)*. **2010**, *3* (2), 1353–1374.
(64) Hu, B.; Li, D.; Ala, O.; Manandhar, P.; Fan, Q.; Kasilingam, D.; Calvert, P. D. Textile-Based Flexible Electroluminescent Devices. *Adv. Funct. Mater.* **2011**, *21* (2), 305–311.
(65) Xu, C. N.; Watanabe, T.; Akiyama, M.; Zheng, X. G. Artificial Skin to Sense Mechanical Stress by Visible Light Emission. *Appl. Phys. Lett.* **1999**, *74* (9), 1236–1238.
(66) Krishnan, S.; Van der Walt, H.; Venkatesh, V.; Sundaresan, V. B. Dynamic Characterization of Elastico-Mechanoluminescence towards Structural Health Monitoring. *J. Intell. Mater. Syst. Struct.* **2017**, *28* (17), 2458–2464.
(67) Xu, X.; Hu, D.; Yan, L.; Fang, S.; Shen, C.; Loo, Y. L.; Lin, Y.; Haines, C. S.; Li, N.;

Zakhidov, A. A.; Meng, H.; Baughman, R. H.; Huang, W. Polar-Electrode-Bridged Electroluminescent Displays: 2D Sensors Remotely Communicating Optically. *Adv. Mater.* **2017**, *29* (41).

(68) Wood, V.; Halpert, J. E.; Panzer, M. J.; Bawendi, M. G.; Bulović, V. Alternating Current Driven Electroluminescence from ZnSe/ZnS:Mn/ZnS Nanocrystals. *Nano Lett.* **2009**, *9* (6), 2367–2371.

(69) Park, J. H.; Lee, S. H.; Kim, J. S.; Kwon, A. K.; Park, H. L.; Han, S. Do. White-Electroluminescent Device with ZnS:Mn, Cu, Cl Phosphor. *J. Lumin.* **2007**, *126* (2), 566–570.

(70) Jeong, S. M.; Song, S.; Lee, S. K.; Ha, N. Y. Color Manipulation of Mechanoluminescence from Stress-Activated Composite Films. *Adv. Mater.* **2013**, *25* (43), 6194–6200.

(71) Moon Jeong, S.; Song, S.; Lee, S. K.; Choi, B. Mechanically Driven Light-Generator with High Durability. *Appl. Phys. Lett.* **2013**, *102* (5), 51110.

(72) Chandra, V. K.; Chandra, B. P.; Jha, P. Self-Recovery of Mechanoluminescence in ZnS:Cu and ZnS:Mn Phosphors by Trapping of Drifting Charge Carriers. *Appl. Phys. Lett.* **2013**, *103* (16), 161113.

(73) Jeong, S. M.; Song, S.; Kim, H. Simultaneous Dual-Channel Blue/Green Emission from Electro-Mechanically Powered Elastomeric Zinc Sulphide Composite. *Nano Energy* **2016**, *21*, 154–161.

(74) Wang, X.; Zhang, H.; Yu, R.; Dong, L.; Peng, D.; Zhang, A.; Zhang, Y.; Liu, H.; Pan, C.; Wang, Z. L. Dynamic Pressure Mapping of Personalized Handwriting by a Flexible Sensor Matrix Based on the Mechanoluminescence Process. *Adv. Mater.* **2015**, *27* (14), 2324–2331.

(75) Zhang, Y.; Gao, G.; Chan, H. L. W.; Dai, J.; Wang, Y.; Hao, J. Piezo-Phototronic Effect-Induced Dual-Mode Light and Ultrasound Emissions from ZnS:Mn/PMN-PT Thin-Film Structures. *Adv. Mater.* **2012**, *24* (13), 1729–1735.

(76) Bowers, M. J.; McBride, J. R.; Rosenthal, S. J. White-Light Emission from Magic-Sized Cadmium Selenide Nanocrystals. *J. Am. Chem. Soc.* **2005**, *127* (44), 15378–15379.

(77) Keene, J. D.; McBride, J. R.; Orfield, N. J.; Rosenthal, S. J. Elimination of Hole-Surface Overlap in Graded CdSxSe1- x Nanocrystals Revealed by Ultrafast Fluorescence Upconversion Spectroscopy. *ACS Nano* **2014**, *8* (10), 10665–10673.

(78) Shen, Y.; Gee, M. Y.; Tan, R.; Pellechia, P. J.; Greytak, A. B. Purification of Quantum Dots by Gel Permeation Chromatography and the Eeffect of Excess Ligands on Shell Growth and Ligand Exchange. *Chem. Mater.* **2013**, *25* (14), 2838–2848.

(79) Jans, H.; Jans, K.; Lagae, L.; Borghs, G.; Maes, G.; Huo, Q. Poly(Acrylic Acid)-Stabilized Colloidal Gold Nanoparticles: Synthesis and Properties. *Nanotechnology* **2010**, *21* (45), 455702.

(80) Kimling, J.; Maier, M.; Okenve, B.; Kotaidis, V.; Ballot, H.; Plech, A. Turkevich Method for Gold Nanoparticle Synthesis Revisited. *J. Phys. Chem. B* **2006**, *110* (32), 15700–15707.

(81) Guarrotxena, N.; Quijada-Garrido, I. Optical and Swelling Stimuli-Response of Functional Hybrid Nanogels: Feasible Route to Achieve Tunable Smart Core@Shell Plasmonic@Polymer Nanomaterials. *Chem. Mater.* **2016**, *28* (5), 1402–1412.

(82) Lawrence, J.; Pham, J. T.; Lee, D. Y.; Liu, Y.; Crosby, A. J.; Emrick, T. Highly Conductive Ribbons Prepared by Stick–Slip Assembly of Organosoluble Gold

Nanoparticles. *ACS Nano* **2014**, *8* (2), 1173–1179.
(83) Zheng, N.; Fan, J.; Stucky, G. D. One-Step One-Phase Synthesis of Monodisperse Noble-Metallic Nanoparticles and Their Colloidal Crystals. *J. Am. Chem. Soc.* **2006**, *128* (20), 6550–6551.
(84) Schreuder, M. a.; Gosnell, J. D.; Smith, N. J.; Warnement, M. R.; Weiss, S. M.; Rosenthal, S. J. Encapsulated White-Light CdSe Nanocrystals as Nanophosphors for Solid-State Lighting. *J. Mater. Chem.* **2008**, *18* (9), 970.
(85) Tymrak, B. M.; Kreiger, M.; Pearce, J. M. Mechanical Properties of Components Fabricated with Open-Source 3-D Printers under Realistic Environmental Conditions. *Mater. Des.* **2014**, *58*, 242–246.
(86) Sood, A. K.; Ohdar, R. K.; Mahapatra, S. S. Parametric Appraisal of Mechanical Property of Fused Deposition Modelling Processed Parts. *Mater. Des.* **2010**, *31* (1), 287–295.
(87) Raut, S.; Jatti, V. S.; Khedkar, N. K.; Singh, T. P. Investigation of the Effect of Built Orientation on Mechanical Properties and Total Cost of FDM Parts. *Procedia Mater. Sci.* **2014**, *6*, 1625–1630.
(88) Brubaker, C. D.; Frecker, T. M.; McBride, J. R.; Reid, K. R.; Jennings, G. K.; Rosenthal, S. J.; Adams, D. E. Incorporation of Fluorescent Quantum Dots for 3D Printing and Additive Manufacturing Applications. *J. Mater. Chem. C* **2018**, *6* (28), 7584–7593.
(89) Kong, Y. L.; Tamargo, I. a; Kim, H.; Johnson, B. N.; Gupta, M. K.; Koh, T. W.; Chin, H. A.; Steingart, D. a; Rand, B. P.; McAlpine, M. C. 3D Printed Quantum Dot Light-Emitting Diodes. *Nano Lett.* **2014**, *14* (12), 7017–7023.
(90) Zhang, Q.-H.; Tian, Y.; Wang, C.-F.; Chen, S.; Li, L.; Herbich, J.; Golec, B.; Wielgus, I.; Pron, A.; Wei, X. J.; Wang, S. G.; Zhang, J. T.; Du, Y.; Dou, S. X.; Zhu, H. S. Construction of Ag-Doped Zn–In–S Quantum Dots toward White LEDs and 3D Luminescent Patterning. *RSC Adv.* **2016**, *6* (53), 47616–47622.
(91) Danek, M.; Jensen, K. F.; Murray, C. B.; Bawendi, M. G. Synthesis of Luminescent Thin-Film CdSe / ZnSe Quantum Dot Composites Using CdSe Quantum Dots Passivated with an Overlayer of ZnSe. *Chem. Mater.* **1996**, *8* (3), 173–180.
(92) Harrison, M. A.; Ng, A.; Hmelo, A. B.; Rosenthal, S. J. CdSSe Nanocrystals with Induced Chemical Composition Gradients. *Isr. J. Chem.* **2012**, *52* (11–12), 1063–1072.
(93) Xu, J.; Wang, J.; Mitchell, M.; Mukherjee, P.; Jeffries-El, M.; Petrich, J. W.; Lin, Z. Organic-Inorganic Nanocomposites via Directly Grafting Conjugated Polymers onto Quantum Dots. *J. Am. Chem. Soc.* **2007**, *129* (42), 12828–12833.
(94) Kagan, C. R.; Murray, C. B.; Nirmal, M.; Bawendi, M. G. Electronic Energy Transfer in CdSe Quantum Dot Solids. *Phys. Rev. Lett.* **1996**, *76* (9), 1517–1520.
(95) Rittigstein, P.; Torkelson, J. M. Polymer-Nanoparticle Interfacial Interactions in Polymer Nanocomposites: Confinement Effects on Glass Transition Temperature and Suppression of Physical Aging. *J. Polym. Sci. Part B Polym. Phys.* **2006**, *44* (20), 2935–2943.
(96) Ash, B. J.; Siegel, R. W.; Schadler, L. S. Glass-Transition Temperature Behavior of Alumina/PMMA Nanocomposites. *J. Polym. Sci. Part B Polym. Phys.* **2004**, *42* (23), 4371–4383.
(97) Belgacem, M.; Gandini, A. *Monomers, Polymers and Composites from Renewable Resources*, 1st ed.; Elsevier Science, Amsterdam, 2008.
(98) Martin, O.; Averous, L. Plasticization and Properties of Biodegradable Multiphase

Systems Polymer. *Polymer (Guildf)*. **2001**, *42*, 6209–6219.
(99) Qiao, R.; Deng, H.; Putz, K. W.; Brinson, L. C. Effect of Particle Agglomeration and Interphase on the Glass Transition Temperature of Polymer Nanocomposites. *J. Polym. Sci. Part B Polym. Phys.* **2011**, *49* (10), 740–748.
(100) Ramanathan, T.; Liu, H.; Brinson, L. C. Functionalized SWNT/Polymer Nanocomposites for Dramatic Property Improvement. *J. Polym. Sci. Part B Polym. Phys.* **2005**, *43* (17), 2269–2279.
(101) Hamming, L.; Qiao, R.; Messersmith, P.; Brinson, L. Effects of Dispersion and Interfacial Modification on the Macorscale Properties of TiO2 Polymer Matrix Nanocomposites. *Compos. Sci. Technol.* **2009**, *69* (11–12), 1880–1886.
(102) Bansal, A.; Yang, H.; Li, C.; Cho, K.; Benicewicz, B. C.; Kumar, S. K.; Schadler, L. S. Quantitative Equivalence between Polymer Nanocomposites and Thin Polymer Films. *Nat. Mater.* **2005**, *4* (9), 693–698.
(103) Baiardo, M.; Frisoni, G.; Scandola, M.; Rimelen, M.; Lips, D.; Ruffieux, K.; Wintermantel, E. Thermal and Mechanical Properties of Plasticized Poly(l-Lactic Acid). *J Appl Polym Sci* **2003**, *90*, 1731–1738.
(104) Pillin, I.; Montrelay, N.; Grohens, Y. Thermo-Mechanical Characterization of Plasticized PLA: Is the Miscibility the Only Significant Factor? *Polymer (Guildf)*. **2006**, *47* (13), 4676–4682.
(105) Ash, B. J.; Rogers, D. F.; Wiegand, C. J.; Schadler, L. S.; Siegel, R. W.; Benicewicz, B. C.; Apple, T. Mechanical Properties of Al2O3/Polymethylmethacrylate Nanocomposites. *Polym. Compos.* **2002**, *23* (6), 1014–1025.
(106) Xu, W.; Raychowdhury, S.; Jiang, D. D.; Retsos, H.; Giannelis, E. P. Dramatic Improvements in Toughness in Poly(Lactide-Co-Glycolide) Nanocomposites. *Small* **2008**, *4* (5), 662–669.
(107) Lee, J. Y.; Su, K. E.; Chan, E. P.; Zhang, Q.; Emrick, T.; Crosby, A. J. Impact of Surface-Modified Nanoparticles on Glass Transition Temperature and Elastic Modulus of Polymer Thin Films. *Macromolecules* **2007**, *40* (22), 7755–7757.
(108) Boyle, B. M.; French, T. A.; Pearson, R. M.; McCarthy, B. G.; Miyake, G. M. Structural Color for Additive Manufacturing: 3D-Printed Photonic Crystals from Block Copolymers. *ACS Nano* **2017**, *11* (3), 3052–3058.
(109) Van Derlofske, J. F. Computer Modeling of LED Light Pipe Systems for Uniform Display Illumination. *Proc. SPIE* **2001**, *4445* (518), 119–129.
(110) Surez, I.; Gordillo, H.; Abargues, R.; Albert, S.; Martínez-Pastor, J. Photoluminescence Waveguiding in CdSe and CdTe QDs-PMMA Nanocomposite Films. *Nanotechnology* **2011**, *22* (43), 435202.
(111) Zeltmann, S. E.; Gupta, N.; Tsoutsos, N. G.; Maniatakos, M.; Rajendran, J.; Karri, R. Manufacturing and Security Challenges in 3D Printing. *Jom* **2016**, *68* (7), 1872–1881.
(112) Straub, J. An Approach to Detecting Deliberately Introduced Defects and Micro-Defects in 3D Printed Objects. *Proc. SPIE - Int. Soc. Opt. Eng.* **2017**, *10203*.
(113) Yadollahi, A.; Shamsaei, N. Additive Manufacturing of Fatigue Resistant Materials: Challenges and Opportunities. *Int. J. Fatigue* **2017**, *98*, 14–31.
(114) Beretta, S.; Romano, S. A Comparison of Fatigue Strength Sensitivity to Defects for Materials Manufactured by AM or Traditional Processes. *Int. J. Fatigue* **2017**, *94*, 178–191.
(115) Romano, S.; Brandão, A.; Gumpinger, J.; Gschweitl, M.; Beretta, S. Qualification of

AM Parts: Extreme Value Statistics Applied to Tomographic Measurements. *Mater. Des.* **2017**, *131* (April), 32–48.
(116) Bhaumik, S. K.; Sujata, M.; Venkataswamy, M. A. Fatigue Failure of Aircraft Components. *Eng. Fail. Anal.* **2008**, *15* (6), 675–694.
(117) Weeren, R. Van; Agarwala, M.; Jamalabad, V. R.; Bandyophadyay, A. Quality of Parts Processed by Fused Deposition. *Proc. Solid Free. Fabr. Symp.* **1995**, *6*, 314–321.
(118) Duty, C. E.; Kunc, V.; Compton, B.; Post, B.; Erdman, D.; Smith, R.; Lind, R.; Lloyd, P.; Love, L. Structure and Mechanical Behavior of Big Area Additive Manufacturing (BAAM) Materials. *Rapid Prototyp. J.* **2017**, *23* (1), 181–189.
(119) Bayens, C.; Le, T.; Garcia, L.; Bayens, C.; Garcia, L. See No Evil , Hear No Evil , Feel No Evil , Print No Evil ? Malicious Fill Patterns Detection in Additive Manufacturing This Paper Is Included in the Proceedings of The. *USENIX Secur.* **2017**.
(120) Bridges, S. M.; Hall, S. T.; Graves, S. J.; Hall, S. a T.; Keiser, K.; Hall, S. T.; Sissom, N.; Hall, S. T. Cyber Security for Additive Manufacturing. **2015**, 1–3.
(121) Rokka Chhetri, S.; Canedo, A. KCAD: Kinetic Cyber Attack Detection Method for Cyber-Physical Additive Manufacturing Systems. In *Proceedings of the 35th International Conference on Computer-Aided Design*; 2016.
(122) Cerniglia, D.; Scafidi, M.; Pantano, A.; Rudlin, J. Inspection of Additive-Manufactured Layered Components. *Ultrasonics* **2015**, *62*, 292–298.
(123) Wu, M.; Phoha, V. V.; Moon, Y. B.; Belman, A. K. Detecting Malicious Defects in 3D Printing Process Using Machine Learning and Image Classification. In *Volume 14: Emerging Technologies; Materials: Genetics to Structures; Safety Engineering and Risk Analysis*; ASME, 2016; p V014T07A004.
(124) Albakri, M.; Sturm, L.; Williams, C. B.; Tarazaga, P. Non-Destructive Evaluation of Additively Manufactured Parts Via Impedance-Based Monitoring. *Solid Free. Fabr. Symp.* **2015**.
(125) Zeltmann, S. E.; Gupta, N.; Tsoutsos, N. G.; Maniatakos, M.; Rajendran, J.; Karri, R. Manufacturing and Security Challenges in 3D Printing. *JOM* **2016**, *68* (7), 1872–1881.
(126) Hennek, C.; Nemiroski, A.; Bala Subramaniam, A.; Bwambok, D. K.; Yang, D.; Harburg, D. V; Tricard, S.; Ellerbee, A. K.; Whitesides, G. M.; Hennek, J. W. Using Magnetic Levitation for Non-Destructive Quality Control of Plastic Parts. *Adv. Mater.* **2015**, *27* (9), 1587–1592.
(127) Rao, P. K.; Liu, J. (Peter); Roberson, D.; Kong, Z. (James); Williams, C. Online Real-Time Quality Monitoring in Additive Manufacturing Processes Using Heterogeneous Sensors. *J. Manuf. Sci. Eng.* **2015**, *137* (6), 061007.
(128) Sarah K. Everton, Matthias Hirsch, Petros Stravroulakis, Richard K. Leach, A. T. C. Review of in Situ Process Monitoring and in Situ Metrology for Metal Additive Manufacturing. *Mater. Des.* **2016**, *95*, 431–445.
(129) Gong, X.; Pan, L.; Tang, C. Y.; Chen, L.; Hao, Z.; Law, W.-C.; Wang, X.; Tsui, C. P.; Wu, C. Preparation, Optical and Thermal Properties of CdSe-ZnS/Poly(Lactic Acid) (PLA) Nanocomposites. *Compos. Part B* **2014**, *66*, 494–499.
(130) Garlotta, D. A Literature Review of Poly(Lactic Acid). *J. Polym. Environ.* **2001**, *9* (2), 63–84.
(131) Chahal, R. P.; Mahendia, S.; Tomar, A. K.; Kumar, S. UV Irradiated PVA–Ag Nanocomposites for Optical Applications. *Appl. Surf. Sci.* **2015**, *343*, 160–165.
(132) Larson, C.; Peele, B.; Li, S.; Robinson, M.; Beccai, L.; Mazzolai, B.; Shepherd, R.

Highly Stretchable Electroluminescent Skin for Optical Signaling and Tactile Sensing. *Science (80-.).* **2016**, *351* (6277), 1071–1074.
(133) Jeong, S. M.; Song, S.; Joo, K. Il; Kim, J.; Hwang, S. H.; Jeong, J.; Kim, H. Bright, Wind-Driven White Mechanoluminescence from Zinc Sulphide Microparticles Embedded in a Polydimethylsiloxane Elastomer. *Energy Environ. Sci.* **2014**, *7* (10), 3338–3346.
(134) Chen, L.; Wong, M. C.; Bai, G.; Jie, W.; Hao, J. White and Green Light Emissions of Flexible Polymer Composites under Electric Field and Multiple Strains. *Nano Energy* **2015**, *14*, 372–381.
(135) Jun, S.; Kim, Y.; Ju, B. K.; Kim, J. W. Extremely Flexible, Transparent, and Strain-Sensitive Electroluminescent Device Based on ZnS:Cu-Polyvinyl Butyral Composite and Silver Nanowires. *Appl. Surf. Sci.* **2018**, *429*, 144–150.
(136) Terasaki, N.; Yamada, H.; Xu, C. N. Ultrasonic Wave Induced Mechanoluminescence and Its Application for Photocatalysis as Ubiquitous Light Source. *Catal. Today* **2013**, *201* (1), 203–208.
(137) Wang, X.; Xu, C. N.; Yamada, H.; Nishikubo, K.; Zheng, X. G. Electro-Mechano-Optical Conversions in Pr3+-Doped BaTiO3-CaTiO3ceramics. *Adv. Mater.* **2005**, *17* (10), 1254–1258.
(138) Wang, Z. G.; Chen, Y. F.; Li, P. J.; Hao, X.; Liu, J. B.; Huang, R.; Li, Y. R. Flexible Graphene-Based Electroluminescent Devices. *ACS Nano* **2011**, *5* (9), 7149–7154.
(139) Brubaker, C. D.; Newcome, K.; Jennings, G. K.; Adams, D. E. 3D-Printed Electroluminescent Devices. *Submiss.* **2018**.
(140) Patel, D. K.; Cohen, B. El; Etgar, L.; Magdassi, S. Fully 2D and 3D Printed Anisotropic Mechanoluminescent Objects and Their Application for Energy Harvesting in the Dark. *Mater. Horizons* **2018**, *5* (4), 708–714.
(141) Lee, J. H.; Zapata, P.; Choi, S.; Meredith, J. C. Effect of Nanowhisker-Modified Zeolites on Mechanical and Thermal Properties of Poly(Vinyl Acetate) Composites with Pure-Silica MFI. *Polymer (Guildf).* **2010**, *51* (24), 5744–5755.
(142) Bansal, A.; Yang, H.; Li, C.; Cho, K.; Benicewicz, B. C.; Kumar, S. K.; Schadler, L. S. Quantitative Equivalence between Polymer Nanocomposites and Thin Polymer Films. *Nat. Mater.* **2005**, *4* (9), 693–698.
(143) Ash, B. J.; Siegel, R. W.; Schadler, L. S. Mechanical Behavior of Alumina/Poly(Methyl Methacrylate) Nanocomposites. *Macromolecules* **2004**, *37* (4), 1358–1369.
(144) Xu, S. J.; Chua, S. J.; Liu, B.; Gan, L. M.; Chew, C. H.; Xu, G. Q. Luminescence Characteristics of Impurities-Activated ZnS Nanocrystals Prepared in Microemulsion with Hydrothermal Treatment. *Appl. Phys. Lett.* **1998**, *73* (4), 478–480.
(145) Peng, W. Q.; Cong, G. W.; Qu, S. C.; Wang, Z. G. Synthesis and Photoluminescence of ZnS:Cu Nanoparticles. *Opt. Mater. (Amst).* **2006**, *29* (2–3), 313–317.
(146) Sreeja, R.; Sridharan, K.; Philip, R.; Jayaraj, M. K. Impurity Mediated Large Three Photon Absorption in ZnS:Cu Nanophosphors. *Opt. Mater. (Amst).* **2014**, *36* (5), 861–866.
(147) Fang, H.; Tian, H.; Li, J.; Li, Q.; Dai, J.; Ren, T. L.; Dong, G.; Yan, Q. Self-Powered Flat Panel Displays Enabled by Motion-Driven Alternating Current Electroluminescence. *Nano Energy* **2016**, *20*, 48–56.
(148) Murugadoss, G. Synthesis and Photoluminescence Properties of Zinc Sulfide Nanoparticles Doped with Copper Using Effective Surfactants. *Particuology* **2013**, *11*

(5), 566–573.
(149) Ummartyotin, S.; Bunnak, N.; Juntaro, J.; Sain, M.; Manuspiya, H. Synthesis and Luminescence Properties of ZnS and Metal (Mn, Cu)-Doped-ZnS Ceramic Powder. *Solid State Sci.* **2012**, *14* (3), 299–304.
(150) Jun, S.; Kim, Y.; Ju, B. K.; Kim, J. W. Extremely Flexible, Transparent, and Strain-Sensitive Electroluminescent Device Based on ZnS:Cu-Polyvinyl Butyral Composite and Silver Nanowires. *Appl. Surf. Sci.* **2018**, *429*, 144–150.
(151) Qiao, B.; Tang, Z. L.; Zhang, Z. T.; Chen, L. Study on ZnGa2O4:Cr3+ a.c. Powder Electroluminescent Device. *Mater. Lett.* **2007**, *61* (2), 401–404.
(152) Brubaker, C. D.; Frecker, T. M.; Njoroge, I.; Kane Jennings, G.; Adams, D. E. Poly(Acrylic Acid) Coated Gold Nanoparticles for PH Sensing Applications. In *8th European Workshop on Structural Health Monitoring, EWSHM 2016*; 2016; Vol. 4.

APPENDIX

Appendix A

Incorporation of Fluorescent Quantum Dots for 3D Printing and Additive Manufacturing Applications

Fluorescence lifetime measurements

For time-resolved photoluminescence (TRPL) measurements, the QD films were excited at low power (~ 30mW/cm^2) using a 405 nm pulsed source (100 ps pulse duration) with a repetition rate of 1 MHz. Photoluminescence from the films was filtered with an appropriate long-pass filter and directed onto a single-photon avalanche photo-diode (SPAD, Micro Photon Devices, PD-050-0TC). A time-correlated single photon-counting unit (TCSPC, PicoHarp 300) was used to generate a histogram of photon arrival times. Lifetimes were determined by fitting the histogram of arrival times to a tri-exponential function:

$$I_{PL}(t) = \Sigma_i = A_i exp(-t/\tau_i) \quad (1)$$

The average lifetime, τ_{avg} was calculated using the fit components as follows:

$$\tau_{avg} = \Sigma_i^n \frac{A_i \tau_i}{\Sigma_i^n A_i} \quad (2)$$

Decay curves were fit with the following equation, where A_i and τ_i are the decay amplitudes and lifetimes, respectively.

$$I(t) = \Sigma_{i=3}^n A_i e^{-\left(\frac{t}{\tau_i}\right)} \quad (3)$$

For samples in solution TRPL measurements were performed on diluted solutions with optical densities below 0.1 at the lowest-energy absorption transition.

Table A1. Lifetime analysis of 3D-printed PLA/CdSSe QD films and CdSSe QDs in solution.

Parameter	CdSSe solution	0.1%	0.5%	1.0%	3.0%	5.0%	7.0%
A_1 (counts)	210.7	377.8	642.6	517.1	326.7	248.8	252.0
τ_1 (ns)	46.811	33.541	31.656	30.920	30.392	32.506	34.977
A_2 (counts)	4183.3	1308.9	1801.1	1861.9	1980.2	2002.8	2152.4
τ_2 (ns)	19.112	7.905	10.499	10.490	9.265	9.579	11.117
A_3 (counts)	560.9	2675.2	2426.6	2625.4	2696.4	2790.5	2607.1
τ_3 (ns)	4.395	1.247	1.869	2.009	2.251	2.459	3.006

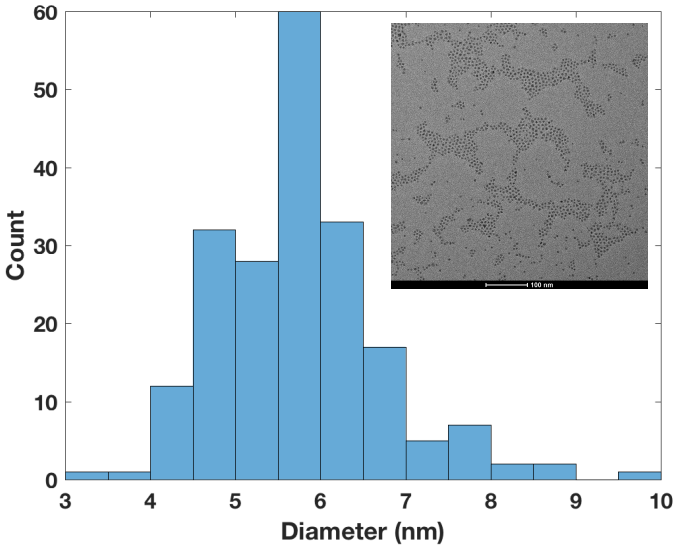

Figure A1. Size distribution and TEM image of CdSSe QDs in solution. Average diameter of CdSSe QDs in solution is 5.74 ± 0.95 nm.

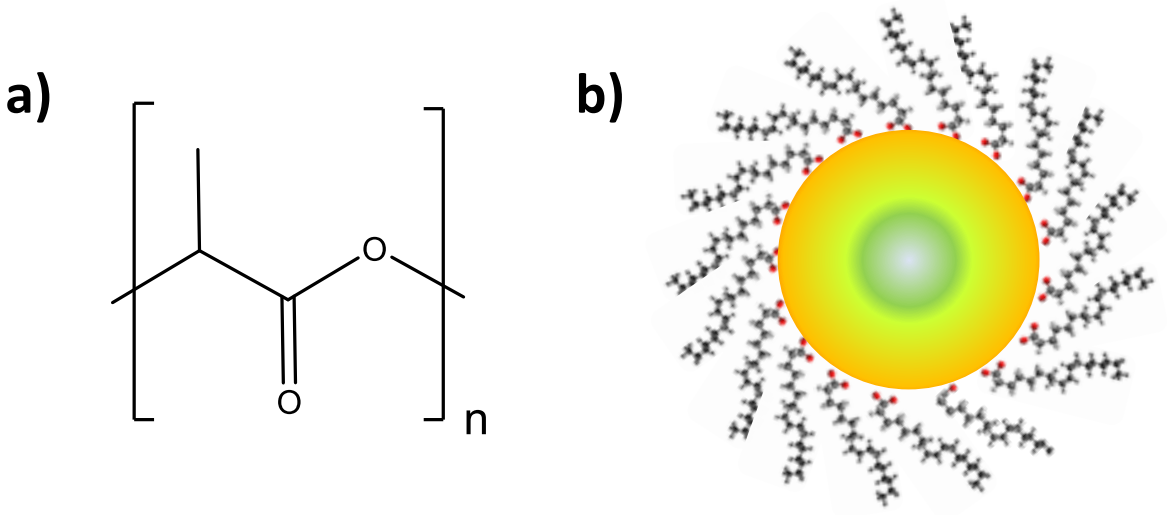

Figure A2. a) Chemical structure of polylactic acid polymer host matrix and b) schematic representation of cadmium sulfur selenide graded alloy quantum dots and corresponding oleic acid surface ligands.

Appendix B

Nondestructive Evaluation and Detection of Defects in 3D-Printed Materials Using the Optical Properties of Gold Nanoparticles

Tensile Testing Results

Tensile testing was performed on pure PLA control and PLA/AuNP (0.1% AuNP in PLA by weight) samples to evaluate the impact AuNPs have on the overall stability of 3D-printed parts. Overall, we found that the presence of gold nanoparticles embedded in the PLA host matrix did influence the maximum tensile strength at failure, where PLA/AuNP samples had a 13 ± 2% lower maximum stress at failure compared to pure PLA control samples. We attribute the decrease in overall material strength to discontinuities in the polymer chain network caused by the presence of embedded gold nanoparticles.

Appendix C

3D-Printed Alternating Current Electroluminescent Devices

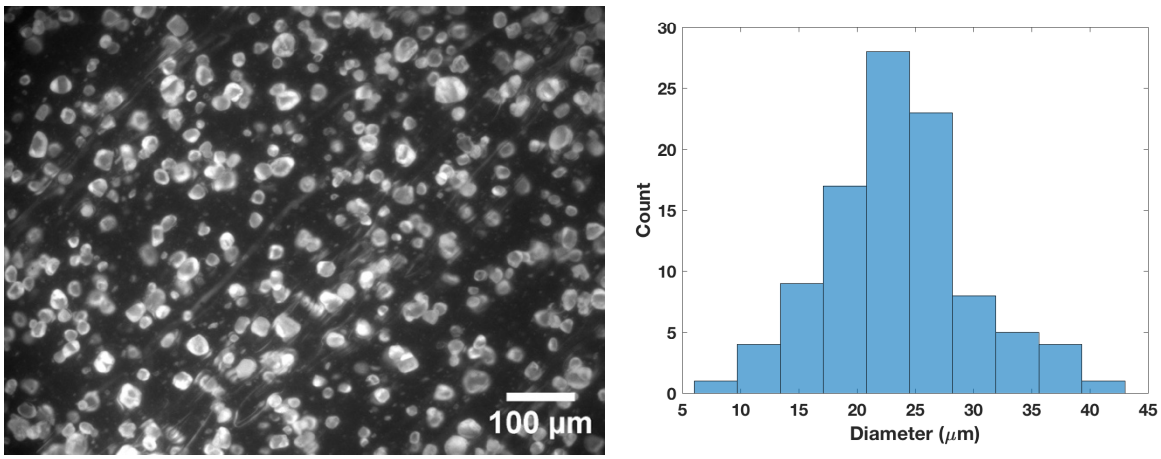

Figure C1. WL microscopy of ZnS:Cu phosphors in PLA, and corresponding size distribution. Average diameter is 24 ± 6 µm.

CIE Coordinates (x,y)

The following Matlab scripts were used to calculate CIE coordinates (x,y) for all 3D-printed ACEL devices tested. First, the as-recorded spectral data ('plresponse' variable) was converted to a matrix ('maxdata' variable) where the maximum luminescent intensity for every round integer wavelength value was calculated. This conversion was necessary to calculate CIE coordinates, as the CIE transfer/color-matching functions and variables are reported at 1 nm increments from 400 nm – 800 nm (i.e. 400 nm, 401 nm, 402 nm … 800 nm).

```
z = 400:800;
x = floor(plresponse(:,1));
maxdata = zeros(length(z),size(y,2));
for kk = 1:6
    for ii = 1:length(z)
        for jj = 1:length(x)
            if x(jj) == z(ii)
                if y(jj,kk) > maxdata(ii,kk)
                    maxdata(ii,kk) = y(jj,kk);
                end
            elseif x(jj)> z(ii)+1
                continue;
            end
        end
    end
end
```

Representative matrix transformations from the as-recorded spectral data ('plresponse') to the maximum PL for each wavelength at 1 nm increments ('maxdata') for the code included above is shown in Table C1 below:

As-Recorded Spectral Data ('plresponse')		**Converted Spectral Response ('maxdata')**	
Wavelength (nm)	Luminescence (a.u.)	Wavelength (nm)	Luminescence (a.u.)
515.2	11690	515	11690
515.5	11597		
515.9	11649		
521.1	11064	521	11064
521.4	10892		
521.7	10989		

Next, the spectral data for each whole integer value was transformed into CIE coordinate space through the use of various transfer/color-matching functions and normalizations as follows:

```
% calculate CIE Coordinates

% importing weighting factor for the three color matching functions

ciexyz = xlsread('ciexyz.xlsx');

% initializing variables to calculate and store color matching functions

xbar = [];
ybar = [];
zbar = [];

% initializing variable to store calculated CIE coordinates (x,y)

xcoords = [];
ycoords = [];

% performing calculations for CIE coordinates (x,y)

% counter is defined by the number of tests run for each sample
% here, we are looking at a constant excitation frequency with increasing
% excitation voltages (150V, 175V, 200V, 225V, and 245V) so a total of
five
% scans (i.e. 2:6) were run.

for pp = 2:6
    xbar = [];
    ybar = [];
    zbar = [];
    % multiplying the recorded spectral response ('maxdata') by the
    % color-matching functions ('ciexyz') for the x, y, and z functions
```

```
    for i = 1:401
        xbar = [xbar; maxdata(i,pp)*ciexyz(i,1)];
        ybar = [ybar; maxdata(i,pp)*ciexyz(i,2)];
        zbar = [zbar; maxdata(i,pp)*ciexyz(i,3)];
    end

    % summing Xbar, Ybar and Zbar at every wavelength from 400 nm to 800
nm
    normaldata = sum([xbar ybar zbar],2);

    % calculating sum of Xbar, Ybar, and Zbar matricies
    sumx = sum(xbar);
    sumy = sum(ybar);
    sumz = sum(zbar);

    % here I am calculating the tristimulus values, x1, y1, and z1
    x1 = sumx/sum([sumx,sumy,sumz]);
    y1 = sumy/sum([sumx,sumy,sumz]);
    z1 = sumz/sum([sumx,sumy,sumz]);

    % with these values, additional constants u and v are calculated in
    % order to obtain CIE coordinates
    u = (4*x1)/(x1+15*y1+3*z1);
    v = (6*y1)/(x1+15*y1+3*z1);

    % finally, 1931 CIE coordinates (x,y) are calculated using the above
    % calculated u and v variables
    xcie = (3*u)/(2*u-8*v+4);
    ycie = (2*v)/(2*u-8*v+4);

    % making and storing matrix with the (x,y) CIE coordinates for all 5
    % excitation conditions tested for this sample
    xcoords = [xcoords; xcie];
    ycoords = [ycoords; ycie];
end
```

The transfer/color-matching functions/values with a 1 nm step size were downloaded from http://cvrl.ioo.ucl.ac.uk/cmfs.htm. The two dimensional chromacity plot (often referred to as the CIE 1931 color space diagram) was plotted in Matlab using the Colour toolbox in the second edition of Computation Colour Science downloaded from MathWorks at the following web address (https://www.mathworks.com/matlabcentral/fileexchange/40640-computational-colour-science-using-matlab-2e).

Additional tables, plots and spectral responses for the 3D-printed ACEL devices are included in the following figures:

Table C1. Curve fitting data for voltage-dependent maximum EL response at various frequencies (Figure C8). Data was fit with a linear model using the following equation: y(x) = p1*x+p2.

Frequency (Hz)	p1	p2	R-Squared
100	12.57	-1341	0.9969
500	56.8	-6992	0.9965
1000	95.13	-11380	0.9965
3000	187.1	-22600	0.9972
5000	234.5	-28440	0.9954
7000	265.8	-32310	0.9961
10000	303	-37010	0.9969

The following figures represent the spectral response of the ACEL devices tested in this thesis. A total of five samples (Sample 1 – 5) were tested for each voltage- and frequency-dependent response case, where the resultant optical response is included in Figures C1 – C10. Overall, all samples displayed consistent and reproducible electroluminescent trends and behaviors.

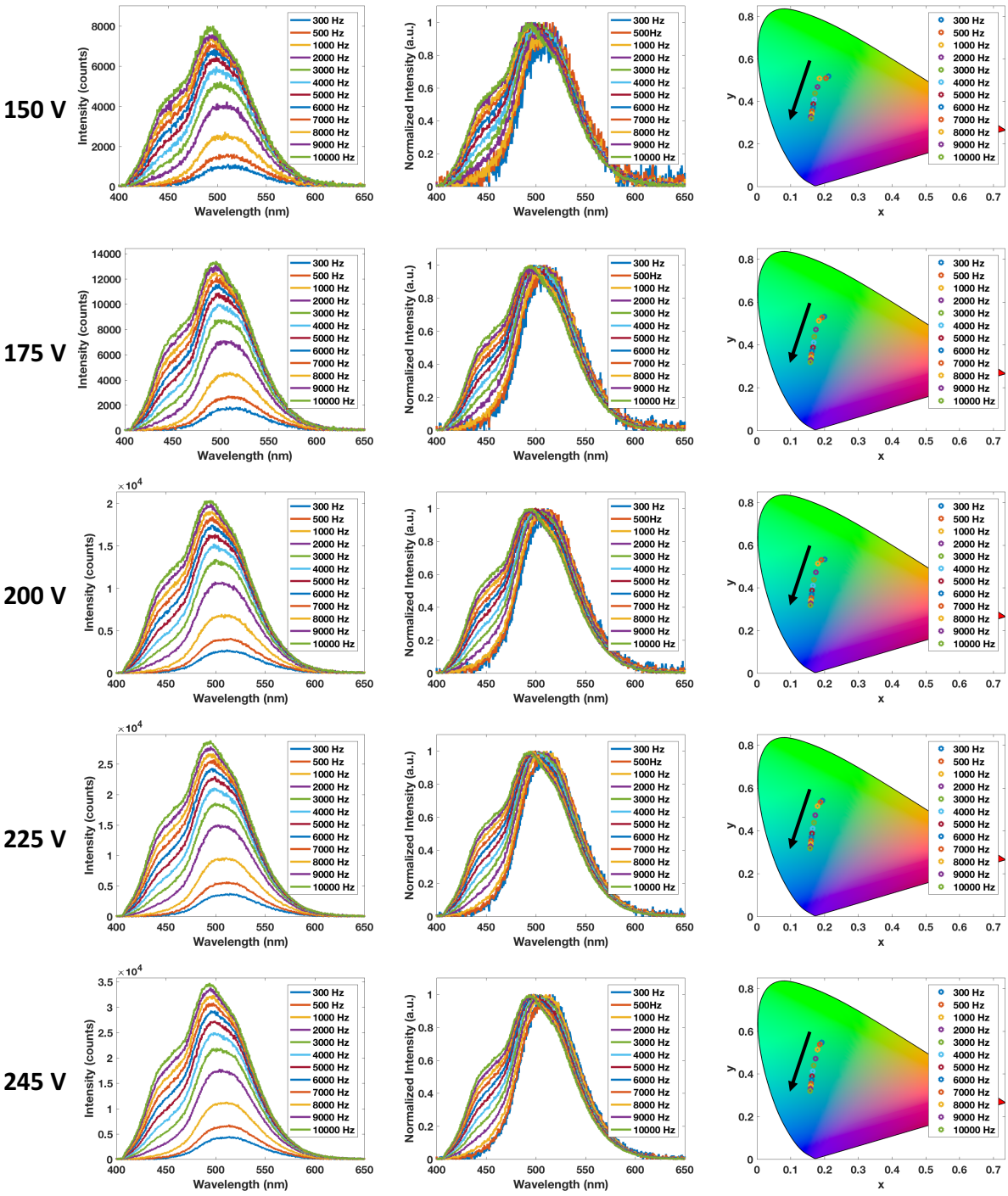

Figure C1. Frequency-dependent as-recorded and normalized spectral response (left and middle columns) of a 3D-printed ACEL device at various excitation voltages and corresponding CIE coordinates (x,y) (right column) for Sample 1.

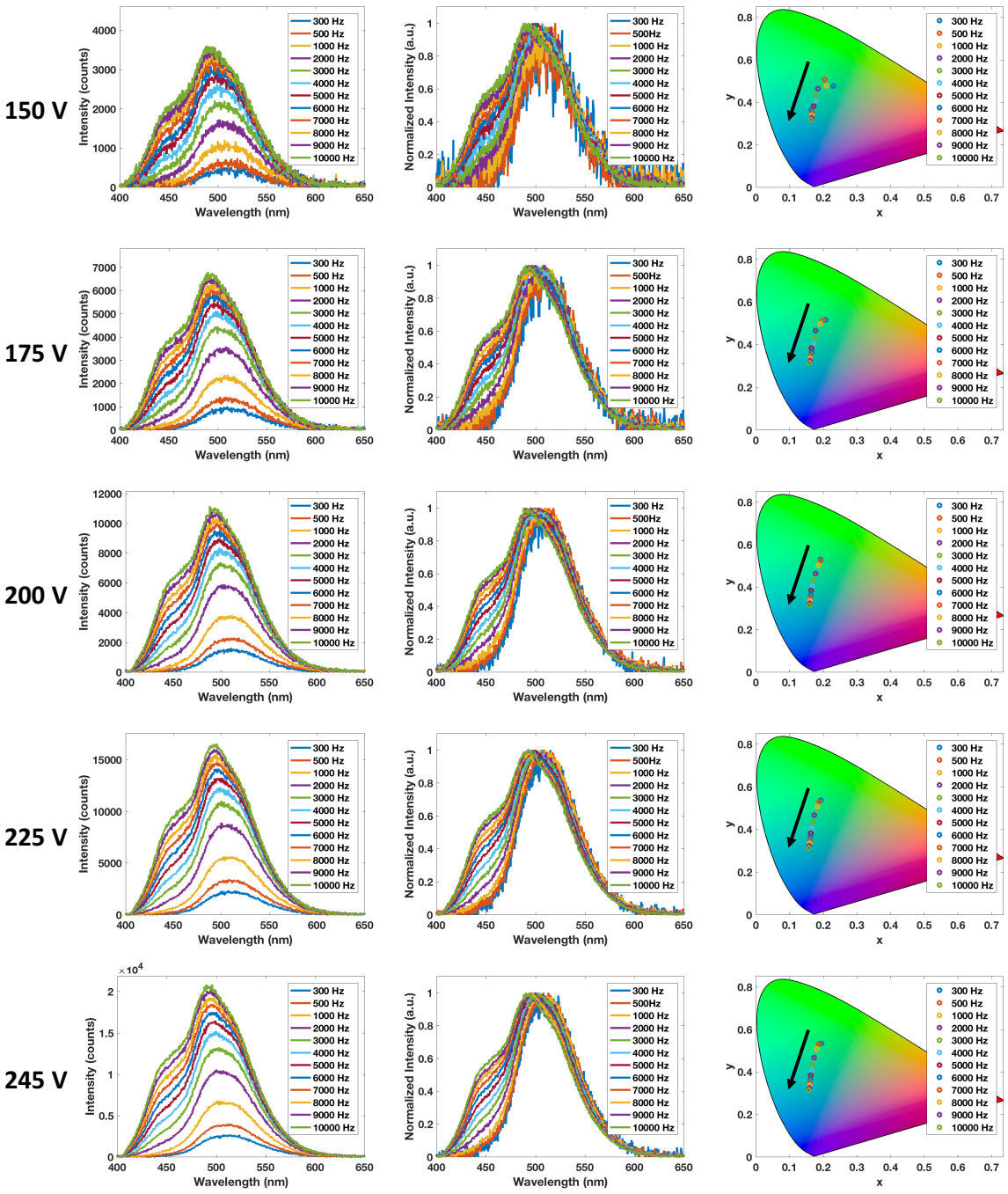

Figure C2. Frequency-dependent as-recorded and normalized spectral response (left and middle columns) of a 3D-printed ACEL device at various excitation voltages and corresponding CIE coordinates (x,y) (right column) for Sample 2.

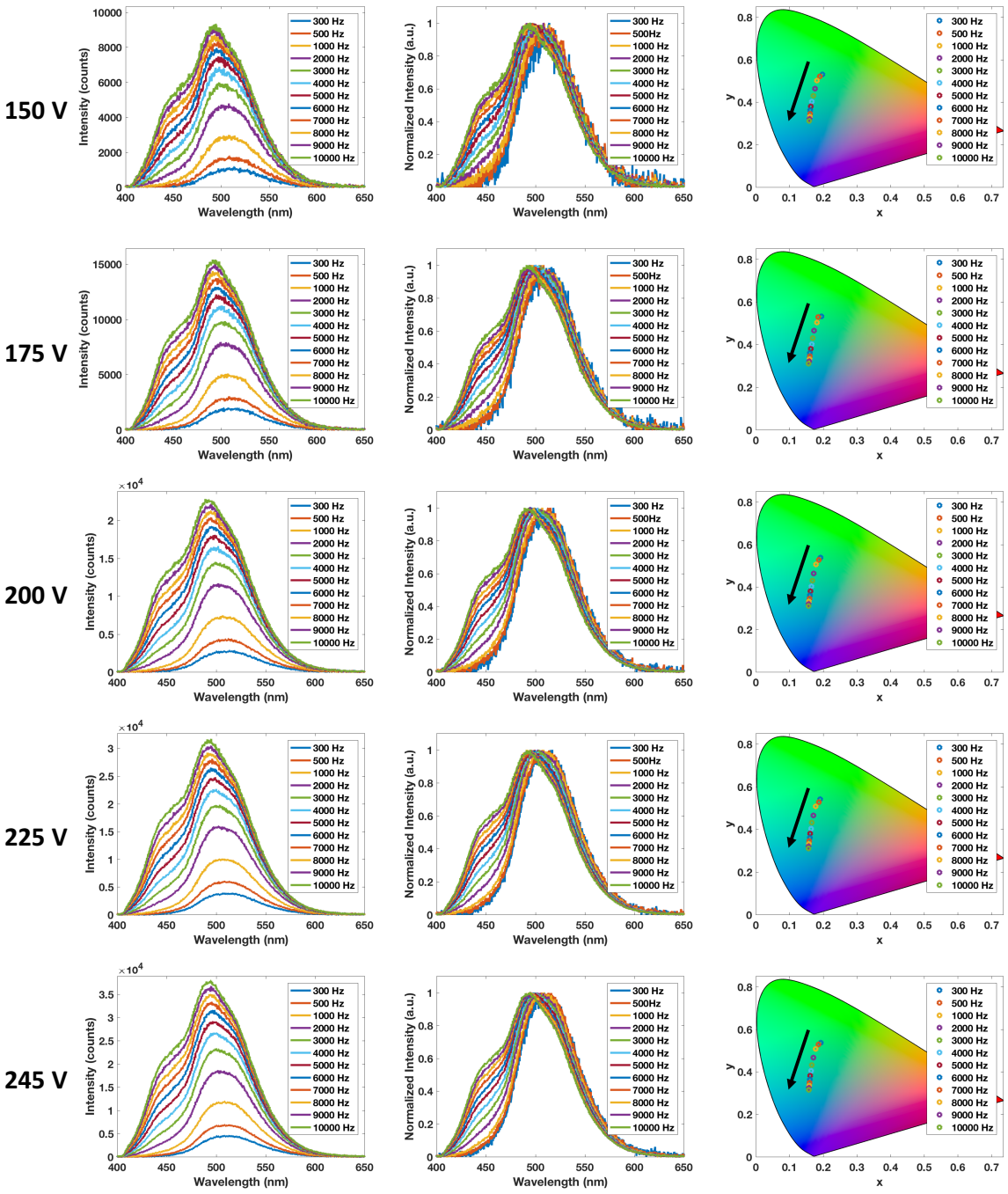

Figure C3. Frequency-dependent as-recorded and normalized spectral response (left and middle columns) of a 3D-printed ACEL device at various excitation voltages and corresponding CIE coordinates (x,y) (right column) for Sample 3.

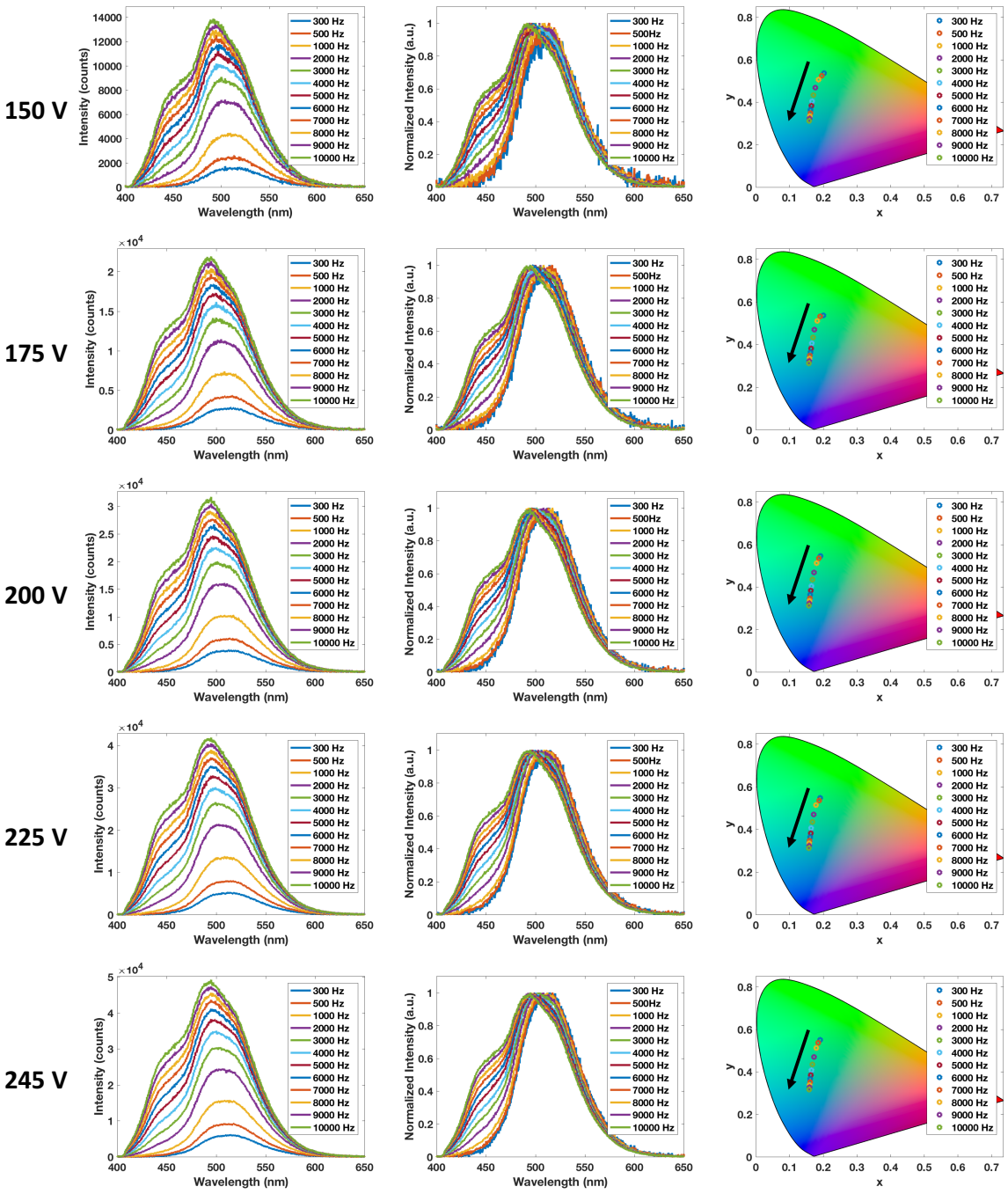

Figure C4. Frequency-dependent as-recorded and normalized spectral response (left and middle columns) of a 3D-printed ACEL device at various excitation voltages and corresponding CIE coordinates (x,y) (right column) for Sample 4.

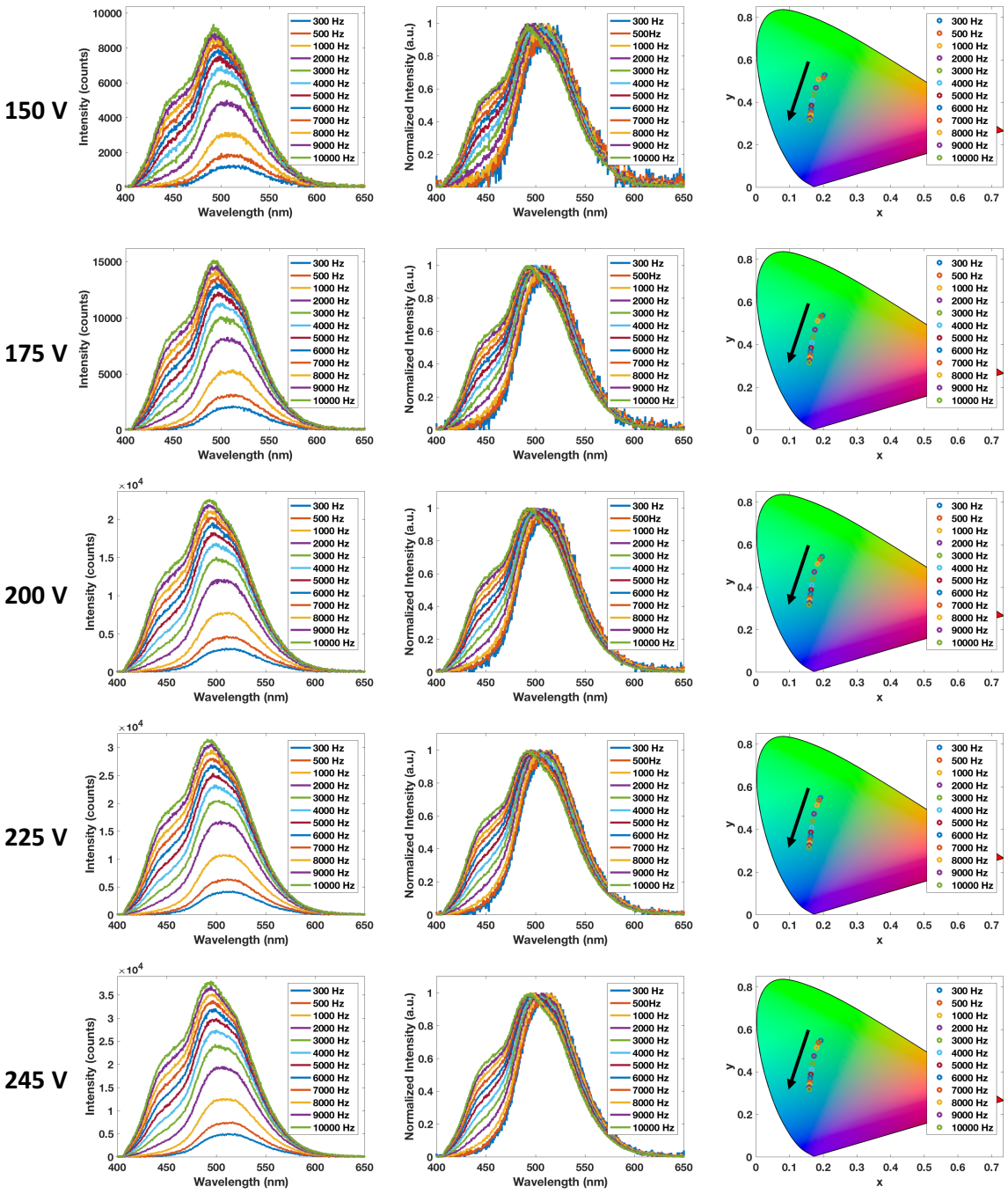

Figure C5. Frequency-dependent as-recorded and normalized spectral response (left and middle columns) of a 3D-printed ACEL device at various excitation voltages and corresponding CIE coordinates (x,y) (right column) for Sample 5.

Table C1 – Frequency-dependent response

	150 V		175 V		200 V		225 V		245 V	
Frequency (Hz)	x	y	x	y	x	y	x	y	x	y
50	0.27 ± 0.018	0.47 ± 0.034	0.24 ± 0.013	0.50 ± 0.016	0.23 ± 0.006	0.52 ± 0.012	0.22 ± 0.006	0.54 ± 0.017	0.22 ± 0.010	0.54 ± 0.014
100	0.24 ± 0.013	0.49 ± 0.025	0.22 ± 0.014	0.52 ± 0.023	0.22 ± 0.007	0.53 ± 0.011	0.21 ± 0.003	0.54 ± 0.008	0.21 ± 0.003	0.55 ± 0.008
300	0.21 ± 0.013	0.52 ± 0.024	0.20 ± 0.004	0.53 ± 0.009	0.19 ± 0.004	0.54 ± 0.006	0.19 ± 0.001	0.54 ± 0.005	0.19 ± 0.002	0.54 ± 0.007
500	0.20 ± 0.006	0.52 ± 0.008	0.19 ± 0.005	0.53 ± 0.007	0.19 ± 0.002	0.53 ± 0.005	0.19 ± 0.000	0.53 ± 0.004	0.19 ± 0.001	0.53 ± 0.004
1000	0.19 ± 0.011	0.50 ± 0.013	0.18 ± 0.004	0.51 ± 0.006	0.18 ± 0.003	0.51 ± 0.005	0.18 ± 0.002	0.51 ± 0.004	0.18 ± 0.001	0.51 ± 0.003
2000	0.18 ± 0.003	0.47 ± 0.003	0.18 ± 0.002	0.47 ± 0.003	0.17 ± 0.002	0.47 ± 0.004	0.17 ± 0.001	0.47 ± 0.003	0.17 ± 0.001	0.47 ± 0.003
3000	0.17 ± 0.003	0.43 ± 0.003	0.17 ± 0.002	0.43 ± 0.004	0.17 ± 0.001	0.43 ± 0.004	0.17 ± 0.001	0.43 ± 0.003	0.17 ± 0.001	0.44 ± 0.003
4000	0.17 ± 0.005	0.41 ± 0.003	0.17 ± 0.002	0.41 ± 0.003	0.17 ± 0.001	0.41 ± 0.003	0.17 ± 0.001	0.41 ± 0.003	0.17 ± 0.001	0.41 ± 0.003
5000	0.17 ± 0.003	0.38 ± 0.003	0.16 ± 0.001	0.38 ± 0.003	0.16 ± 0.001	0.38 ± 0.003	0.16 ± 0.001	0.38 ± 0.003	0.16 ± 0.001	0.39 ± 0.003
6000	0.16 ± 0.002	0.37 ± 0.003	0.16 ± 0.002	0.36 ± 0.003	0.16 ± 0.001	0.36 ± 0.003	0.16 ± 0.001	0.36 ± 0.003	0.16 ± 0.001	0.37 ± 0.003
7000	0.16 ± 0.002	0.35 ± 0.003	0.16 ± 0.001	0.35 ± 0.003	0.16 ± 0.001	0.35 ± 0.003	0.16 ± 0.001	0.35 ± 0.003	0.16 ± 0.001	0.35 ± 0.003
8000	0.16 ± 0.002	0.34 ± 0.003	0.16 ± 0.001	0.34 ± 0.003	0.16 ± 0.001	0.34 ± 0.003	0.16 ± 0.001	0.34 ± 0.003	0.16 ± 0.001	0.34 ± 0.003
9000	0.16 ± 0.003	0.32 ± 0.003	0.16 ± 0.001	0.32 ± 0.003	0.16 ± 0.001	0.32 ± 0.003	0.16 ± 0.001	0.32 ± 0.003	0.16 ± 0.001	0.33 ± 0.003
10000	0.16 ± 0.002	0.32 ± 0.003	0.16 ± 0.001	0.31 ± 0.003	0.16 ± 0.001	0.31 ± 0.003	0.16 ± 0.001	0.31 ± 0.003	0.16 ± 0.001	0.32 ± 0.003

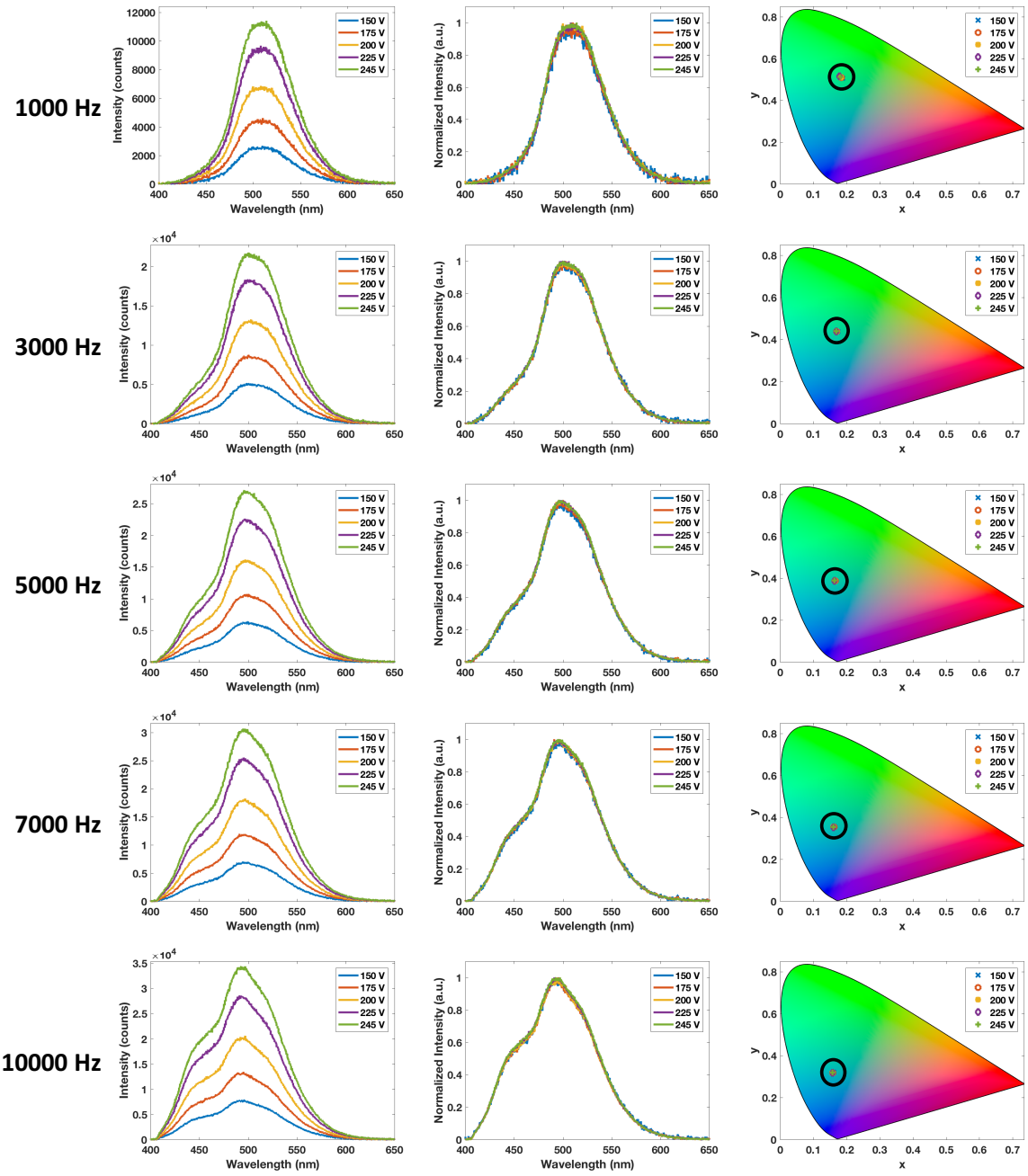

Figure C6. Voltage-dependent as-recorded and normalized spectral response (left and middle columns) of a 3D-printed ACEL device at various excitation frequencies and corresponding CIE coordinates (x,y) (right column) for Sample 1.

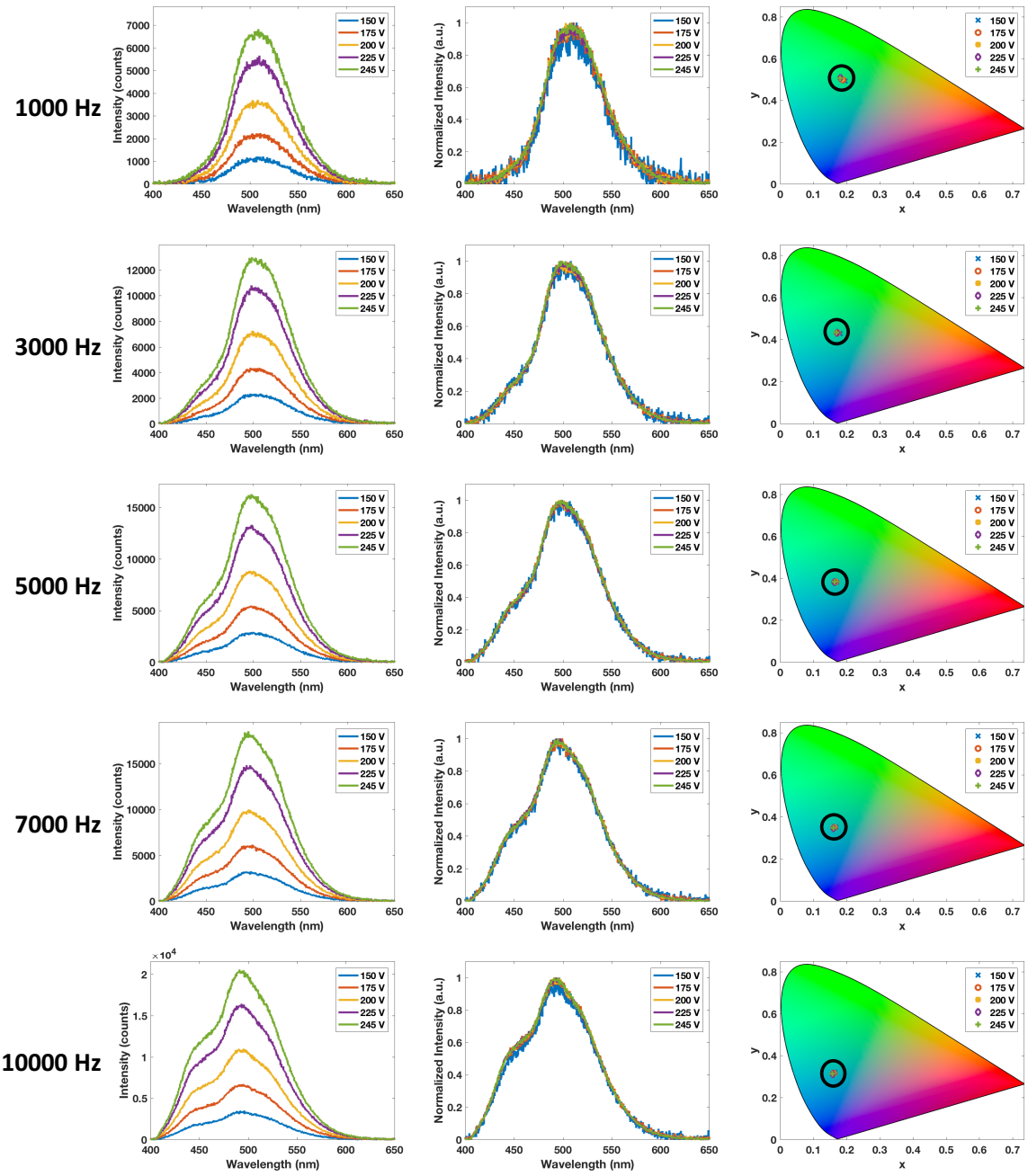

Figure C7. Voltage-dependent as-recorded and normalized spectral response (left and middle columns) of a 3D-printed ACEL device at various excitation frequencies and corresponding CIE coordinates (x,y) (right column) for Sample 2.

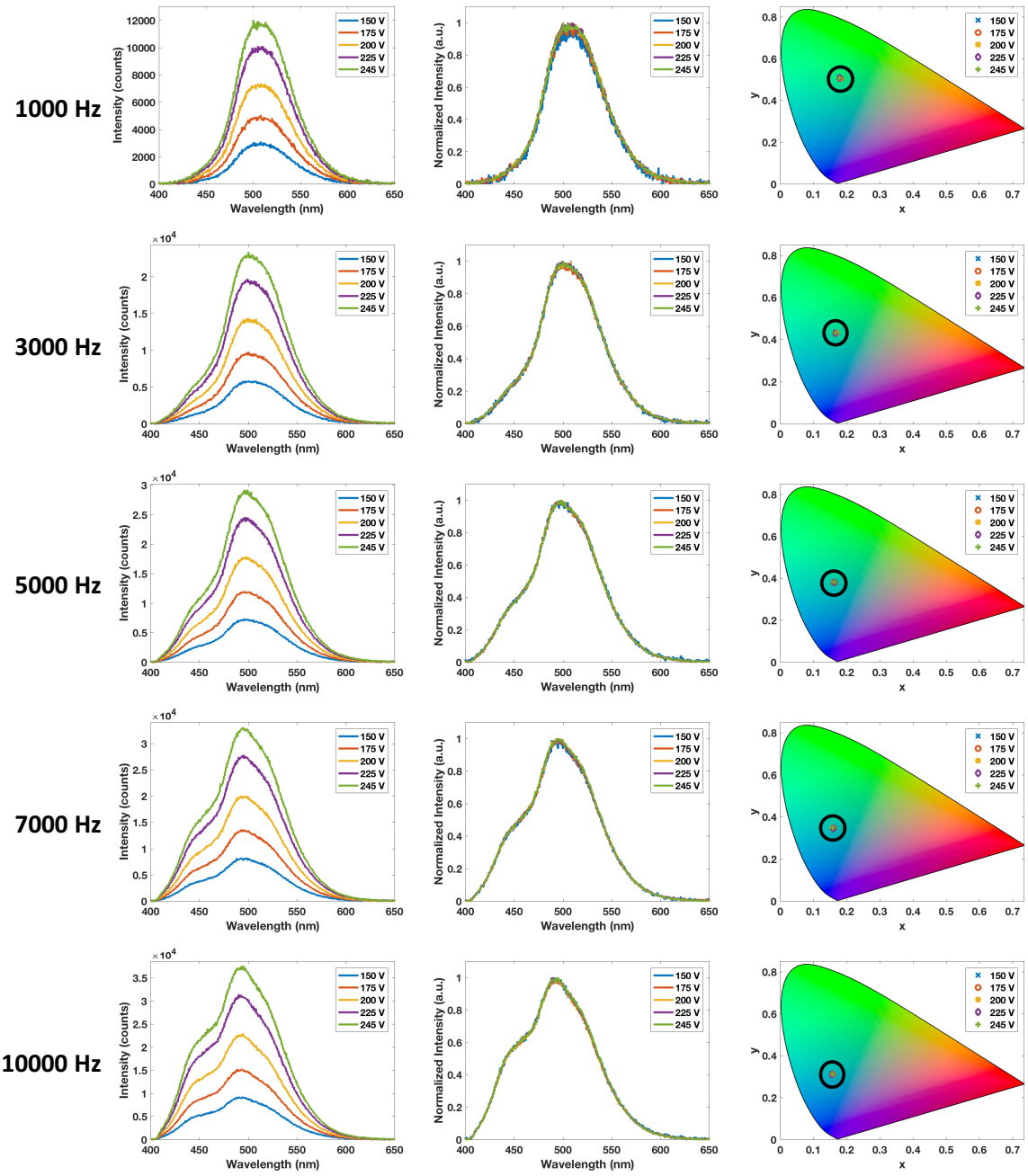

Figure C8. Voltage-dependent as-recorded and normalized spectral response (left and middle columns) of a 3D-printed ACEL device at various excitation frequencies and corresponding CIE coordinates (x,y) (right column) for Sample 3.

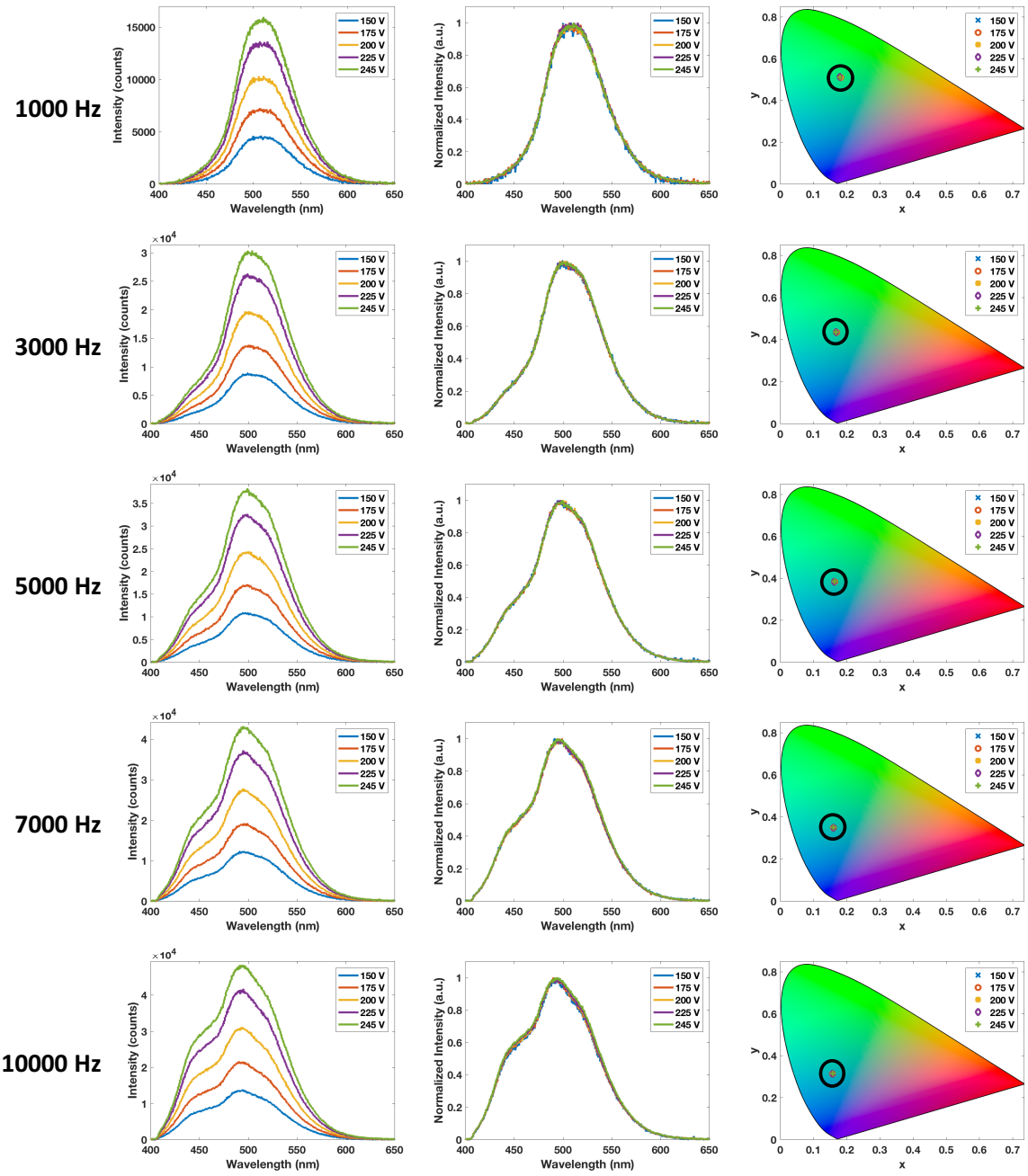

Figure C9. Voltage-dependent as-recorded and normalized spectral response (left and middle columns) of a 3D-printed ACEL device at various excitation frequencies and corresponding CIE coordinates (x,y) (right column) for Sample 4.

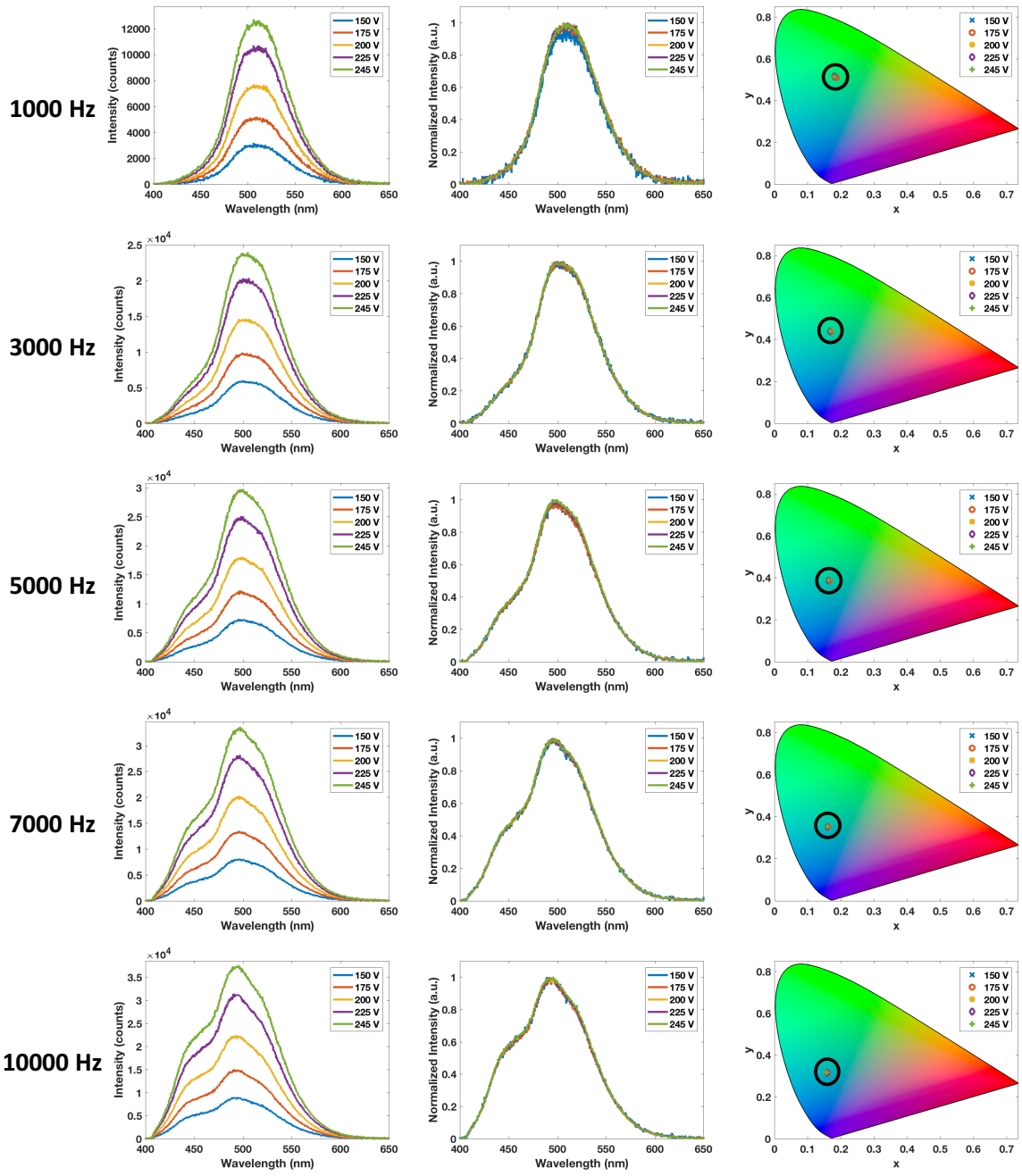

Figure C10. Voltage-dependent as-recorded and normalized spectral response (left and middle columns) of a 3D-printed ACEL device at various excitation frequencies and corresponding CIE coordinates (x,y) (right column) for Sample 5.

Table C2 – Voltage-dependent response

	1000 Hz		3000 Hz		5000 Hz		7000 Hz		10000 Hz	
Frequency (Hz)	x	y	x	y	x	y	x	y	x	y
150	0.19 ± 0.006	0.50 ± 0.007	0.17 ± 0.004	0.43 ± 0.004	0.17 ± 0.002	0.38 ± 0.004	0.16 ± 0.003	0.35 ± 0.003	0.16 ± 0.002	0.32 ± 0.004
175	0.18 ± 0.003	0.51 ± 0.004	0.17 ± 0.002	0.43 ± 0.003	0.16 ± 0.002	0.38 ± 0.003	0.16 ± 0.001	0.35 ± 0.003	0.16 ± 0.002	0.32 ± 0.003
200	0.18 ± 0.002	0.51 ± 0.004	0.17 ± 0.001	0.43 ± 0.003	0.16 ± 0.001	0.38 ± 0.003	0.16 ± 0.001	0.35 ± 0.003	0.16 ± 0.001	0.31 ± 0.003
225	0.18 ± 0.001	0.51 ± 0.004	0.17 ± 0.002	0.43 ± 0.003	0.16 ± 0.001	0.38 ± 0.003	0.16 ± 0.001	0.35 ± 0.003	0.16 ± 0.001	0.31 ± 0.003
245	0.18 ± 0.001	0.51 ± 0.004	0.17 ± 0.001	0.44 ± 0.003	0.16 ± 0.001	0.39 ± 0.003	0.16 ± 0.001	0.35 ± 0.003	0.16 ± 0.001	0.32 ± 0.003